LEVERAGING INVERTER-INTERFACED ENERGY STORAGE FOR FREQUENCY CONTROL IN LOW-INERTIA POWER SYSTEMS

by

Yan Jiang

A dissertation submitted to Johns Hopkins University

in conformity with the requirements for the degree of

Doctor of Philosophy

Baltimore, Maryland

July, 2021

Abstract

The shift from conventional synchronous generation to renewable inverter-interfaced sources has led to a noticeable degradation of frequency dynamics in power systems, mainly due to a loss of inertia. Fortunately, the recent technology advancement and cost reduction in energy storage facilitate the potential for higher renewable energy penetration via inverter-interfaced energy storage. With proper control laws imposed on inverters, the rapid power-frequency response from energy storage contributes to mitigating the degradation. A straightforward choice is to emulate the droop response and/or inertial response of synchronous generators through droop control (DC) or virtual inertia (VI), yet they do not necessarily fully exploit the benefits of inverter-interfaced energy storage. This thesis thus seeks to challenge this naive choice of mimicking synchronous generator characteristics by advocating for a principled control design perspective.

To achieve this goal, we build an analysis framework for quantifying the performance of power systems using signal and system norms, within which we perform a systematic study to evaluate the effect of different control laws on various performance metrics. Our analysis unveils several limitations of

traditional control laws, such as the coupling between the steady-state performance and dynamic performance in DC and the high noise sensitivity of VI, which motivate the need for better solutions. We first propose dynam-i-c Droop control (iDroop) which is proved to enjoy many good properties. For example, iDroop is able to decouple the steady-state performance and dynamic performance. Moreover, iDroop can be tuned to achieve Nadir elimination, zero synchronization cost, and low noise sensitivity. However, iDroop has no control over the rate of change of frequency (RoCoF), which is undesirable in low-inertia power systems for the risk of falsely triggering protections. Thus, we further propose frequency shaping control (FS) whose most outstanding feature is its ability to shape the system frequency dynamics following a sudden power imbalance into a first-order one with the specified synchronous frequency and RoCoF by adjusting two independent control parameters. We finally validate theoretical results through numerical experiments performed on a more realistic power system test case.

Thesis Committee

Enrique Mallada (Primary Advisor)
Assistant Professor
Department of Electrical and Computer Engineering
Johns Hopkins University

Pablo A. Iglesias
Edward J. Schaefer Professor
Department of Electrical and Computer Engineering
Johns Hopkins University

Dennice F. Gayme
Associate Professor
Department of Mechanical Engineering
Johns Hopkins University

Petr Vorobev
Assistant Professor
Center for Energy Science and Technology
Skolkovo Institute of Science and Technology

Dedicated to my family.

Acknowledgments

Looking back at my past five years at Hopkins, there are many people to thank for their help and support. Without them, it would not have been possible for me to complete this journey.

I owe my deepest gratitude to my advisor, Enrique Mallada, for his guidance throughout my graduate studies. Enrique is not only the most talented but also the most diligent person I have ever known. Such great personal qualities make him an outstanding scholar. I am impressed by his enthusiasm and patience for tackling challenging research problems. Moreover, he is the best advisor I could imagine. He instructs me more by deed than by word in how to do research. Whenever I got stuck in research problems, he would always be by my side. He encouraged me to try various methods before easily giving up. In fact, the time we spent together at Barton Hall 312 in deriving formulas and writing proofs on the whiteboard has been the most stimulating experience for me during these years. I would cherish that memory forever. He also shows me the importance to strike a good balance between research and life. Thus, I starts to work out more often just as he does, which helps to strengthen both my body and mind, two foundations for other demands of life such as to be a good researcher.

I would also like to thank my colleague Petr Vorobev for his collaboration. He indeed acts more as my mentor rather than a collaborator. His professionalism lets me know what the real role of a power system engineer is. He teaches me to think more from practical perspectives, which helps me to grasp a better physical interpretation of the mathematical results we had. Due to the time difference between Baltimore and Moscow, most discussions we had were in his late evenings. I would never forget the challenging time we had before the deadline of one of our papers, during which he burned the midnight oil to work together with me on debugging the code day by day.

My next special thanks goes to Pablo A. Iglesias. I really enjoy the multiple exciting courses on control theory that I took from you at the beginning of my graduate studies, which definitely laid the groundwork for my further research on control of power systems. Also, thanks for treating me as a friend. I am very grateful for your invitations to celebrate Thanksgivings with your whole family, which warmed my heart in those lonely cold winters.

I also thank Dennice F. Gayme for serving on my dissertation committee with many kindly detailed comments.

I feel fortunate to had the chance to collaborate with Richard Pates and Andrey Bernstein. This thesis would not be possible without them.

I would like to further extend my appreciation to every member in our group, Pengcheng You, Rajni Kant Bansal, Hancheng Min, Yue Shen, Tianqi Zheng, Charalampos Avraam, Mustafa Devrim Kaba, Elijah Pivo, Eliza Cohn, Zachary Nelson, James Guthrie, and Mohammad Hajiesmaili, for the great time we spent together. Some of them are my main meal partners. I believe

that we still have chances to have our favorite hot pot together.

I also would like to thank my office mate, Debojyoti Biswas, for interesting and relaxing chatting with him.

My family, of course, deserve my special thanks. I am deeply grateful to my parents, Guanggeng Jiang and Xiaoping Yan, for their endless love from China. My deepest thanks also goes to my grandmother, Jiazhen Li, for raising me up. Last but not least, I am very lucky to have my husband, Guande Huang, in my life. You are like the star shining in my sky, which is far away in distance but never in heart. I can't wait to spend the rest of my life with you.

Table of Contents

List of Tables

List of Figures

Chapter 1

Introduction

An electric power system is a large complex dynamic network that consists of generation, transmission, and distribution systems, all of which work together to deliver the right amount of electricity from power plants to end customers. Since different components in this physical network are mutually dependent, the "right amount" actually refers to a balance between electric power supply and demand over the network on a second-by-second basis, which is the key to the normal operation of a power system [1]. A sudden surplus of generation over load boosts the frequency above its nominal value, while a sudden drop of generation below load depresses the frequency below its nominal value [2]. Usually, the nominal frequency is either 50 Hz or 60 Hz depending on the number of alternating current cycles per second in a particular power system. For example, the European and most of the Asian power grids operate at 50 Hz and the North American power grid operates at 60 Hz. Since most electrical devices connected to power grids are designed to operate within certain frequency ranges, a power imbalance not corrected timely may result in catastrophic consequences in the end. For instance, the main cause

of the 2021 Texas power crisis where the unprecedented low temperatures following severe winter storms knocked out the Texas power grid is that the deficient supply of power due to frozen equipment could not meet the high demand for electricity in such cold weather.

Nowadays, power systems are in a state of flux [3]. Motivated by growing concerns about climate change and energy depletion [4], power systems are experiencing a gradual change in the mix of generation—conventional synchronous generators are being replaced by renewable energy sources such as solar and wind energy. This tendency is in line with the goal of the Paris Agreement, under which nearly 200 countries contribute together towards reducing greenhouse gas emissions. To name a few, China and India committed to increase the nonfossil share of their energy supply to 20% and 40%, respectively, by 2030 [5, 6]. As the largest historical emitter in the world, the United States formally rejoined the Paris Agreement on February 19, 2021, with a pledge to achieve net-zero emissions no later than 2050. Clearly, this calls for further development of renewable generation. It is anticipated that the renewable share of the electricity generation mix in the United States will double from 21% in 2020 to 42% in 2050 [7].

However, this transition actually poses challenges to the operation of power systems [8, 9]. On the one hand, the intermittent nature of renewable energy sources catalyzes unpredictable changes in power generation [10]. For example, solar power is variable since the sun does not always shine and wind power is capricious since the wind does not constantly blow. Thus, more effort is needed to keep power well-balanced; otherwise frequency fluctuates

more markedly and frequently. On the other hand, renewable energy sources typically connect to power grids through power electronic converters which lack the natural inertia inherently provided by rotating mass of synchronous generators [11]. This implies a reduction of system inertia in power systems with a high penetration of renewable energy, which further adversely affects the frequency dynamics [12].

In physics, the so-called inertia reflects the tendency of any object to reject any change in its velocity, which was formulated by Isaac Newton as his well-known first law of motion. Power systems have long been predominately powered by synchronous generators, whose mechanical speed of rotation is directly coupled to electrical frequency of the grid via electromagnetic induction. Hence, the moment of inertia of rotating mass of these generators measures the resistance of power systems to change in grid frequency. Roughly speaking, greater moment of inertia gives rise to stubborner resistance to frequency deviations since the kinetic energy stored in rotating mass is directly proportional to the moment of inertia. Specifically, the kinetic energy is equal to one-half of the product of the moment of inertia and the squared electrical angular frequency. This relation lays the groundwork for understanding the fact that the kinetic energy stored in rotating mass of synchronous generators effectively performs as a buffer against frequency changes. As mentioned before, the grid frequency rises above or drops below its nominal value during power imbalances, depending on whether a net excess or deficiency of power supply occurs. The mechanism is as follows: if power supply exceeds demand, the kinetic energy is absorbed into the rotating mass from the grid, which

speeds up generators and thus the grid frequency increases; if power demand exceeds supply, the kinetic energy is extracted from the rotating mass to the grid, which slows down generators and thus the grid frequency decreases. Although this procedure, also known as *inertial response*, typically lasts only for a few seconds, it provides time for turbine-governors to respond to power imbalances by automatically adjusting the supply of mechanical power to synchronous generators in a desired way. Here, a turbine-governor, as shown in Figure 1.1, is a device attached to the shaft of a driven generator for the sake of controlling the power that enters the generator in response to its rotational speed variation. For example, in a fossil-fueled power plant, a governor manipulates the position of a steam valve such that the steam flow into the turbine decreases if the generator speed rises and increases if the generator speed falls, with the turbine converting thermal energy to rotational energy that drives the generator. This kind of procedure is known as *droop response*, which helps to arrest and stabilize the frequency to a value that still deviates from the nominal one. Conceivably, for a power system with sufficient online generators, a large amount of moment of inertia is present and hence only a minor frequency deviation is able to recover the power balance through inertial and droop response.[1]

Nevertheless, the ever-growing renewable energy penetration level drives power systems towards an era of inverter-dominated generation [14], where an inverter is a power electronic device that converts direct current (dc) electricity to alternating current (ac) electricity [15]. Although multiple power conversion

[1]The restoration of frequency to the nominal value requires a secondary control layer, e.g., automatic generation control [13], which is out of the scope of this thesis.

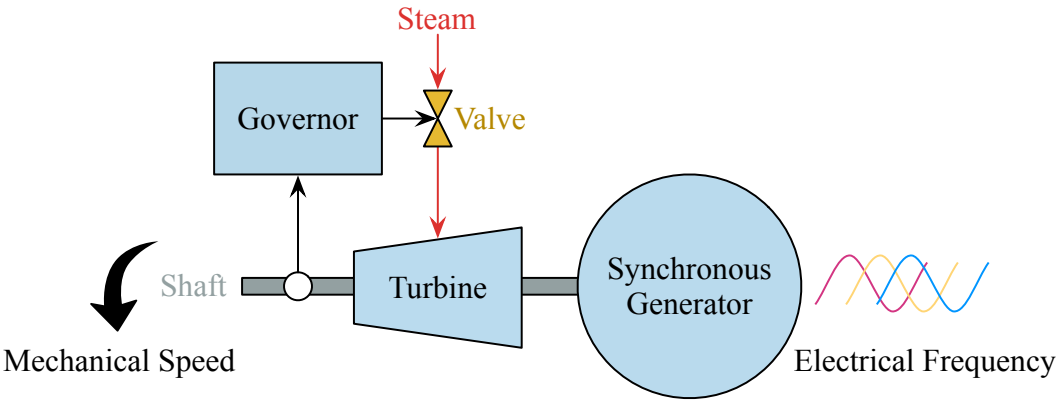

Figure 1.1: Scheme for turbine-governor

stages are needed to integrate renewable energy sources into grids, usually inverters are the ones that play the role of the final stage which directly interacts with the grid [16]. Figure 1.2 illustrates the typical way in which solar and wind energy are connected to the grid. Note that the main structure difference here is that solar energy is converted to dc electricity first but wind energy is converted to ac electricity first. A solar generation system begins with the process that photovoltaic arrays transform solar radiation into dc electricity. A wind generation system starts with the procedure that wind turbines capture kinetic energy from the wind blowing over their aerodynamic blades whose low-speed high-torque mechanical power is converted to high-speed low-torque mechanical power via a gearbox so as to drive an electric generator that produces ac electricity. However, neither the dc electricity produced in a solar generation system nor the ac electricity produced in a wind generation system can be integrated into the grid at this stage since their quality is highly susceptible to ambient conditions and incompatible with grid conditions. Firstly, to ensure the maximum power generation efficiency,

the "raw" dc electricity generated from sunlight and ac electricity generated from wind, after being filtered for reducing ripples, are regulated by a dc-dc converter and an ac-dc converter, respectively, to realize the maximum power point tracking under time-variant ambient conditions. Then, the obtained power is injected to a dc link capacitor, whose voltage is regulated by a following inverter to a constant value. Finally, the dc power is interfaced with the ac grid through the inverter, where an output filter and a step-up transformer are included to enable harmonics mitigation and voltage elevation. The structure described above makes it easy to understand the reduction of inertia in power systems as renewable energy penetration grows. Clearly, solar generation systems contribute no inertia since they have no moving parts at all. As for most modern wind generation systems, although wind turbines do have massive rotor blades, they fail to contribute inertia either since a by-product of the power electronics interface, which decouples the variable speed of the wind generator with the fixed frequency of the power grid in the normal operation, is that it prevents the kinetic energy stored in rotor blades from providing a buffer against rapid grid frequency changes when sudden power imbalances occur. With a lack of inertia in power systems, an exacerbated frequency deviation is required to recover the power balance. Therefore, care must be taken when replacing a significant amount of synchronous generators with renewable resources to avoid serious frequency dynamic degradation caused by reduced inertia. Notably, frequency dynamic degradation increases the risk of blackouts, which in turn places a limit on the total amount of renewable energy that can be sustained by power grids [17]. For example, an incident happened in Europe on January 8, 2021, where the grid of the

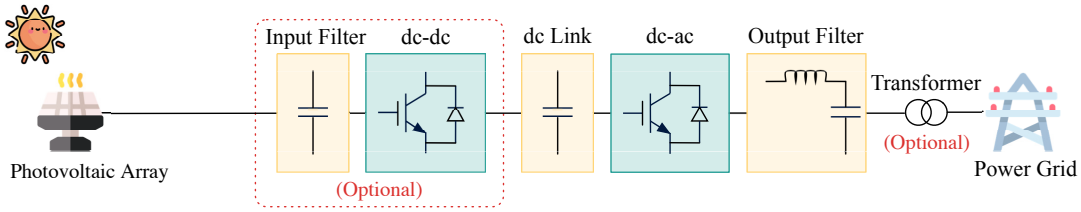

(a) Solar generation system

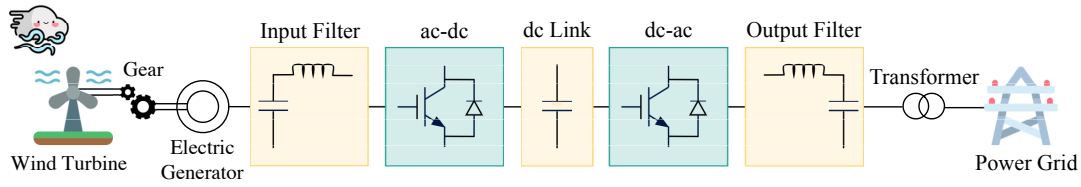

(b) Wind generation system

Figure 1.2: Typical structure of renewable energy systems [18]

continent split into two to elude a huge blackout in response to a power demand surge due to biting cold, is blamed on the rising renewables in the energy mix.

Fortunately, the recent technology advancement and cost reduction in energy storage facilitate the potential to enable higher renewable energy penetration by means of inverter-interfaced energy storage [19]. By virtue of the response rapidity and control flexibility, inverter-interfaced energy storage is deemed as a viable option for frequency control in power systems, where energy storage contributes to fast power-frequency response according to the control law imposed on inverters to compensate the possibly fast decline in frequency resulting from low-inertia. For example, an impressive 472 MW of storage has been reported to participate in the frequency control during the recent blackout caused by a lightning strike in the Great Britain system on

August 9, 2019 [20], where there was a cumulative loss of 1878 MW generation from the 32 GVA prior-contingency generation capacity available on the system.

Straightforwardly, a widely embraced control approach is to emulate the droop response and/or inertial response of synchronous generators through *droop control* (DC) and/or *virtual inertia* (VI) [21, 22]. DC only imitates the natural droop response of synchronous generators by modulating the inverter power output based on the local frequency measurement in a way that is proportional to the frequency deviation. VI also mimics the physical inertial response of synchronous generators through fast power exchange between the inverter and the grid by means of a proportional-derivative action upon the frequency deviation. In such settings, the inverter power output variation works as follows: its proportional component helps to continually resist any nonzero frequency deviation as droop response, while its derivative component injects power to the grid when the frequency decreases and absorbs power from the grid when the frequency increases, as inertial response, until the frequency settles down. Recent works within this line of research focus on leveraging either numerical methods [23–26] to optimize the allocation of synthetic inertial and droop responses or analytical methods to characterize the sensitivity of system performance to global or spatial variations of parameters of such approaches [27–29].

Nevertheless, the naive utilization of inverter-interfaced energy storage to emulate synchronous generator behavior does not take advantage of their full potential of implementing a much wider class of control actions. Presumably,

it need not be the case that synchronous generator behavior represents the optimal response to grid conditions since it is constrained by physical limits [11]. Particularly, inverter-interfaced energy storage has a much shorter time delay and higher ramp rate when compared with synchronous generators, which makes it a especially suitable provider for frequency control [30]. This, thus, opens the door for the search of better control approaches.

1.1 Thesis Contributions

The high level goal of our research is to develop novel control approaches that are able to largely improve the performance of prior methods. To this end, the main contributions of this thesis are as follows.

We build an analysis framework for quantifying the performance of power systems using signal and system norms, within which we perform a systematic study to evaluate the effect of different control laws on both frequency response metrics and storage economic metrics. More precisely, under a mild proportionality assumption, we are able to perform a modal decomposition which allows us to get closed-form expressions or conditions for synchronous frequency, Nadir, rate of change of frequency (RoCoF), synchronization cost, frequency variance, and steady-state effort share. All of them pave the way for a better understanding of the sensitivities of various performance metrics to different control laws.

Our analysis unveils several limitations of traditional control laws, such as the inability of DC to improve the dynamic performance without sacrificing the steady-state performance and the unbounded frequency variance

introduced by VI in the presence of frequency measurement noise. Therefore, rather than clinging to the idea of imitating synchronous generator behavior via inverter-interfaced energy storage, we prefer searching for better solutions.

We first propose *dynam-i-c Droop control* (iDroop) [31–33]—inspired by the classical lead/lag compensator—which is proved to enjoy many good properties. First of all, the added degrees of freedom in iDroop allow to decouple the dynamic performance improvement from the steady-state performance. In addition, the lead/lag property of iDroop makes it less sensitive to stochastic power fluctuations and frequency measurement noise. Last but not least, iDroop can also be tuned either to achieve zero synchronization cost or to achieve Nadir elimination, by which we mean to remove the overshoot in the transient system frequency. Particularly, the Nadir elimination tuning of iDroop exhibits the potential for a balance among various performance metrics in practice. However, iDroop has no control over the RoCoF, which is undesirable in low-inertia power systems for the risk of falsely triggering protections.

We then propose *frequency shaping control* (FS) [34, 35]—an extension of iDroop—whose most outstanding feature is its ability to shape the system frequency dynamics following a sudden power imbalance into a first-order one with the specified synchronous frequency and RoCoF by adjusting two independent control parameters.

We finally validate theoretical results through numerical experiments performed on a more realistic power system test case that violates the proportionality assumption, which clearly confirms that our proposed control laws

outperform the traditional ones in an overall sense.

1.2 Thesis Outline

The remainder of this thesis is organized as follows:

- Chapter 2 describes the power system model used here and defines some relevant frequency control metrics.
- Chapter 3 turns attention towards proportionally heterogeneous power systems, a reasonable first-cut approximation to generally heterogeneous power systems, where a modal decomposition can be done to extremely ease the performance analysis.
- Chapter 4 formally compares the performance of the traditional control laws—DC and VI—with that of our proposed control laws—iDroop and FS—for frequency control via inverter-interfaced energy storage, which serves as both a motivation and a justification for our research.
- Chapter 5 validates our theoretical results through a numerical example with more complex models for both the energy storage and the power system.
- Chapter 6 concludes this thesis.

Chapter 2

Model and Metrics for Frequency Control in Power Systems

This chapter describes the power system model used here and defines some relevant frequency control metrics. In Section 2.1, we build an one-bus system model from scratch, a simple yet useful characterization for many practical systems that are tightly electrically coupled. In Section 2.2, we generalize the one-bus system model to multi-bus system model by considering the effect of the transmission network. In Section 2.3, we introduce the mathematical definitions and physical interpretations of some signal and system norms which are then used to measure the performance of power systems under different frequency control laws based on inverter-interfaced energy storage through appropriately defined frequency response and storage economic metrics.

2.1 Model of One-Bus Systems

We start from the simple case where the inter-machine oscillations are negligible so that the whole power system can be modelled as an equivalent augmented synchronous generator, where, by "augmented", we mean that the effect of a turbine-governor is also considered. Such a representation is proven to be sufficiently accurate for many practical systems [36–38]. The dynamics of a synchronous generator can be characterized by the classical swing equation and the key features of a turbine-governor also can be captured by a simplified model. It is worth reproducing some of the derivation provided in [39, 40] for modelling such an augmented synchronous generator since it throws light on the physical interpretation of important jargon used by power system engineers. With the augmented synchronous generator model built up, we can gain a better understanding of the frequency dynamic degradation in low-inertia power systems by investigating an example of practical power systems, which motivates the participation of inverter-interfaced energy storage in frequency control.

2.1.1 Swing Equation

The motion of a synchronous generator obeys Newton's second law. Thus, the equation of motion is

$$J\dot{\Omega}_{\mathrm{m}} = T_{\mathrm{m}} - T_{\mathrm{e}}\,, \tag{2.1}$$

where J denotes the total moment of inertia (in $\mathrm{kg\,m^2}$), Ω_{m} the rotor mechanical angular velocity (in $\mathrm{rad\,s^{-1}}$), T_{m} the mechanical torque (in $\mathrm{N\,m}$), and T_{e}

the electrical torque (in N m).

It is convenient to express (2.1) in terms of the *inertia constant* H, which is defined as the normalized kinetic energy at the rated rotor mechanical angular velocity Ω_{m0} (in rad s^{-1}) on the rated apparent power base S_{B} (in VA), i.e.,

$$H := \frac{J\Omega_{\mathrm{m0}}^2}{2S_{\mathrm{B}}}\,. \tag{2.2}$$

Observe from (2.2) that the inertia constant H (in s) actually counts seconds during which the rated power can be supplied solely by the stored kinetic energy in the generator. Typically, H is in a narrow range of 1–10 s, which makes it a better choice than J for power system engineers to quantify the inertial response of a synchronous generator, given that J has a high variance between individual generators. After expressing J in terms of H though (2.2), we can rewrite (2.1) as

$$\frac{2HS_{\mathrm{B}}}{\Omega_{\mathrm{m0}}^2}\dot{\Omega}_{\mathrm{m}} = T_{\mathrm{m}} - T_{\mathrm{e}}\,. \tag{2.3}$$

Since what we care about is the deviation of the rotor mechanical angular velocity from its rated value, we will denote as ω_{m} the per unit deviation of the rotor mechanical angular velocity from its rated value, i.e.,

$$\omega_{\mathrm{m}} := \frac{\Omega_{\mathrm{m}} - \Omega_{\mathrm{m0}}}{\Omega_{\mathrm{m0}}}\,,$$

from which we can get

$$\dot{\Omega}_{\mathrm{m}} = \Omega_{\mathrm{m0}}\dot{\omega}_{\mathrm{m}}\,. \tag{2.4}$$

Applying (2.4) to (2.3), we can get

$$2H\dot{\omega}_{\mathrm{m}} = \frac{\Omega_{\mathrm{m0}}T_{\mathrm{m}} - \Omega_{\mathrm{m0}}T_{\mathrm{e}}}{S_{\mathrm{B}}}\,. \tag{2.5}$$

Note that usually the rotor mechanical angular velocity does not deviate from its rated value much, i.e., $\Omega_{\mathrm{m}} \approx \Omega_{\mathrm{m0}}$. Thus, we can rewrite (2.5) in terms of the mechanical input power from the turbine to the generator P_{m} (in W) and the electrical output power from the generator to the load P_{e} (in W) as

$$2H\dot{\omega}_{\mathrm{m}} \approx \frac{\Omega_{\mathrm{m}} T_{\mathrm{m}} - \Omega_{\mathrm{m}} T_{\mathrm{e}}}{S_{\mathrm{B}}} = \frac{P_{\mathrm{m}} - P_{\mathrm{e}}}{S_{\mathrm{B}}}\,. \tag{2.6}$$

If it is recognized that the steady-state values of P_{m} and P_{e}, denoted as $P_{\mathrm{m}\star}$ and $P_{\mathrm{e}\star}$, respectively, are equal, i.e., $P_{\mathrm{m}\star} = P_{\mathrm{e}\star}$, we can further rewrite (2.6) in terms of the per unit variations of the mechanical power input and the electrical power output from their respective steady-state values which are defined as

$$p_{\mathrm{m}} := \frac{P_{\mathrm{m}} - P_{\mathrm{m}\star}}{S_{\mathrm{B}}} \qquad \text{and} \qquad p_{\mathrm{e}} := \frac{P_{\mathrm{e}} - P_{\mathrm{e}\star}}{S_{\mathrm{B}}}\,, \tag{2.7}$$

respectively. Thus, combining (2.6) and (2.7), we can get

$$2H\dot{\omega}_{\mathrm{m}} = \frac{(P_{\mathrm{m}} - P_{\mathrm{m}\star}) - (P_{\mathrm{e}} - P_{\mathrm{e}\star})}{S_{\mathrm{B}}} = p_{\mathrm{m}} - p_{\mathrm{e}}\,. \tag{2.8}$$

The rotor electrical and mechanical angular velocities are related by the number of pairs of field poles n_{f} through the relations that

$$\Omega = n_{\mathrm{f}}\Omega_{\mathrm{m}} \qquad \text{and} \qquad \Omega_0 = n_{\mathrm{f}}\Omega_{\mathrm{m0}}\,, \tag{2.9}$$

where Ω and Ω_0 denote the true and rated rotor electrical velocities (in $\mathrm{rad\,s^{-1}}$), respectively. Hence, we can replace ω_{m} in (2.8) with the per unit

deviation of the rotor electrical angular velocity from its rated value ω since

$$\omega := \frac{\Omega - \Omega_0}{\Omega_0} = \frac{n_f \Omega_m - n_f \Omega_{m0}}{n_f \Omega_{m0}} = \frac{\Omega_m - \Omega_{m0}}{\Omega_{m0}} =: \omega_m \,, \tag{2.10}$$

which yields

$$2H\dot{\omega} = p_m - p_e \,. \tag{2.11}$$

Note that, due to (2.10), the per unit deviations of the rotor electrical angular velocity and rotor mechanical angular velocity from their respective rated values, namely, ω and ω_m, are used interchangeably from now on.

It is reasonable to separate p_e in (2.11) into two components as $p_e = p_l + \alpha_l \omega$, where the first term p_l represents the per unit non-frequency-sensitive load change, such as the one from lights and heaters, and the second term $\alpha_l \omega$ represents the per unit frequency-sensitive load change, such as the one from fans and pumps. Here, α_l is the *load-frequency sensitivity coefficient* (in p.u.) whose typical values are 0–2 p.u.. For example, $\alpha_l = 1$ p.u. means that a 1% frequency change results in a 1% load change.

Now, we can get the following classical *swing equation*

$$m\dot{\omega} = -\alpha_l \omega + p_m - p_l \qquad \text{with} \qquad m := 2H \,. \tag{2.12}$$

Here, with an abuse of terminology, m is also called generator inertia constant, which instead of $2H$ is used just for a clean notation. The above equation can also be represented by a transfer function as

$$\frac{\hat{\omega}}{\hat{p}_m - \hat{p}_l} = \frac{1}{ms + \alpha_l} \,, \tag{2.13}$$

[1]

[1] We use hat to distinguish the Laplace transform from its time domain counterpart.

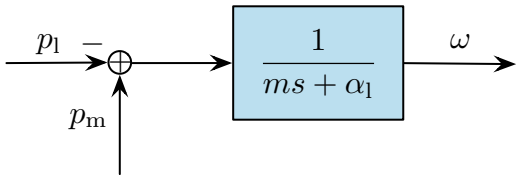

Figure 2.1: Block diagram of swing equation

whose block diagram is shown in Figure 2.1.

2.1.2 Turbine-Governor Dynamics

A turbine-governor varies mechanical power supply to synchronous generators after sensing mechanical speed deviations. Depending on turbine types and configurations, the detailed dynamics of a turbine-governor can be extremely high-order and nonlinear, which will be a barrier to our future analysis. Hence, we make a detour for tractable analysis by adopting the following simplified model that captures the key features of *turbine-governor dynamics* [41]:

$$\tau_{\mathrm{t}}\dot{p}_{\mathrm{m}} = -p_{\mathrm{m}} + \varphi_{\omega_\epsilon}(\omega) \tag{2.14}$$

with

$$\varphi_{\omega_\epsilon}(\omega) := \begin{cases} -\dfrac{1}{r_{\mathrm{t}}}(\omega+\omega_\epsilon) & \text{if } \omega \le -\omega_\epsilon \\ 0 & \text{if } -\omega_\epsilon < \omega < \omega_\epsilon \\ -\dfrac{1}{r_{\mathrm{t}}}(\omega-\omega_\epsilon) & \text{if } \omega_{\mathrm{m}} \ge \omega_\epsilon \end{cases},$$

where $\tau_{\mathrm{t}} > 0$ represents the *turbine time constant* (in s), $r_{\mathrm{t}} > 0$ represents the *turbine droop coefficient* (in p.u.), and $\omega_\epsilon \ge 0$ is the threshold of the deadband (in p.u.). To gain a better understanding of (2.14), we can turn it into the block diagram as shown in Figure 2.2, which is composed of a governor deadband, an inverse droop, and a first-order lag.

In general, a governor deadband is of two types: inherent and intentional [42]. An inherent deadband is the one resulting from uncontrollable mechanical effect such as sticky valves and loose gears. Experience shows that an inherent deadband is often within ± 5 mHz, corresponding to ± 0.0001 p.u. electrical frequency deviation on a 50 Hz base, which is negligible. An intentional deadband is the one designed to avoid mechanical wear due to excessive control activities in response to speed deviations, with which the governor does not react to the speed deviation ω until it exceeds a preset threshold $\pm\omega_\epsilon$. A standard value of ω_ϵ is 36 mHz, corresponding to 0.000 72 p.u. electrical frequency deviation on a 50 Hz base. Here, we consider an intentional deadband.

An inverse droop characterizes the droop response which feeds speed deviations back to adjust mechanical power output of the turbine by changing the valve position. More precisely, a negative feedback is used with the aim of raising mechanical power output if a sudden decrease in speed occurs and lowering mechanical power output if a sudden increase in speed occurs. Ideally, the variation of p_m with ω is determined by the control gain $1/r_\mathrm{t}$ which is the reciprocal of the turbine droop coefficient. Thus, it is often preferred to use the so-called *turbine inverse droop coefficient* $\alpha_\mathrm{t} := 1/r_\mathrm{t}$ (in p.u.), whose typical values are 10–20 p.u.. For example, $\alpha_\mathrm{t} = 20$ p.u., i.e., $r_\mathrm{t} = 0.05$ p.u., means that a 1% speed drop would cause a 20% increase in mechanical power output.

A first-order lag reflects the fact that the mechanical power output variation following the speed deviation does not occur instantaneously since the various

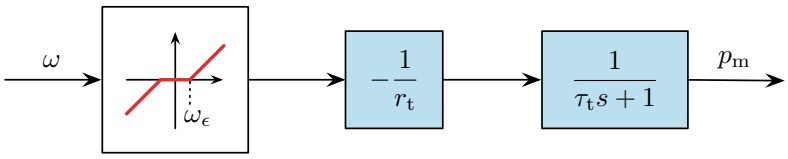

Figure 2.2: Block diagram of simplified turbine-governor dynamics

mechanical processes involved all take time. For instance, it would take a while for a change in the valve position to be effective in changing the mechanical power output of the turbine due to the gradual penetration of the flow from the valve into the turbine. Thus, we approximate such lags with a single turbine time constant τ_t.

2.1.3 Augmented Synchronous Generator Model

Now, we are ready to establish the augmented synchronous generator model after combining the swing equation in (2.12) and the turbine-governor dynamics in (2.14), which yields the block diagram shown in Figure 2.3. This model can be used to analyze the frequency performance of one-bus systems, where the electrical distances between different parts in a power system are negligible. In such systems, we can ignore the inter-machine oscillations and assume a coherent frequency among all generators. In other words, all generators are deemed to be locked together to form a grid frequency F (in Hz) determined by their common rotor electrical angular velocity Ω via $F = \Omega/(2\pi)$. This makes an equivalent single generator model shown in Figure 2.3 sufficient to represent the collective frequency performance of the whole system. Therein, the per unit deviation of the rotor electrical angular

velocity ω is exactly the per unit grid frequency deviation since

$$\frac{F - F_0}{F_0} = \frac{\Omega/(2\pi) - \Omega_0/(2\pi)}{\Omega_0/(2\pi)} = \frac{\Omega - \Omega_0}{\Omega_0} =: \omega\,,$$

where $F_0 := \Omega_0/(2\pi)$ denotes the nominal grid frequency (in Hz). This shows again the benefit of per unit analysis used by power system engineers. Note that, although it is convenient to use the per unit grid frequency deviation ω in analysis, we prefer to also use the true frequency deviation $f := F_0\omega$ when studying a practical system.

It worth noting that the parameters m, α_{l}, α_{t}, and τ_{t} of the equivalent generator are actually either accurate or approximate aggregates of parameters of all generators in such a system. More precisely, for a system with n generators, the aggregate generator inertia constant m and aggregate load-frequency sensitivity coefficient α_{l} are exactly the sum of the generator inertia constants and load-frequency sensitivity coefficients of all generators, respectively, i.e.,

$$m = \sum_{i=1}^{n} m_i \qquad \text{and} \qquad \alpha_{\mathrm{l}} = \sum_{i=1}^{n} \alpha_{\mathrm{l},i}\,,$$

where m_i and $\alpha_{\mathrm{l},i}$ denote the generator inertia constant and load-frequency sensitivity coefficient of the ith generator, respectively; however, α_{t} and τ_{t} are chosen to be the dc gain and time constant, respectively, of a first-order reduced model for the aggregate turbine-governor dynamics given by [43]

$$\sum_{i=1}^{n} \frac{\alpha_{\mathrm{t},i}}{\tau_{\mathrm{t},i}s + 1}\,,$$

where $\alpha_{\mathrm{t},i}$ is the ith turbine inverse droop coefficient, $\tau_{\mathrm{t},i}$ is the ith turbine time constant, and the individual governor deadbands are omitted for simplicity.

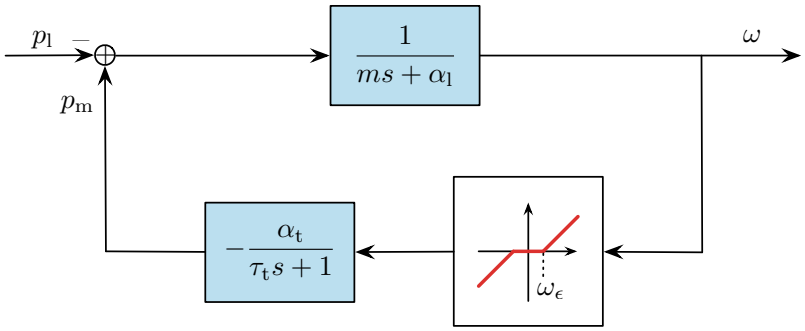

Figure 2.3: Block diagram of augmented synchronous generator model

Remark 2.1 (Change of Base). *Since individual generators in a power system may have different ratings, it is necessary to normalize their parameter values to a common base before conducting any analysis. A good rule of thumb for the change of base is to keep the actual value unchanged. For example, if* $m_{i,\mathrm{old}}$ *and* $\alpha_{\mathrm{l},i,\mathrm{old}}$ *are the generator inertia constant and load-frequency sensitivity coefficient, respectively, of the* i*th generator on its own power base* $S_{\mathrm{B},i,\mathrm{old}}$*, then we have to recalculate the per unit values on the power base of the whole system* S_B *as*

$$m_i = m_{i,\mathrm{old}}\frac{S_{\mathrm{B},i,\mathrm{old}}}{S_\mathrm{B}} \qquad \textit{and} \qquad \alpha_{\mathrm{l},i} = \alpha_{\mathrm{l},i,\mathrm{old}}\frac{S_{\mathrm{B},i,\mathrm{old}}}{S_\mathrm{B}}\,.$$

Therefore, throughout this thesis, all per unit values are on the system base by default, which means that we assume that they have been preprocessed properly by the change of base.

With the model provided in Figure 2.3, we can investigate the frequency performance of some practical systems as in the following example, which helps to offer a better insight of the frequency dynamic degradation in low-inertia power systems.

Example 2.1 (Great Britain Power System Under the Low-Inertia Scenario).

Consider the Great Britain power system modelled as the one-bus system shown in Figure 2.3 with parameter values taken mostly from [44, 45]. The system power base is $S_{\mathrm{B}} = 32\,\mathrm{GVA}$ *and the nominal system frequency is* $F_0 = 50\,\mathrm{Hz}$*. It is known that the present lowest value of the system inertia constant is* $H = 4.06\,\mathrm{s}$ *[44]. However, it is predicted that in 2025 the system inertia constant under the high renewable penetration scenario will be as low as* $H = 2.19\,\mathrm{s}$ *[44]. In addition, we assume that the aggregate load-frequency sensitivity coefficient is* $\alpha_{\mathrm{l}} = 1\,\mathrm{p.u.}$*, the aggregate turbine inverse droop coefficient is* $\alpha_{\mathrm{t}} = 15\,\mathrm{p.u.}$*, the turbine time constant is* $\tau_{\mathrm{t}} = 1\,\mathrm{s}$*, and the governor deadband is* $\pm 36\,\mathrm{mHz}$*, i.e.,* $\omega_\epsilon = 0.000\,72\,\mathrm{p.u.}$*. All parameter values are summarized in Table 2.1. To show the effect of lower inertia on frequency dynamics, Figure 2.4 provides a plot of system frequency deviations following a sudden power disturbance for the two different values of system inertia constant mentioned above. According to [45], the maximum value of a sudden power imbalance that the system should survive is* $|\mu_0|_{\mathrm{allowed}} = 0.0563\,\mathrm{p.u.}$ *which corresponds to the loss of the two biggest generation units. Thus, we test the case when* p_{l} *is a step increase with a magnitude of* $0.0563\,\mathrm{p.u.}$ *at time* $t = 1\,\mathrm{s}$*. Clearly, for the lower value of inertia, the transient frequency dip gets closer to* $500\,\mathrm{mHz}$*, the maximum allowed frequency drop for the Great Britain power system [44, 45]. Thus, certain measures should be taken to improve it.*

2.1.4 One-Bus System with Energy Storage

Since frequency deviation is volatile in a low-inertia power system, it is necessary to resort to certain measures to improve frequency performance, especially following major power disturbances. A promising approach to

Table 2.1: Parameter Values of Great Britain Power Systems (Example 2.1)

PARAMETERS	SYMBOLS	VALUES
Nominal frequency	F_0	50 Hz
System power base	S_B	32 GVA
Maximum power imbalance	$\lvert\mu_0\rvert_{\text{allowed}}$	0.0563 p.u.
System inertia constant	H	4.06 s in scenario 1 2.19 s in scenario 2
Aggregate load-frequency sensitivity coefficient	α_l	1 p.u.
Aggregate turbine inverse droop coefficient	α_t	15 p.u.
Turbine time constant	τ_t	1 s
Governor deadband threshold	ω_ϵ	0.000 72 p.u.

† All per unit values are on the system base.
‡ Recall that $m := 2H$.

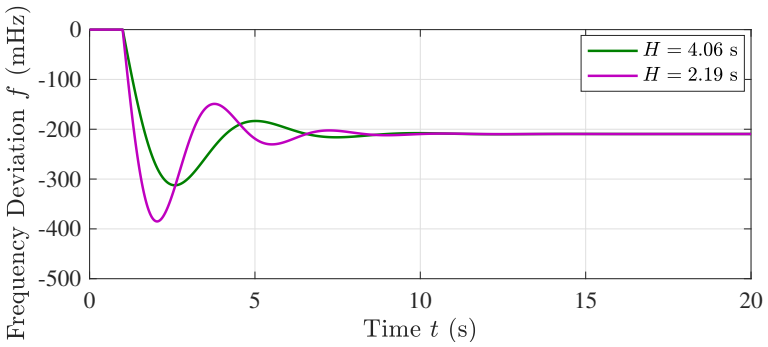

Figure 2.4: Frequency deviations in Great Britain system (Example 2.1)

mitigate this problem is to employ inverter-interfaced energy storage for frequency control [46]. The dynamics of inverter-interfaced energy storage is much faster than the electro-mechanical dynamics of conventional synchronous generators, which allows for more flexibility in frequency control. Here, we consider the most commonly used control mode of inverters—the "grid-following" mode—which adjusts inverter power output variation p_{b} (in p.u.) in certain ways directly following grid frequency deviation ω. The detailed way depends on the control law $\hat{c}(s)$ employed to map ω to p_{b}, with which the inverter power-frequency response can be described in Laplace domain as

$$\hat{p}_{\mathrm{b}} = \hat{c}(s)\hat{\omega}\,. \tag{2.15}$$

Note that two underlying assumptions are made. First, the measurement of the grid frequency is rather fast and accurate. Second, energy storage is able to follow power commands from inverter instantly and provide any shape of power response as long as it is within the installed capacity capability.

Then, we proceed to apply inverter-interfaced energy storage to the one-bus system by adding the feedback loop described in (2.15) to the augmented synchronous generator, which yields Figure 2.5.

2.2 Model of Multi-Bus Systems

With the model of one-bus systems paving the way, we now delve into the more general multi-bus systems which relax the previous assumption about the inter-machine oscillations. Thus, the case where different buses exhibit

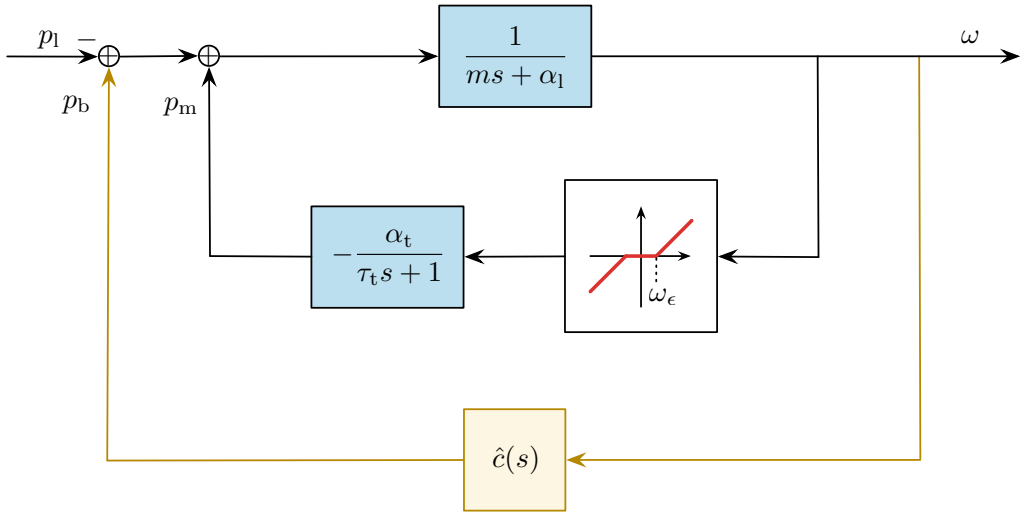

Figure 2.5: Block diagram of an one-bus system with energy storage

different frequencies can be tackled by considering the effect of the transmission network. To this end, we consider a n-bus system whose topology can be characterized by a weighted undirected connected graph $(\mathcal{V}, \mathcal{E})$, where buses indexed by $i, j \in \mathcal{V} := [n] := \{1, \ldots, n\}$ are linked through transmission lines denoted by unordered pairs $\{i, j\} \in \mathcal{E} \subset \{\{i, j\} \,|\, i, j \in \mathcal{V}, i \neq j\}$.[2] Here, some basic concepts from graph theory are involved.

Definition 2.1 (Undirected/Simple Graph). *A (simple) graph is an ordered pair $(\mathcal{V}, \mathcal{E})$, where $\mathcal{V}$ is a nonempty set of vertices and $\mathcal{E}$ is a set of 2-element subsets of $\mathcal{V}$, called edges.*[3]

Definition 2.2 (Walk). *A walk in a graph is a sequence of vertices such that any pair of consecutive vertices in the sequence is an edge of the graph.*

Definition 2.3 (Connectivity). *A graph is connected if there exists a walk between*

[2] Throughout this thesis, we use $[n]$ to denote the set of the first n positive integers. For example, $[3] = \{1, 2, 3\}$.

[3] A set is an unordered collection of distinct elements

any two vertices.

Remark 2.2 (Implications of Undirected/Simple Graphs). *Definition 2.1 actually implies that a (simple) graph has no self-loops, no parallel edges, and no orientation.*

As illustrated by the block diagram in Figure 2.6, assuming operation around an equilibrium, the system dynamics are modeled as a feedback interconnection of bus dynamics and network dynamics, where the input and output signals that are of most interest to us are power injection set point changes $\boldsymbol{p}_{\text{in}} := (p_{\text{in},i}, i \in [n]) \in \mathbb{R}^n$ (in p.u.) and bus frequency deviations from the nominal value $\boldsymbol{\omega} := (\omega_i, i \in [n]) \in \mathbb{R}^n$ (in p.u.), respectively.[4] We now discuss the dynamic elements in more detail.

As a note for clarification, we assume ideal grid conditions with neither imbalance nor harmonics, which allows a single-phase analysis. As usual, all per unit values are assumed to be on a common system base with a nominal frequency $F_0 := \Omega_0/(2\pi)$ as well as a power base S_{B} and a voltage base V_{B} specified, which uniquely determines the bases of remaining parameters and variables through the same relations as the one that their actual values satisfy.

2.2.1 Bus Dynamics

The bus dynamics that map net bus power imbalances $\boldsymbol{u}_{\text{p}} := \big(u_{\text{p},i}, i \in [n]\big) \in \mathbb{R}^n$ (in p.u.) to frequency deviations $\boldsymbol{\omega}$ are composed of n blocks, the ith of which represents the dynamics of the ith bus as shown in Figure 2.7. Observe

[4] Throughout this thesis, vectors are denoted in lower case bold and matrices are denoted in upper case bold, unless otherwise specified.

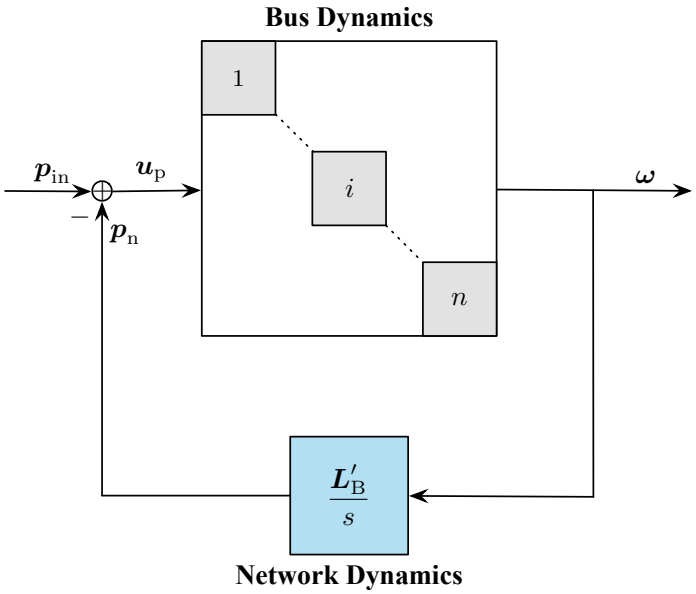

Figure 2.6: A multi-bus system model

from Figure 2.7 that each of the buses is in the same form as the model of an one-bus system with energy storage shown in Figure 2.5 except for a subscript i added to index the bus number. Thus, we can easily write the generator and inverter dynamics by referring to (2.12), (2.14), and (2.15).

Generator Dynamics The augmented synchronous generator dynamics on n buses can be stacked into a vector form as follows:

$$\boldsymbol{M}\dot{\boldsymbol{\omega}} = -\boldsymbol{A}_{\text{l}}\boldsymbol{\omega} + \boldsymbol{p}_{\text{m}} + \boldsymbol{p}_{\text{b}} + \boldsymbol{u}_{\text{p}}\,, \tag{2.16a}$$

$$\boldsymbol{T}_{\text{t}}\dot{\boldsymbol{p}}_{\text{m}} = -\boldsymbol{p}_{\text{m}} + \boldsymbol{\varphi}_{\omega_\epsilon}(\boldsymbol{\omega})\,, \tag{2.16b}$$

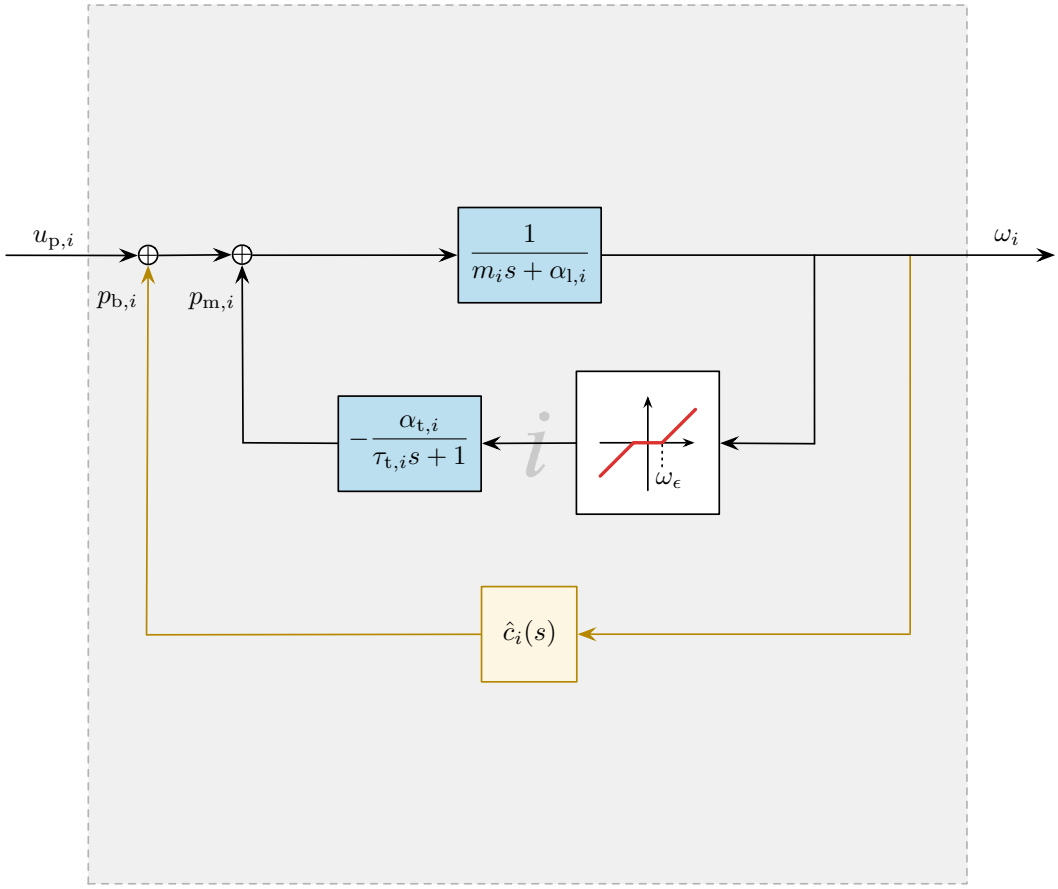

Figure 2.7: Block diagram of the ith bus dynamics

where $\boldsymbol{\varphi}_{\omega_\epsilon}(\boldsymbol{\omega})$ is a vector function of $\boldsymbol{\omega}$ with its ith term determined by

$$\varphi_{\omega_\epsilon,i}(\boldsymbol{\omega}) := \begin{cases} -\alpha_{\mathrm{t},i}(\omega_i + \omega_\epsilon) & \text{if } \omega_i \leq -\omega_\epsilon \\ 0 & \text{if } -\omega_\epsilon < \omega_i < \omega_\epsilon \\ -\alpha_{\mathrm{t},i}(\omega_i - \omega_\epsilon) & \text{if } \omega_i \geq \omega_\epsilon \end{cases}, \qquad \forall i \in [n] \ .$$

The meanings of all other parameters and variables should be clear from the definitions of their one-bus counterparts. Here, $\boldsymbol{M} := \mathrm{diag}\,(m_i, i \in [n]) \in \mathbb{R}^{n\times n}$, $\boldsymbol{A}_{\mathrm{l}} := \mathrm{diag}\,(\alpha_{\mathrm{l},i}, i \in [n]) \in \mathbb{R}^{n\times n}$, $\boldsymbol{T}_{\mathrm{t}} := \mathrm{diag}\,(\tau_{\mathrm{t},i}, i \in [n]) \in \mathbb{R}^{n\times n}$, $\boldsymbol{p}_{\mathrm{m}} := (p_{\mathrm{m},i}, i \in [n]) \in \mathbb{R}^n$, and $\boldsymbol{p}_{\mathrm{b}} := (p_{\mathrm{b},i}, i \in [n]) \in \mathbb{R}^n$, with $m_i > 0$, $\alpha_{\mathrm{l},i} > 0$, and $\tau_{\mathrm{t},i} \geq 0$, $\forall i \in [n]$.

Inverter Dynamics The dynamics of inverter-interfaced energy storage on n buses can be stacked into a vector form as follows:

$$\hat{\boldsymbol{p}}_{\mathrm{b}} = \hat{\boldsymbol{C}}(s)\hat{\boldsymbol{\omega}}\,, \tag{2.17}$$

where $\hat{\boldsymbol{C}}(s) := \mathrm{diag}\left(\hat{c}_i(s), i \in [n]\right)$.

2.2.2 Network Dynamics

The bread-and-butter issue that distinguishes multi-bus systems from one-bus systems is the unignorable effect of the transmission network, which plays a part in defining the physical relationship that system states—namely, voltage angle and magnitude as well as active and reactive power injections at each bus—should satisfy at an equilibrium. By conservation of complex power, at each bus, the difference between the complex power supplied and demanded from outside should match the net complex power drained into the transmission network at an equilibrium, which is the key idea conveyed by power flow equations. We now derive classic power flow equations following [47].

$\forall i \in [n]$, let the difference between the complex power supplied and demanded from outside at the ith bus be S_i (in p.u.). At an equilibrium, we have

$$P_i + \boldsymbol{j}Q_i = S_i = V_i\bar{I}_i\,.^{5} \tag{2.18}$$

Here, P_i and Q_i are the real and imaginary parts, respectively, of the rectangular representation for S_i, which correspond to active and reactive power injections (in p.u.), respectively, at the ith bus; V_i and I_i are the phasor voltage

[5] $\boldsymbol{j}$ represents the imaginary unit which satisfies $\boldsymbol{j}^2 = -1$; we use overline to denote the complex conjugate.

relative to ground and the phasor current injected to bus, respectively, at the ith bus, i.e.,

$$V_i := |V_i| e^{\boldsymbol{j}\angle V_i} \qquad \text{and} \qquad I_i := |I_i| e^{\boldsymbol{j}\angle I_i}\,, \tag{2.19}$$

which correspond to a sinusoidal voltage and current given by

$$v_i := |V_i| \cos\left(\Omega t + \angle V_i\right) \quad \text{and} \quad i_i := |I_i| \cos\left(\Omega t + \angle I_i\right),$$

respectively. Here, $|V_i|$ and $|I_i|$ are the root-mean-squared magnitudes (in p.u.) of v_i and i_i, respectively, which are equal to the peak values (in p.u.) of v_i and i_i, respectively, in the per unit system; $\angle V_i$ and $\angle I_i$ are the phases (in rad) of v_i and i_i, respectively.

Let $\boldsymbol{V} := (V_i, i \in [n]) \in \mathbb{C}^n$ and $\boldsymbol{I} := (I_i, i \in [n]) \in \mathbb{C}^n$. Then the following node equations should hold:

$$\boldsymbol{I} = \boldsymbol{Y}\boldsymbol{V}\,. \tag{2.20}$$

Here, $\boldsymbol{Y} := \left[Y_{ij}\right] \in \mathbb{C}^{n\times n}$ is the bus admittance matrix that can be constructed from the primitive parameters of a transmission network, whose ijth element can be put into a polar representation as

$$Y_{ij} := G_{ij} + \boldsymbol{j} B_{ij} \tag{2.21}$$

with G_{ij} and B_{ij} called conductance and susceptance (in p.u.), respectively.

Remark 2.3 (Structure of Bus Admittance Matrix). *The bus admittance matrix $\boldsymbol{Y}$ can be constructed from the primitive admittance of a transmission network in a standard way [47]. That is, $\forall i, j \in [n]$, if $i = j$, then Y_{ij}, called self admittance, is the sum of all primitive admittance connected to the ith bus; if $i \neq j$, then Y_{ij}, called*

mutual admittance, is the negative of the sum of all primitive admittance on $\{i,j\} \in \mathcal{E}$. *Actually, this construction implies the symmetry of* $\mathbf{Y}$, *i.e.,* $\forall i,j \in [n]$, $Y_{ij} = Y_{ji}$, *and the following pattern of sign in mutual admittance:* $\forall i \neq j$, *if* $\{i,j\} \notin \mathcal{E}$, *then* $G_{ij} = 0$ *and* $B_{ij} = 0$; *if* $\{i,j\} \in \mathcal{E}$, *then* $G_{ij} \leq 0$ *and* $B_{ij} \geq 0$, *not both zero.*

Applying the ith component of (2.20), i.e.,

$$I_i = \sum_{j=1}^{n} Y_{ij} V_j \,,$$

to (2.18) yields

$$P_i + \boldsymbol{j} Q_i = V_i \sum_{j=1}^{n} \overline{Y}_{ij} \overline{V}_j \,. \tag{2.22}$$

Substituting (2.19) and (2.21) to (2.22) gives

$$P_i + \boldsymbol{j} Q_i = \sum_{j=1}^{n} |V_i||V_j| \left(G_{ij} - \boldsymbol{j} B_{ij}\right) e^{\boldsymbol{j}\left(\angle V_i - \angle V_j\right)} \,. \tag{2.23}$$

It is convenient to define

$$\Theta_i := \angle V_i \,,$$

with which we can rewrite (2.23) as

$$P_i + \boldsymbol{j} Q_i = \sum_{j=1}^{n} |V_i||V_j| \left(G_{ij} - \boldsymbol{j} B_{ij}\right) \left[\cos\left(\Theta_i - \Theta_j\right) + \boldsymbol{j} \sin\left(\Theta_i - \Theta_j\right)\right] \tag{2.24}$$

using Euler's formula. Finally, we can separate (2.24) into real and imaginary parts as

$$P_i = \sum_{j=1}^{n} |V_i||V_j| \left[G_{ij} \cos\left(\Theta_i - \Theta_j\right) + B_{ij} \sin\left(\Theta_i - \Theta_j\right)\right] \,, \tag{2.25a}$$

$$Q_i = \sum_{j=1}^{n} |V_i||V_j| \left[G_{ij} \sin\left(\Theta_i - \Theta_j\right) - B_{ij} \cos\left(\Theta_i - \Theta_j\right)\right] \,, \tag{2.25b}$$

which are called *power flow equations*.

Observe from the right hand side of (2.25) that the power drained into the transmission network at each bus depends on voltage angle and magnitude of all buses, which makes the network dynamics nonlinear. Thus, to simplify analysis, we will adopt a linearized model to characterize the network dynamics, which implicitly makes the following assumptions well-justified for frequency control on transmission networks [39, 48].

Assumption 2.1 (Linearized Network Model Assumptions).

- *Lossless lines:* $\forall\{i,j\} \in \mathcal{E}$*, the line resistance is zero.*
- *Constant voltage profile:* $\forall i \in [n]$*, the bus voltage magnitude is constant.*
- *Decoupling: Reactive power flows do not affect bus voltage angles.*
- $\forall\{i,j\} \in \mathcal{E}$*, the equilibrium bus voltage angle difference is within* $\pm\pi/2$*.*

The lossless lines assumption agrees with the fact that the line resistance is negligible compared to the line inductance in transmission networks, which further implies that, $\forall i,j \in [n]$, $G_{ij} = 0$ by the way in which the bus admittance matrix is constructed. Then, (2.25) reduces to

$$P_i = \sum_{j=1}^{n} |V_i||V_j|B_{ij} \sin\left(\Theta_i - \Theta_j\right), \tag{2.26a}$$

$$Q_i = -\sum_{j=1}^{n} |V_i||V_j|B_{ij} \cos\left(\Theta_i - \Theta_j\right). \tag{2.26b}$$

The constant voltage profile assumption is reasonable since bus voltage magnitudes are kept within strict limits in normal operation. The decoupling

assumption takes advantage of the weak coupling between reactive power flows and bus voltage angles in normal operation. These two assumptions allow us to focus on the relationship between active power injections and bus voltage angles described by (2.26a), from which we can linearize the network dynamics around an equilibrium as

$$p_{\mathrm{n},i} = \sum_{j'=1}^{n} \left(\partial_{\Theta_{j'}} \sum_{j=1}^{n} |V_i||V_j|B_{ij} \sin(\Theta_i - \Theta_j) \Big|_{\boldsymbol{\Theta}=\boldsymbol{\Theta}_\star} \right) \theta_{j'} , \qquad \forall i \in [n] \ . \quad (2.27)$$

Here, $p_{\mathrm{n},i}$ is the deviation in the active power drained into the transmission network at the ith bus (in p.u.) and θ_i is the angle deviation at the ith bus (in rad) from the equilibrium angles $\boldsymbol{\Theta}_\star := (\Theta_{\star,i}, i \in [n]) \in \mathbb{R}^n$ of $\boldsymbol{\Theta} := (\Theta_i, i \in [n]) \in \mathbb{R}^n$.

We can stack (2.27) into a vector form by defining a weighted undirected *Laplacian matrix* $\boldsymbol{L}_{\mathrm{B}} = \left[L_{\mathrm{B},ij}\right] \in \mathbb{R}^{n\times n}$ of the network whose ij'th element is

$$L_{\mathrm{B},ij'} = \partial_{\Theta_{j'}} \sum_{j=1}^{n} |V_i||V_j|B_{ij} \sin(\Theta_i - \Theta_j) \Big|_{\boldsymbol{\Theta}=\boldsymbol{\Theta}_\star} , \quad (2.28)$$

which yields

$$\boldsymbol{p}_{\mathrm{n}} = \boldsymbol{L}_{\mathrm{B}} \boldsymbol{\theta} \quad (2.29)$$

with $\boldsymbol{p}_{\mathrm{n}} := (p_{\mathrm{n},i}, i \in [n]) \in \mathbb{R}^n$ and $\boldsymbol{\theta} := (\theta_i, i \in [n]) \in \mathbb{R}^n$. Finally, since we care more about $\boldsymbol{\omega}$ than $\boldsymbol{\theta}$, we now involve $\boldsymbol{\omega}$ in the model via

$$\dot{\boldsymbol{\theta}} = \Omega_0 \boldsymbol{\omega} \, . \quad (2.30)$$

Thus, (2.29) and (2.30) together characterize the linearized model of network dynamics that map frequency deviations $\boldsymbol{\omega}$ to network power deviations $\boldsymbol{p}_{\mathrm{n}}$,

which can also be described in Laplace domain as

$$\hat{\boldsymbol{p}}_{\mathrm{n}} = \frac{\boldsymbol{L}'_{\mathrm{B}}}{s}\hat{\boldsymbol{\omega}} \qquad \text{with} \qquad \boldsymbol{L}'_{\mathrm{B}} := \Omega_0 \boldsymbol{L}_{\mathrm{B}} \,. \tag{2.31}$$

Notably, since throughout the modelling process we consider power drained into the network, we need to add the block description of network dynamics given by (2.31) as a negative feedback loop in Figure 2.6.

One might be curious about the need for the last assumption about equilibrium bus voltage angle differences in Assumption 2.1, i.e., $\forall\{i,j\} \in \mathcal{E}$, $-\pi/2 < \Theta_{\star,i} - \Theta_{\star,j} < \pi/2$, since it has never been used up to now. Actually, it is made to ensure that $\boldsymbol{L}_{\mathrm{B}}$ is a well-defined Laplacian matrix. Prior to a detailed explanation of this, we need to introduce the definition of a Laplacian matrix.

Definition 2.4 (Laplacian Matrix of a Weighted Undirected Graph). *Given a weighted undirected graph $(\mathcal{V},\mathcal{E})$ with $\mathcal{V} = [n]$, $\mathcal{E} \subset \{\{i,j\} \,|\, i,j \in \mathcal{V}, i \neq j\}$, and a weight matrix $\boldsymbol{W} := \left[W_{ij}\right] \in \mathbb{R}^{n\times n}$ such that*

$$W_{ij} = \begin{cases} W_{ji} > 0 & \text{if } \{i,j\} \in \mathcal{E} \\ 0 & \text{if } \{i,j\} \notin \mathcal{E} \end{cases}, \qquad \forall i,j \in [n] \,, \tag{2.32}$$

the Laplacian matrix $\boldsymbol{L} := \left[L_{ij}\right] \in \mathbb{R}^{n\times n}$ of $(\mathcal{V},\mathcal{E})$ is defined as a matrix whose ijth element is

$$L_{ij} := \begin{cases} -W_{ij} & \text{if } i \neq j \\ \displaystyle\sum_{j'=1, j'\neq i}^{n} W_{ij'} & \text{if } i = j \end{cases}, \qquad \forall i,j \in [n] \,. \tag{2.33}$$

Remark 2.4 (Independence from Diagonal Weights). *From (2.33), it is easy to*

see that the Laplacian matrix of a graph is independent of diagonal entries of the weight matrix. Thus, from the perspective of Laplacian matrix, we can always assume zero diagonal weights without loss of generality which is an assumption naturally needed in a (simple) graph for consistency with the fact of no self-loops.

We now quickly check that $\boldsymbol{L}_{\mathrm{B}}$ built in (2.28) is a well-defined Laplacian matrix under the assumption that, $\forall\{i,j\} \in \mathcal{E}$, $-\pi/2 < \Theta_{\star,i} - \Theta_{\star,j} < \pi/2$, using Definition 2.4. A simple calculation shows that the explicit expression for the ijth element of $\boldsymbol{L}_{\mathrm{B}}$ is

$$L_{\mathrm{B},ij} = \begin{cases} -|V_i||V_j|B_{ij}\cos(\Theta_{\star,i} - \Theta_{\star,j}) & \text{if } i \neq j \\ \displaystyle\sum_{j'=1,j'\neq i}^{n} |V_i||V_{j'}|B_{ij'}\cos(\Theta_{\star,i} - \Theta_{\star,j'}) & \text{if } i = j \end{cases}, \qquad \forall i,j \in [n]\ ,$$

which is in the same format as (2.33) with

$$W_{ij} := |V_i||V_j|B_{ij}\cos(\Theta_{\star,i} - \Theta_{\star,j})\,, \qquad \forall i \neq j\,.$$

Thus, $\boldsymbol{L}_{\mathrm{B}}$ can be considered as the Laplacian matrix associated with the weight matrix $\boldsymbol{W}$ defined as

$$W_{ij} := \begin{cases} |V_i||V_j|B_{ij}\cos(\Theta_{\star,i} - \Theta_{\star,j}) & \text{if } i \neq j \\ 0 & \text{if } i = j \end{cases}, \qquad \forall i,j \in [n]\ . \tag{2.34}$$

It remains to be shown that (2.34) produces a well-defined weight matrix $\boldsymbol{W}$ that satisfies (2.32) for the graph $(\mathcal{V},\mathcal{E})$ underlying the n-bus system. Clearly, $\forall i,j \in [n]$, $|V_i| > 0$, $|V_j| > 0$. We then divide our analysis of W_{ij} according to diagonal and off-diagonal terms. For the case that $i = j$, we have $\{i,j\} \notin \mathcal{E}$ and $W_{ij} = 0$. For the case that $i \neq j$, if $\{i,j\} \notin \mathcal{E}$, then

$W_{ij} = |V_i||V_j|B_{ij}\cos(\Theta_{\star,i} - \Theta_{\star,j}) = 0$ since $B_{ij} = 0$ by Remark 2.3; if $\{i,j\} \in \mathcal{E}$, then $W_{ij} = |V_i||V_j|B_{ij}\cos(\Theta_{\star,i} - \Theta_{\star,j}) = |V_j||V_i|B_{ji}\cos(\Theta_{\star,j} - \Theta_{\star,i}) = W_{ji} > 0$ since $B_{ij} = B_{ji} > 0$ by Remark 2.3 and $\cos(\Theta_{\star,i} - \Theta_{\star,j}) = \cos(\Theta_{\star,j} - \Theta_{\star,i}) > 0$ by our assumption that $-\pi/2 < \Theta_{\star,i} - \Theta_{\star,j} < \pi/2$. Thus, both cases match (2.32), which means that $\boldsymbol{W}$ is a well-defined weight matrix on $(\mathcal{V}, \mathcal{E})$. Therefore, $\boldsymbol{L}_{\mathrm{B}}$ built in (2.28) is a well-defined Laplacian matrix.

Trivially, $\boldsymbol{L}'_{\mathrm{B}}$ in (2.31) is a well-defined Laplacian matrix on the graph $(\mathcal{V}, \mathcal{E})$ with the weight matrix $\Omega_0 \boldsymbol{W}$. As a Laplacian matrix, $\boldsymbol{L}'_{\mathrm{B}}$ enjoys many useful properties, some of which are [49]:

- Symmetry, i.e., $\boldsymbol{L}'_{\mathrm{B}} = \boldsymbol{L}'^{T}_{\mathrm{B}}$. This ensures that $\boldsymbol{L}'_{\mathrm{B}}$ is real orthogonally diagonalizable [50].
- Each row sums to 0, i.e., $\boldsymbol{L}'_{\mathrm{B}}\mathbf{1}_n = \mathbf{0}_{n\times 1}$, where $\mathbf{1}_n \in \mathbb{R}^n$ is the vector of all 1's. This implies that 0 is an eigenvalue of $\boldsymbol{L}'_{\mathrm{B}}$ associated with eigenvector $\mathbf{1}_n$.
- Eigenvalues different from 0 lie on the open right half plane by the Gersgorin disks theorem.
- The algebraic multiplicity of the 0 eigenvalue is 1 since the graph $(\mathcal{V}, \mathcal{E})$ is connected.

It follows from above properties that $\boldsymbol{L}'_{\mathrm{B}}$ is real orthogonally diagonalizable with eigenvalues satisfying $0 = \lambda_1(\boldsymbol{L}'_{\mathrm{B}}) < \lambda_2(\boldsymbol{L}'_{\mathrm{B}}) \leq \ldots \leq \lambda_n(\boldsymbol{L}'_{\mathrm{B}})$.

2.2.3 Closed-Loop Dynamics

Heretofore our focus is to prepare ourselves for investigating the closed-loop response of the n-bus system in Figure 2.6 from the power injection set

point changes $\boldsymbol{p}_{\text{in}}$ to frequency deviations $\boldsymbol{\omega}$, which could help us to estimate the ability of the system to reject a sudden power imbalance that might be caused by a loss of generation units or a spike in load demands. However, apart from this disturbance rejection capability, the sensitivity of the system to stochastic power fluctuations and frequency measurement noise also matters. Thus, we will dwell further on this by introducing two additional input signals to the n-bus system as shown in Figure 2.8, where, for the ease of presentation, the block diagram of the bus dynamics is redrawn as a feedback loop that comprises a forward-path $\hat{\boldsymbol{G}}(s) := \text{diag}\left(\hat{g}_i(s), i \in [n]\right)$ and a feedback-path $\hat{\boldsymbol{C}}(s) := \text{diag}\left(\hat{c}_i(s), i \in [n]\right)$ representing the transfer function matrices of generators and inverters, respectively. The input signal $\boldsymbol{n}_{\text{p}} := \left(n_{\text{p},i}, i \in [n]\right) \in \mathbb{R}^n$ (in p.u.) that represents stochastic power fluctuations is injected on top of $\boldsymbol{p}_{\text{in}}$, while the input signal $\boldsymbol{n}_{\omega} := (n_{\omega,i}, i \in [n]) \in \mathbb{R}^n$ (in p.u.) that represents frequency measurement noise originates in sensors involved in grid-following inverters. The weighting functions $\hat{\boldsymbol{W}}_{\text{p}}(s)$ and $\hat{\boldsymbol{W}}_{\omega}(s)$ can be used to adjust the magnitudes of these two signals in the usual way.

As our analysis of the effect of different control laws on system performance unfolds, it should be clear that the key lies in an examination of the closed-loop responses of the system in Figure 2.8 from $\boldsymbol{p}_{\text{in}}$, $\boldsymbol{n}_{\text{p}}$, and $\boldsymbol{n}_{\omega}$ to $\boldsymbol{\omega}$, which can be described compactly by the transfer function matrix

$$\hat{\boldsymbol{T}}_{\text{sys}}(s) := \begin{bmatrix} \hat{\boldsymbol{T}}_{\omega\text{p}}(s) & \hat{\boldsymbol{T}}_{\omega\text{n}}(s) \end{bmatrix} := \begin{bmatrix} \hat{\boldsymbol{T}}_{\omega\text{n}_{\text{p}}}(s) & \hat{\boldsymbol{T}}_{\omega\text{n}_{\omega}}(s) \end{bmatrix} . \tag{2.35}$$

Last but not least, the linear model in (2.35) relies on the following assumption on the augmented synchronous generator dynamics on each bus in the

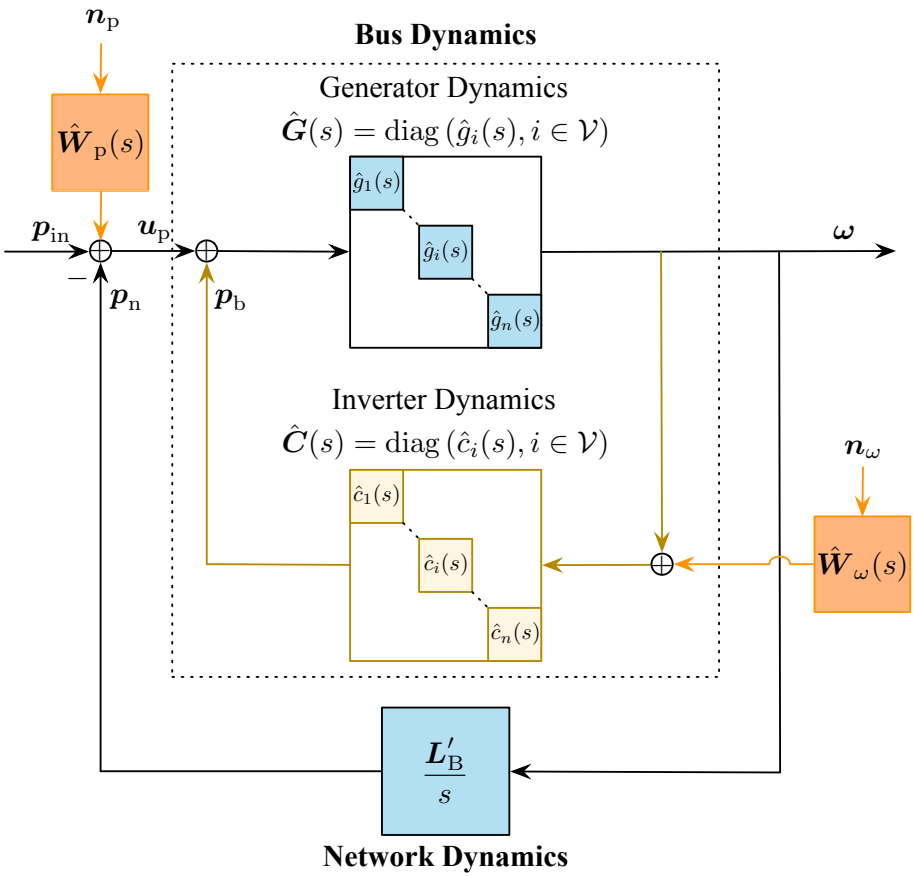

Figure 2.8: A linearized model of the multi-bus system

system shown in Figure 2.6.

Assumption 2.2 (Scenario-Based Generator Dynamics). *Whenever the system shown in Figure 2.6 is excited solely by:*

- $\boldsymbol{p}_{\text{in}}$*, then* $\omega_\epsilon = 0$ *such that turbine-governors are constantly triggered;*
- $\boldsymbol{n}_{\text{p}}$ *and* $\boldsymbol{n}_\omega$*, then* $|\omega_i(t)| < \omega_\epsilon$*,* $\forall\, i \in [n]$ *and* $t \geq 0$*, such that turbine-governors will not be triggered.*

Assumption 2.2 extremely simplifies our analysis by removing the nonlinearity introduced to (2.16) by governor deadbands. Under this assumption, the generator dynamics that are of our interest fall into two cases:

Generator Dynamics 1 (Standard Swing Dynamics). *When turbine-governors are not triggered, the generator dynamics can be described by the transfer function*

$$\hat{g}_i(s) = \frac{1}{m_i s + \alpha_{\text{l},i}}\,, \qquad \forall i \in [n]\ . \tag{2.36}$$

Generator Dynamics 2 (Second-Order Generator Dynamics). *When turbine-governors are constantly triggered, the generator dynamics can be described by the transfer function*

$$\hat{g}_i(s) = \frac{\tau_{\text{t},i} s + 1}{m_i \tau_{\text{t},i} s^2 + (m_i + \alpha_{\text{l},i}\tau_{\text{t},i})\, s + \alpha_{\text{l},i} + \alpha_{\text{t},i}}\,, \qquad \forall i \in [n]\ . \tag{2.37}$$

2.3 Performance Metrics

Having built up the model of the power system, we are now ready to introduce performance metrics used in this thesis to compare different frequency control laws.

2.3.1 Signal and System Norms

Signal and system norms are useful measures for evaluating performance of a control system. Thus, we begin with definitions of some relevant norms that are appropriate to the characterization of power system performance under different frequency control laws.

Definition 2.5 ($\mathcal{L}_2$ Norm of a Signal [51]). *For a vector-valued time-varying signal $\boldsymbol{y} := (y_i(t), i \in [n]) \in \mathbb{R}^n$, the $\mathcal{L}_2$ norm of $\boldsymbol{y}$ is*

$$\|\boldsymbol{y}\|_{\mathcal{L}_2} := \sqrt{\sum_{i=1}^{n} \int_{-\infty}^{\infty} |y_i(t)|^2 \mathrm{d}t} = \sqrt{\int_{-\infty}^{\infty} \boldsymbol{y}(t)^T \boldsymbol{y}(t) \mathrm{d}t} \,.$$

Definition 2.6 ($\mathcal{L}_\infty$ Norm of a Signal [51]). *For a vector-valued time-varying signal $\boldsymbol{y} := (y_i(t), i \in [n]) \in \mathbb{R}^n$, the $\mathcal{L}_\infty$ norm of $\boldsymbol{y}$ is*

$$\|\boldsymbol{y}\|_{\mathcal{L}_\infty} := \max_t \max_{i \in [n]} |y_i(t)| \,,$$

supposing the maximum value exists.

Definition 2.7 ($\mathcal{H}_2$ Norm of a System [51]). *For a multi-input multi-output linear system with a strictly proper stable transfer function matrix $\hat{\boldsymbol{T}}(s)$, the $\mathcal{H}_2$ norm of $\hat{\boldsymbol{T}}(s)$ is*

$$\|\hat{\boldsymbol{T}}\|_{\mathcal{H}_2} := \sqrt{\frac{1}{2\pi} \int_{-\infty}^{\infty} \mathrm{tr}\left(\hat{\boldsymbol{T}}(j\dot{\omega})^* \hat{\boldsymbol{T}}(j\dot{\omega})\right) \mathrm{d}\dot{\omega}} = \sqrt{\int_{-\infty}^{\infty} \mathrm{tr}\left(\boldsymbol{T}(t)^T \boldsymbol{T}(t)\right) \mathrm{d}t} \,,$$ [6]

where the second equality is by Parseval's theorem.

[6] We use $\dot{\omega}$ rather than ω to denote the frequency variable in mathematics in order to distinguish it from the per unit grid frequency deviation ω; we use $*$ to denote the conjugate transpose.

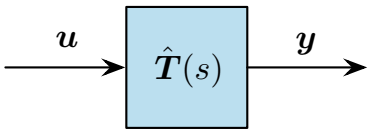

Figure 2.9: A linear system

Remark 2.5 (Right-Sided Signals and Causal Systems). *In most cases, we assume signals are right-sided, i.e.,* $\boldsymbol{y}(t) = \mathbf{0}_{n\times 1}, \forall t < 0$, *and systems are causal, i.e.,* $\boldsymbol{T}(t) = \mathbf{0}, \forall t < 0$, *which means that the integrals with respect to time t are taken only over* $[0, \infty]$ *in above definitions.*

We can see from above definitions that the $\mathcal{L}_2$ norm quantifies the "energy" of a signal while the $\mathcal{L}_\infty$ norm quantifies the "peak" of a signal. As for the $\mathcal{H}_2$ norm, we can interpret it as a norm of a system response resulting from certain input signals [51, 52]. To see this, consider the linear system in Figure 2.9, where there is a strictly proper stable transfer function matrix $\hat{\boldsymbol{T}}(s)$ from the input signal $\boldsymbol{u} := (u_i(t), i \in [n_1]) \in \mathbb{R}^{n_1}$ to the output signal $\boldsymbol{y} := (y_i(t), i \in [n_2]) \in \mathbb{R}^{n_2}$. Then, the norm of the output signal $\boldsymbol{y}$ can yield both deterministic and stochastic interpretations of the $\mathcal{H}_2$ norm of the system $\hat{\boldsymbol{T}}(s)$, depending on the choice for the input signal $\boldsymbol{u}$ that the system is subject to.

A Deterministic Interpretation of the $\mathcal{H}_2$ Norm Suppose $\boldsymbol{u}$ is a series of unit impulses. That is, $\forall i \in [n_1]$, at the ith experiment, apply $\boldsymbol{u} = \delta(t)\boldsymbol{e}_i$ to $\hat{\boldsymbol{T}}(s)$, where $\delta(t)$ is the unit-impulse function and $\boldsymbol{e}_i \in \mathbb{R}^{n_1}$ is the vector with a 1 in the ith coordinate and 0's elsewhere. Then the sum of the squared $\mathcal{L}_2$ norms of $\boldsymbol{y}$ over all n_1 experiments results in the squared $\mathcal{H}_2$ norm of $\hat{\boldsymbol{T}}(s)$

since

$$\sum_{j=1}^{n_1} \| \boldsymbol{y}|_{\boldsymbol{u}=\delta(t)\boldsymbol{e}_j} \|_{\mathcal{L}_2}^2 = \sum_{j=1}^{n_1} \|\boldsymbol{T}(t)\boldsymbol{e}_j\|_{\mathcal{L}_2}^2 := \sum_{j=1}^{n_1}\sum_{i=1}^{n_2} \int_0^\infty |T_{ij}(t)|^2 \mathrm{d}t$$

$$= \int_0^\infty \sum_{j=1}^{n_1}\sum_{i=1}^{n_2} |T_{ij}(t)|^2 \mathrm{d}t = \int_0^\infty \operatorname{tr}\left(\boldsymbol{T}(t)^T\boldsymbol{T}(t)\right) \mathrm{d}t =: \|\hat{\boldsymbol{T}}\|_{\mathcal{H}_2}^2 .$$

A Stochastic Interpretation of the $\mathcal{H}_2$ Norm Suppose $\boldsymbol{u}$ is white noise of unit intensity, i.e., $\mathbb{E}\left[\boldsymbol{u}(t)\boldsymbol{u}(\tau)^T\right] = \delta(t-\tau)\boldsymbol{I}_{n_1}$. Then the sum of the steady-state variances of all elements in $\boldsymbol{y}$ leads to the squared $\mathcal{H}_2$ norm of $\hat{\boldsymbol{T}}(s)$ since

$$\begin{aligned}
&\lim_{t\to\infty} \mathbb{E}\left[\boldsymbol{y}(t)^T\boldsymbol{y}(t)\right] \\
&= \lim_{t\to\infty} \operatorname{tr}\left(\mathbb{E}\left[\boldsymbol{y}(t)\boldsymbol{y}(t)^T\right]\right) \\
&= \lim_{t\to\infty} \operatorname{tr}\left(\mathbb{E}\left[\int_0^t \boldsymbol{T}(\tau_1)\boldsymbol{u}(t-\tau_1)\mathrm{d}\tau_1 \int_0^t \boldsymbol{u}(t-\tau_2)^T\boldsymbol{T}(\tau_2)^T\mathrm{d}\tau_2\right]\right) \\
&= \lim_{t\to\infty} \operatorname{tr}\left(\int_0^t \boldsymbol{T}(\tau_1)\int_0^t \mathbb{E}\left[\boldsymbol{u}(t-\tau_1)\boldsymbol{u}(t-\tau_2)^T\right]\boldsymbol{T}(\tau_2)^T\mathrm{d}\tau_2\mathrm{d}\tau_1\right) \\
&= \lim_{t\to\infty} \operatorname{tr}\left(\int_0^t \boldsymbol{T}(\tau_1)\int_0^t \delta(\tau_2-\tau_1)\boldsymbol{T}(\tau_2)^T\mathrm{d}\tau_2\mathrm{d}\tau_1\right) \\
&= \lim_{t\to\infty} \operatorname{tr}\left(\int_0^t \boldsymbol{T}(\tau_1)\boldsymbol{T}(\tau_1)^T\mathrm{d}\tau_1\right) = \operatorname{tr}\left(\int_0^\infty \boldsymbol{T}(\tau_1)\boldsymbol{T}(\tau_1)^T\mathrm{d}\tau_1\right) \\
&= \int_0^\infty \operatorname{tr}\left(\boldsymbol{T}(\tau_1)\boldsymbol{T}(\tau_1)^T\right)\mathrm{d}\tau_1 = \int_0^\infty \operatorname{tr}\left(\boldsymbol{T}(\tau_1)^T\boldsymbol{T}(\tau_1)\right)\mathrm{d}\tau_1 =: \|\hat{\boldsymbol{T}}\|_{\mathcal{H}_2}^2 .
\end{aligned}$$

Given any state-space realization of $\hat{\boldsymbol{T}}(s)$, the $\mathcal{H}_2$ norm can be calculated

by solving a particular Lyapunov equation [51, 52]. More specifically, suppose

$$\Sigma_{\hat{\boldsymbol{T}}(s)} = \left[\begin{array}{c|c} \boldsymbol{A} & \boldsymbol{B} \\ \hline \boldsymbol{C} & \boldsymbol{D} \end{array}\right], \qquad \text{i.e.,} \qquad \hat{\boldsymbol{T}}(s) = \boldsymbol{C}\left(s\boldsymbol{I} - \boldsymbol{A}\right)^{-1}\boldsymbol{B} + \boldsymbol{D}\,.$$

For strictly proper $\hat{\boldsymbol{T}}(s)$, i.e., $\boldsymbol{D} = \boldsymbol{0}_{n_2\times n_1}$, we have

$$\begin{aligned}\|\hat{\boldsymbol{T}}\|_{\mathcal{H}_2}^2 :=& \int_0^\infty \mathrm{tr}\left(\boldsymbol{T}(t)^T\boldsymbol{T}(t)\right)\mathrm{d}t = \int_0^\infty \mathrm{tr}\left(\boldsymbol{T}(t)\boldsymbol{T}(t)^T\right)\mathrm{d}t \\ =&\mathrm{tr}\left(\int_0^\infty \boldsymbol{T}(t)\boldsymbol{T}(t)^T\mathrm{d}t\right) = \mathrm{tr}\left(\int_0^\infty \boldsymbol{C}e^{\boldsymbol{A}t}\boldsymbol{B}\boldsymbol{B}^Te^{\boldsymbol{A}^Tt}\boldsymbol{C}^T\mathrm{d}t\right) \\ =&\mathrm{tr}\left(\boldsymbol{C}\boldsymbol{X}\boldsymbol{C}^T\right),\end{aligned}$$

where

$$\boldsymbol{X} := \int_0^\infty e^{\boldsymbol{A}t}\boldsymbol{B}\boldsymbol{B}^Te^{\boldsymbol{A}^Tt}\mathrm{d}t\,. \tag{2.38}$$

Note that $\boldsymbol{X}$ defined in (2.38) is an important matrix called *controllability Gramian* in control theory, which can be obtained as the unique solution to the following *Lyapunov equation*

$$\boldsymbol{A}\boldsymbol{X} + \boldsymbol{X}\boldsymbol{A}^T = -\boldsymbol{B}\boldsymbol{B}^T \tag{2.39}$$

if $\boldsymbol{A}$ is asymptotically stable.[7] A standard way to verify that $\boldsymbol{X}$ satisfies (2.39) utilizes the fact that

$$\frac{\mathrm{d}}{\mathrm{d}t}e^{\boldsymbol{A}t}\boldsymbol{B}\boldsymbol{B}^Te^{\boldsymbol{A}^Tt} = \boldsymbol{A}e^{\boldsymbol{A}t}\boldsymbol{B}\boldsymbol{B}^Te^{\boldsymbol{A}^Tt} + e^{\boldsymbol{A}t}\boldsymbol{B}\boldsymbol{B}^Te^{\boldsymbol{A}^Tt}\boldsymbol{A}^T\,. \tag{2.40}$$

[7] A matrix is asymptotically stable if all its eigenvalues have negative real parts.

Integrating both sides of (2.40) with respect to t over $[0, \infty]$ yields

$$e^{\boldsymbol{A}t}\boldsymbol{B}\boldsymbol{B}^T e^{\boldsymbol{A}^T t}\Big|_0^\infty = \boldsymbol{A}\int_0^\infty e^{\boldsymbol{A}t}\boldsymbol{B}\boldsymbol{B}^T e^{\boldsymbol{A}^T t}\mathrm{d}t + \int_0^\infty e^{\boldsymbol{A}t}\boldsymbol{B}\boldsymbol{B}^T e^{\boldsymbol{A}^T t}\mathrm{d}t\boldsymbol{A}^T,$$

which combined with (2.38) directly results in (2.39) since $\lim_{t\to\infty} e^{\boldsymbol{A}t} = \boldsymbol{0}$ if $\boldsymbol{A}$ is asymptotically stable.

Remark 2.6 (A Bi-Proper System Leads to Infinite $\mathcal{H}_2$ Norm). *The $\mathcal{H}_2$ norm is defined only for strictly proper transfer function matrices in Defintion 2.7. Clearly, if $\hat{\boldsymbol{T}}(s)$ is bi-proper, i.e., $\boldsymbol{D} \neq \boldsymbol{0}_{n_2\times n_1}$, then $\|\hat{\boldsymbol{T}}\|_{\mathcal{H}_2}^2 = \infty$ since there must $\exists\, i \in [n_2]$ and $j \in [n_1]$ such that $\lim_{\dot{\omega}\to\infty} \hat{T}_{ij}(\boldsymbol{j}\dot{\omega}) = D_{ij} \neq 0$.*

2.3.2 Frequency Response and Storage Economic Metrics

After a brief review of the basic concepts of signal and system norms, we are ready to apply them to quantifying the performance of the power system shown in Figure 2.8 under different frequency control laws. Notably, for the design of frequency control based on inverter-interfaced energy storage, not only control performance but also economic factors matter. Therefore, the performance metrics that are of our interest for comparing different control laws are twofold: frequency response metrics and storage economic metrics.

Frequency Response Metrics

Before introducing the frequency response metrics that will be used in this thesis, we need to define some useful notions. Since different buses exhibit different frequencies in a n-bus system, a classical option to power system

engineers is to consider the inertia-weighted average of bus frequency deviations (in p.u.), also known as the *center of inertia (COI) frequency deviation* [28], i.e.,

$$\bar{\omega} := \frac{\sum_{i=1}^{n} m_i \omega_i}{\sum_{i=1}^{n} m_i}, \tag{2.41}$$

as the global representative system frequency. Then, the oscillations of all individual bus frequencies around the COI frequency can be characterized by $\tilde{\boldsymbol{\omega}} := (\tilde{\omega}_i, i \in [n]) := \boldsymbol{\omega} - \bar{\omega}\mathbf{1}_n \in \mathbb{R}^n$ (in p.u.). With these two notions defined, we now introduce the factors that are relevant to frequency security.

- *Synchronous frequency* measures the steady-state grid frequency deviation from its nominal value when all individual buses synchronize after a sudden power imbalance $\boldsymbol{p}_{\text{in}}$. In other words, if $\boldsymbol{\omega}(\infty) = \omega_{\text{syn}}\mathbf{1}_n$, then ω_{syn} is called the synchronous frequency. Clearly, if the synchronous frequency exists, then it is exactly the steady-state COI frequency deviation since $\bar{\omega}(\infty) = \left(\sum_{i=1}^{n} m_i \omega_{\text{syn}}\right) / \left(\sum_{i=1}^{n} m_i\right) = \omega_{\text{syn}}$. In the absence of a secondary control layer, e.g., automatic generation control [13], the system can synchronize with a nontrivial frequency deviation, i.e., $\omega_{\text{syn}} \neq 0$. For example, the maximum allowed quasi-steady-state frequency deviation for the European and Great Britain power systems is $\pm 200\,\text{mHz}$ (± 0.004 p.u. on a 50 Hz base) [45, 53].

- *Nadir* measures the maximum grid frequency deviation during a transient response to a sudden power imbalance $\boldsymbol{p}_{\text{in}}$. It can be quantified by the $\mathcal{L}_\infty$ norm of the COI frequency deviation $\bar{\omega}$, i.e.,

$$\|\bar{\omega}\|_{\mathcal{L}_\infty} := \max_{t \geq 0} |\bar{\omega}(t)| . \tag{2.42}$$

This quantity matters in that deeper Nadir increases the risk of under-frequency load shedding and cascading outrages. For example, the maximum allowed Nadir is 800 mHz (0.016 p.u. on a 50 Hz base) for the European power system [46] and 500 mHz (0.01 p.u. on a 50 Hz base) for the Great Britain power system [44, 45]. Thus, one of our targets is to find conditions that make Nadir equal to the steady-state COI frequency deviation. In other words, we want to remove the overshoot in the transient COI frequency, which is what we mean by *Nadir elimination* hereafter. The no overshoot property resulting from Nadir elimination allows the COI frequency to monotonically move towards its new steady-state without experiencing Nadir, which largely improves frequency security.

- *RoCoF* measures the maximum rate of change of frequency during a transient response to a sudden power imbalance $\boldsymbol{p}_{\text{in}}$, i.e.,

$$\|\dot{\tilde{\omega}}\|_{\mathcal{L}_\infty} := \max_{t\geq 0} |\dot{\tilde{\omega}}(t)|\,, \tag{2.43}$$

  which usually occurs at the initial time instant for a first- or second-order COI frequency response. A high RoCoF may cause the frequency to fall quickly below the under-frequency load shedding threshold before the frequency control actions kick in [54]. For example, the highest RoCoF allowed in the European power system is $0.5\,\text{Hz}\,\text{s}^{-1}$ ($0.01\,\text{p.u.}\,\text{s}^{-1}$ on a 50 Hz base).

- *Synchronization cost* measures the total oscillations of all individual bus frequency responses around the COI frequency response following a sudden power imbalance $\boldsymbol{p}_{\text{in}}$. It can be quantified by the squared $\mathcal{L}_2$ norm of $\tilde{\omega}$, i.e.,

$$\|\tilde{\boldsymbol{\omega}}\|_{\mathcal{L}_2}^2 := \sum_{i=1}^{n} \int_0^\infty |\tilde{\omega}_i(t)|^2 \mathrm{d}t = \int_0^\infty \tilde{\boldsymbol{\omega}}(t)^T \tilde{\boldsymbol{\omega}}(t) \mathrm{d}t \,. \tag{2.44}$$

- *Frequency variance* measures how the relative intensity of stochastic power fluctuations $\boldsymbol{n}_\mathrm{p}$ and frequency measurement noise $\boldsymbol{n}_\omega$ affect the frequency deviations, where the signals $\boldsymbol{n}_\mathrm{p}$ and $\boldsymbol{n}_\omega$ are assumed to be uncorrelated white noise of unit intensity such that

$$\mathbb{E}\left[\boldsymbol{n}_\mathrm{p}(t)\boldsymbol{n}_\mathrm{p}(\tau)^T\right] = \delta(t-\tau)\boldsymbol{I}_n \,,$$

$$\mathbb{E}\left[\boldsymbol{n}_\omega(t)\boldsymbol{n}_\omega(\tau)^T\right] = \delta(t-\tau)\boldsymbol{I}_n \,,$$

$$\mathbb{E}\left[\boldsymbol{n}_\mathrm{p}(t)\boldsymbol{n}_\omega(\tau)^T\right] = \boldsymbol{0}_{n\times n} \,.$$

  This can be quantified by the squared $\mathcal{H}_2$ norm of the system $\hat{\boldsymbol{T}}_{\omega\mathrm{n}}(s)$ due to its stochastic interpretation, i.e.,

$$\lim_{t\to\infty} \mathbb{E}\left[\boldsymbol{\omega}(t)^T\boldsymbol{\omega}(t)\right] = \|\hat{\boldsymbol{T}}_{\omega\mathrm{n}}\|_{\mathcal{H}_2}^2 := \frac{1}{2\pi}\int_{-\infty}^{\infty} \mathrm{tr}\left(\hat{\boldsymbol{T}}_{\omega\mathrm{n}}(\boldsymbol{j}\dot{\omega})^* \hat{\boldsymbol{T}}_{\omega\mathrm{n}}(\boldsymbol{j}\dot{\omega})\right) \mathrm{d}\dot{\omega} \,. \tag{2.45}$$

Storage Economic Metrics

The factors that affect the cost of inverter-interfaced energy storage are:

- *Steady-state effort share* measures the fraction of the power imbalance $\boldsymbol{p}_\mathrm{in}$ addressed by inverter-interfaced energy storage. It is calculated as the absolute value of the ratio between the total steady-state inverter power output variation and the total power imbalance, i.e.,

$$\eta_\mathrm{es} := \left| \frac{\sum_{i=1}^n \hat{c}_i(0)\omega_i(\infty)}{\sum_{i=1}^n p_{\mathrm{in},i}(0^+)} \right| \,, \tag{2.46}$$

where $\hat{c}_i(0)$ is the dc gain of the ith inverter. A higher steady-state effort share indicates that a larger amount of steady-state power output is required from inverter-interfaced energy storage in the process of handling certain power imbalance. Since this necessary headroom is achieved by additional storage capacity [46], a lower steady-state effort can be associated with lower operational costs and it is therefore desired.

Chapter 3

Foundations of Performance Analysis for Proportionally Heterogeneous Power Systems

This chapter turns attention towards proportionally heterogeneous power systems, a reasonable first-cut approximation to generally heterogeneous power systems, where a modal decomposition can be done to extremely ease the performance analysis. In Section 3.1, after an introduction to our mild proportionality assumption, we perform a modal decomposition such that the power system model built in Chapter 2 is diagonalized, which results in a meaningful step response decomposition interpretation of the main mode and the remaining modes. In Section 3.2, we show that it is possible to compute all the performance metrics introduced in Chapter 2 analytically as functions of the system parameters for proportionally heterogeneous power systems, which provides a foundation for further performance comparisons among different frequency control laws based on inverter-interfaced energy storage in Chapter 4.

3.1 Modal Decomposition for Proportionally Heterogeneous Systems

It is in general tough to analyze the performance of the system $\hat{\boldsymbol{T}}_{\text{sys}}(s)$ shown in Figure 2.8 for heterogeneous parameters. Nevertheless, provided that parameters of generators and inverters scale according to their power ratings, we can vastly simplify the analysis by performing a modal decomposition on the system $\hat{\boldsymbol{T}}_{\text{sys}}(s)$. Such a proportionally heterogeneous power system assumption is aligned with our intuition that "heavier" equipment has a greater impact on the system performance.

Therefore, from now on, we restrict our attention to the proportionally heterogeneous power system as described in the following assumption, which is a generalization of [28, 55]. This assumption ensures that the closed-loop transfer function matrix of the system $\hat{\boldsymbol{T}}_{\text{sys}}(s)$ is diagonalizable, which makes further performance analysis tractable.

Assumption 3.1 (Proportionality). *There exists a proportionality matrix* $\boldsymbol{R} := \text{diag}\,(r_i, i \in [n]) \in \mathbb{R}^{n\times n}$ *with* $r_i > 0$, $\forall i \in [n]$, *such that*

$$\hat{\boldsymbol{G}}(s) = \hat{g}_{\text{o}}(s)\boldsymbol{R}^{-1} \qquad \text{and} \qquad \hat{\boldsymbol{C}}(s) = \hat{c}_{\text{o}}(s)\boldsymbol{R}\,,$$

where $\hat{g}_{\text{o}}(s)$ *and* $\hat{c}_{\text{o}}(s)$ *are called the representative generator and the representative inverter, respectively.*

Remark 3.1 (Proportionality Parameters). *The parameters* r_i*'s could be individual generator ratings. This choice is rather arbitrary for our analysis, provided that Assumption 3.1 is satisfied. Other alternatives could include* $r_i = m_i/m_{\text{o}}$ *where*

m_o is, for example, either the average or maximum or even 1 s generator inertia. The practical relevance of Assumption 3.1 is justified, for example, by the empirical values reported in [56], which show that, at least in regard to order of magnitude, Assumption 3.1 is a reasonable first-cut approximation to heterogeneity.

Under Assumption 3.1, the representative generator of (2.36) and (2.37) are given by

$$\hat{g}_o(s) = \frac{1}{m_o s + \alpha_{l,o}} \tag{3.1}$$

and

$$\hat{g}_o(s) = \frac{\tau_{t,o} s + 1}{m_o \tau_{t,o} s^2 + (m_o + \alpha_{l,o}\tau_{t,o})\, s + \alpha_{l,o} + \alpha_{t,o}}\,, \tag{3.2}$$

respectively, with $m_i = r_i m_o$, $\alpha_{l,i} = r_i \alpha_{l,o}$, $\alpha_{t,i} = r_i \alpha_{t,o}$, and $\tau_{t,i} = \tau_{t,o}$, $\forall i \in [n]$, while the representative inverter depends on the specific control law that will be used.[1]

3.1.1 Diagonalization

Using Assumption 3.1, we can derive a diagonalized version of (2.35) for the n-bus system shown in Figure 2.8. First, we rewrite

$$\hat{\boldsymbol{G}}(s) = \boldsymbol{R}^{-\frac{1}{2}} \left[\hat{g}_o(s) \boldsymbol{I}_n\right] \boldsymbol{R}^{-\frac{1}{2}} \qquad \text{and} \qquad \hat{\boldsymbol{C}}(s) = \boldsymbol{R}^{\frac{1}{2}} \left[\hat{c}_o(s) \boldsymbol{I}_n\right] \boldsymbol{R}^{\frac{1}{2}}$$

as shown in Figure 3.1(a). Then, after a loop transformation, we obtain Figure 3.1(b). Here, we define the scaled Laplacian matrix

$$\boldsymbol{L}_R := \boldsymbol{R}^{-\frac{1}{2}} \boldsymbol{L}_B' \boldsymbol{R}^{-\frac{1}{2}} \tag{3.3}$$

[1] We use variables with subscript o to denote parameters of the representative generator and inverter.

by grouping the terms in the upper blocks of Figure 3.1(b). Recall from Section 2.2.2 that $\boldsymbol{L}'_{\mathrm{B}}$ is real orthogonally diagonalizable with eigenvalues satisfying $0 = \lambda_1(\boldsymbol{L}'_{\mathrm{B}}) < \lambda_2(\boldsymbol{L}'_{\mathrm{B}}) \leq \ldots \leq \lambda_n(\boldsymbol{L}'_{\mathrm{B}})$.[2] We now show that $\boldsymbol{L}_{\mathrm{R}}$ shares similar properties.

Lemma 3.1 (Decomposition of the Scaled Laplacian Matrix). *$\exists$ an orthogonal matrix $\boldsymbol{U} \in \mathbb{R}^{n\times n}$ with $\boldsymbol{U}^T\boldsymbol{U} = \boldsymbol{U}\boldsymbol{U}^T = \boldsymbol{I}_n$ such that*

$$\boldsymbol{L}_{\mathrm{R}} = \boldsymbol{U}\boldsymbol{\Lambda}\boldsymbol{U}^T \,, \tag{3.4}$$

where $\boldsymbol{\Lambda} := \mathrm{diag}\,(\lambda_k, k \in [n]) \in \mathbb{R}^{n\times n}$ with λ_k being the kth eigenvalue of $\boldsymbol{L}_{\mathrm{R}}$ ordered non-decreasingly $(0 = \lambda_1 < \lambda_2 \leq \ldots \leq \lambda_n)$ and

$$\boldsymbol{U} := \begin{bmatrix} \boldsymbol{u}_1 := (\sum_{i=1}^n r_i)^{-\frac{1}{2}} \boldsymbol{R}^{\frac{1}{2}} \boldsymbol{1}_n & \boldsymbol{U}_\perp := \begin{bmatrix} \boldsymbol{u}_2 & \ldots & \boldsymbol{u}_n \end{bmatrix} \end{bmatrix} \tag{3.5}$$

composed by the eigenvector $\boldsymbol{u}_k = (u_{k,i}, i \in [n]) \in \mathbb{R}^n$ associated with λ_k.[3]

Proof. First, $\boldsymbol{L}_{\mathrm{R}}$ is symmetric since we know from Section 2.2.2 that $\boldsymbol{L}'_{\mathrm{B}}$ is symmetric, which means that $\boldsymbol{L}_{\mathrm{R}}$ is real orthogonally diagonalizable as in (3.4). Thus, the key is to show that the eigenvalues of $\boldsymbol{L}_{\mathrm{R}}$ satisfy $0 = \lambda_1 < \lambda_2 \leq \ldots \leq \lambda_n$ and 0 is an eigenvalue of $\boldsymbol{L}_{\mathrm{R}}$ associated with eigenvector $(\sum_{i=1}^n r_i)^{-\frac{1}{2}} \boldsymbol{R}^{\frac{1}{2}} \boldsymbol{1}_n$. Recall from Section 2.2.2 that

$$L_{\mathrm{B},ij} := \begin{cases} -W_{ij} & \text{if } i \neq j \\ \sum\limits_{j'=1, j' \neq i}^{n} W_{ij'} & \text{if } i = j \end{cases} \,, \qquad \forall i, j \in [n] \,, \tag{3.6}$$

[2] Throughout this thesis, for a matrix $\boldsymbol{E} \in \mathbb{C}^{n\times n}$ with only real eigenvalues, we always order its eigenvalues non-decreasingly, i.e., $\lambda_1(\boldsymbol{E}) \leq \lambda_2(\boldsymbol{E}) \leq \ldots \leq \lambda_n(\boldsymbol{E})$.

[3] We use k and l to index dynamic modes but i and j to index bus numbers.

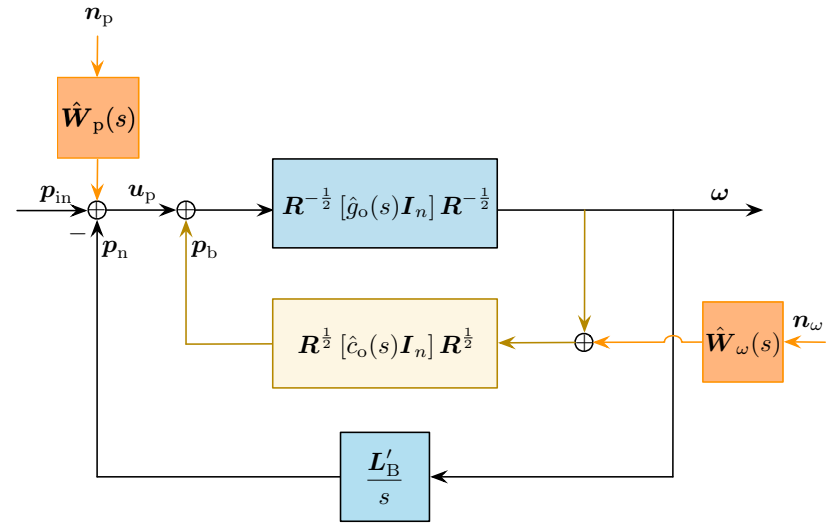

(a)

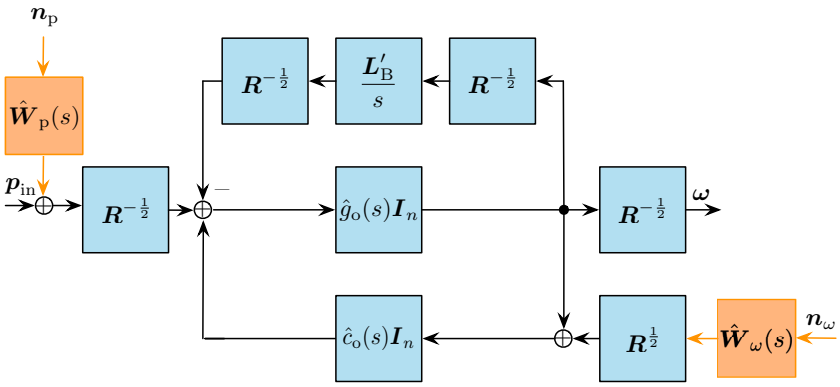

(b)

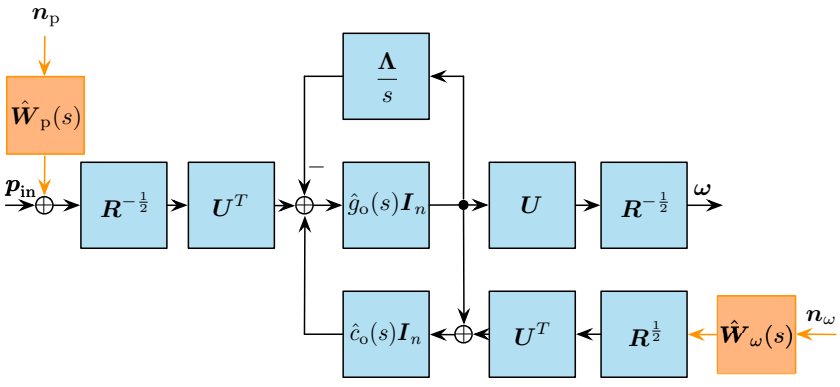

(c)

Figure 3.1: Equivalent block diagrams of the multi-bus system under proportionality assumption

with

$$W_{ij} = W_{ji} = \begin{cases} |V_i||V_j|B_{ij}\cos(\Theta_{\star,i} - \Theta_{\star,j}) > 0 & \text{if} \{i,j\} \in \mathcal{E} \\ \\ 0 & \text{if } \{i,j\} \notin \mathcal{E} \end{cases}, \quad \forall i,j \in [n] \ .$$

Thus, combining (3.3) and (3.6), we can write $\boldsymbol{L}_{\mathrm{R}}$ explicitly as

$$L_{\mathrm{R},ij} := \begin{cases} -\dfrac{W_{ij}}{\sqrt{r_i r_j}} & \text{if } i \neq j \\ \\ \displaystyle\sum_{j'=1, j' \neq i}^{n} \dfrac{W_{ij'}}{r_i} & \text{if } i = j \end{cases}, \qquad \forall i,j \in [n] \ . \tag{3.7}$$

In order to show that all eigenvalues of $\boldsymbol{L}_{\mathrm{R}}$ are nonnegative, we show that $\boldsymbol{L}_{\mathrm{R}}$ is positive semidefinite. Note that, $\forall \boldsymbol{y} := (y_i, i \in [n]) \in \mathbb{R}^n$,

$$\begin{aligned} \boldsymbol{y}^T \boldsymbol{L}_{\mathrm{R}} \boldsymbol{y} &= \sum_{i=1}^{n} y_i \left(\sum_{j=1}^{n} L_{\mathrm{R},ij} y_j \right) = \sum_{i=1}^{n} y_i \left(L_{\mathrm{R},ii} y_i + \sum_{j=1, j\neq i}^{n} L_{\mathrm{R},ij} y_j \right) \\ &= \sum_{i=1}^{n} y_i \left(\sum_{j=1, j\neq i}^{n} \frac{W_{ij}}{r_i} y_i - \sum_{j=1, j\neq i}^{n} \frac{W_{ij}}{\sqrt{r_i r_j}} y_j \right) \\ &= \sum_{i=1}^{n} \sum_{j=1, j\neq i}^{n} \frac{W_{ij}}{\sqrt{r_i}} \left(\frac{y_i^2}{\sqrt{r_i}} - \frac{y_i y_j}{\sqrt{r_j}} \right) = \sum_{i=1}^{n} \sum_{j=1}^{n} \frac{W_{ij}}{\sqrt{r_i}} \left(\frac{y_i^2}{\sqrt{r_i}} - \frac{y_i y_j}{\sqrt{r_j}} \right) \\ &= \sum_{i=1}^{n} \sum_{j=1}^{n} \frac{W_{ij}}{\sqrt{r_i}} \frac{y_i^2}{2\sqrt{r_i}} + \sum_{i=1}^{n} \sum_{j=1}^{n} \frac{W_{ij}}{\sqrt{r_i}} \frac{y_i^2}{2\sqrt{r_i}} - \sum_{i=1}^{n} \sum_{j=1}^{n} \frac{W_{ij}}{\sqrt{r_i}} \frac{y_i y_j}{\sqrt{r_j}} \\ &= \sum_{i=1}^{n} \sum_{j=1}^{n} \frac{W_{ij}}{\sqrt{r_i}} \frac{y_i^2}{2\sqrt{r_i}} + \sum_{i=1}^{n} \sum_{j=1}^{n} \frac{W_{ji}}{\sqrt{r_j}} \frac{y_j^2}{2\sqrt{r_j}} - \sum_{i=1}^{n} \sum_{j=1}^{n} \frac{W_{ij}}{\sqrt{r_i}} \frac{y_i y_j}{\sqrt{r_j}} \\ &= \sum_{i=1}^{n} \sum_{j=1}^{n} \frac{W_{ij}}{\sqrt{r_i}} \frac{y_i^2}{2\sqrt{r_i}} + \sum_{i=1}^{n} \sum_{j=1}^{n} \frac{W_{ij}}{\sqrt{r_j}} \frac{y_j^2}{2\sqrt{r_j}} - \sum_{i=1}^{n} \sum_{j=1}^{n} \frac{W_{ij}}{\sqrt{r_i}} \frac{y_i y_j}{\sqrt{r_j}} \end{aligned}$$

$$= \frac{1}{2}\sum_{i=1}^{n}\sum_{j=1}^{n} W_{ij}\left(\frac{y_i}{\sqrt{r_i}} - \frac{y_j}{\sqrt{r_j}}\right)^2 = \sum_{\{i,j\}\in\mathcal{E}} W_{ij}\left(\frac{y_i}{\sqrt{r_i}} - \frac{y_j}{\sqrt{r_j}}\right)^2 \geq 0\,. \quad (3.8)$$

Thus, $\boldsymbol{L}_{\mathrm{R}}$ is positive semidefinite, which means that all eigenvalues of $\boldsymbol{L}_{\mathrm{R}}$ are nonnegative. Recall from Section 2.2.2 that $\boldsymbol{L}'_{\mathrm{B}}\mathbf{1}_n = \mathbf{0}_{n\times 1}$. Thus, it is easy to see that 0 is an eigenvalue of $\boldsymbol{L}_{\mathrm{R}}$ associated with eigenvector $(\sum_{i=1}^{n} r_i)^{-\frac{1}{2}}\boldsymbol{R}^{\frac{1}{2}}\mathbf{1}_n$ since $\boldsymbol{L}_{\mathrm{R}}\boldsymbol{R}^{\frac{1}{2}}\mathbf{1}_n = \boldsymbol{R}^{-\frac{1}{2}}\boldsymbol{L}'_{\mathrm{B}}\boldsymbol{R}^{-\frac{1}{2}}\boldsymbol{R}^{\frac{1}{2}}\mathbf{1}_n = \boldsymbol{R}^{-\frac{1}{2}}\boldsymbol{L}'_{\mathrm{B}}\mathbf{1}_n = \boldsymbol{R}^{-\frac{1}{2}}\mathbf{0}_{n\times 1} = \mathbf{0}_{n\times 1}$, where $\boldsymbol{R}^{\frac{1}{2}}\mathbf{1}_n$ is normalized to length 1 by a factor of $(\sum_{i=1}^{n} r_i)^{-\frac{1}{2}}$. Now, we still need to show that the algebraic multiplicity of the 0 eigenvalue of $\boldsymbol{L}_{\mathrm{R}}$ is 1, which can be seen from the nullity of $\boldsymbol{L}_{\mathrm{R}}$. Assume that $\boldsymbol{y} \in \mathbb{R}^n$ is in the null space of $\boldsymbol{L}_{\mathrm{R}}$, i.e., $\boldsymbol{L}_{\mathrm{R}}\boldsymbol{y} = \mathbf{0}_{n\times 1}$. Then, $\boldsymbol{y}^T\boldsymbol{L}_{\mathrm{R}}\boldsymbol{y} = 0$. From (3.8), we know that

$$\sum_{\{i,j\}\in\mathcal{E}} W_{ij}\left(\frac{y_i}{\sqrt{r_i}} - \frac{y_j}{\sqrt{r_j}}\right)^2 = 0\,,$$

which implies that $y_i/\sqrt{r_i} = y_j/\sqrt{r_j}$, $\forall\{i,j\} \in \mathcal{E}$. Recall that the graph $(\mathcal{V},\mathcal{E})$ is assumed to be connected, which means that $y_1/\sqrt{r_1} = \ldots = y_n/\sqrt{r_n}$, i.e., $y_1 : \ldots : y_n = \sqrt{r_1} : \ldots : \sqrt{r_n}$.[4] Thus, every member of the null space is a multiple of $\boldsymbol{R}^{\frac{1}{2}}\mathbf{1}_n$, which means that the nullity is 1. This concludes the proof. □

Remark 3.2 (Algebraic Connectivity). *The proof of Lemma 3.1 verifies that the second smallest eigenvalue λ_2 of a symmetric (scaled) Laplacian matrix is positive if the associated graph is connected, which is part of the reason for calling it the algebraic connectivity [49].*

Now, applying (3.3) and (3.4) to Figure 3.1(b) and rearranging blocks of $\boldsymbol{U}$ and $\boldsymbol{U}^T$ results in Figure 3.1(c). Finally, moving the block of $\hat{c}_{\mathrm{o}}(s)\boldsymbol{I}_n$ ahead

[4]The colon is a symbol for ratio.

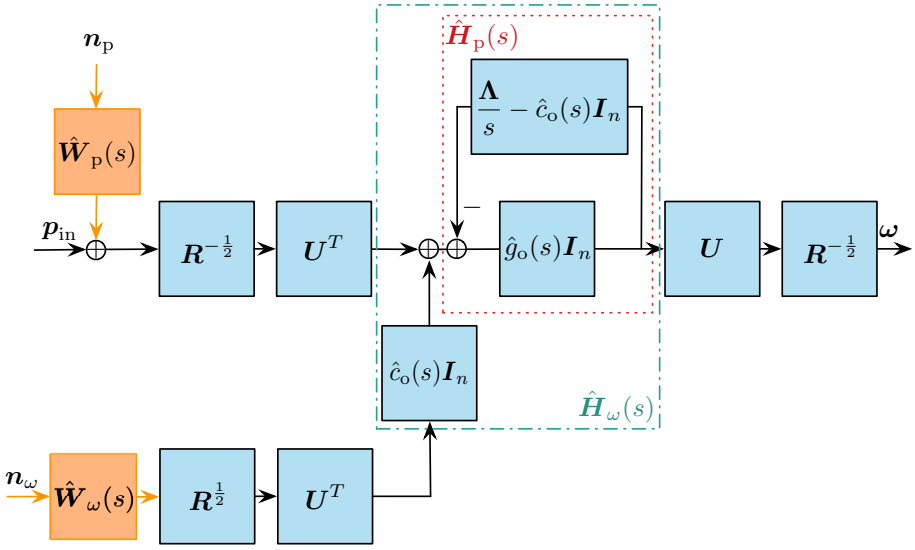

Figure 3.2: Diagonalized block diagram of the multi-bus system

of the summing junction and combining the two parallel paths produces Figure 3.2, where the boxed part is fully diagonalized.

Now, by defining the closed-loop with a forward-path $\hat{g}_{\mathrm{o}}(s)\boldsymbol{I}_n$ and a feedback-path $(\boldsymbol{\Lambda}/s - \hat{c}_{\mathrm{o}}(s)\boldsymbol{I}_n)$ as

$$\hat{\boldsymbol{H}}_{\mathrm{p}}(s) = \mathrm{diag}\left(\hat{h}_{\mathrm{p},k}(s), k \in [n]\right) , \tag{3.9}$$

where

$$\hat{h}_{\mathrm{p},k}(s) = \frac{\hat{g}_{\mathrm{o}}(s)}{1 + \hat{g}_{\mathrm{o}}(s)\left(\lambda_k/s - \hat{c}_{\mathrm{o}}(s)\right)} , \tag{3.10}$$

and $\hat{\boldsymbol{H}}_{\omega}(s) = \hat{c}_{\mathrm{o}}(s)\hat{\boldsymbol{H}}_{\mathrm{p}}(s)$, i.e.,

$$\hat{\boldsymbol{H}}_{\omega}(s) = \mathrm{diag}\left(\hat{h}_{\omega,k}(s), k \in [n]\right) ,$$

where

$$\hat{h}_{\omega,k}(s) = \hat{c}_{\mathrm{o}}(s)\hat{h}_{\mathrm{p},k}(s) , \tag{3.11}$$

the closed-loop transfer functions from $\boldsymbol{p}_{\text{in}}$, $\boldsymbol{n}_{\text{p}}$, and $\boldsymbol{n}_{\omega}$ to $\boldsymbol{\omega}$ become

$$\hat{\boldsymbol{T}}_{\omega \text{p}}(s) = \boldsymbol{R}^{-\frac{1}{2}} \boldsymbol{U} \hat{\boldsymbol{H}}_{\text{p}}(s) \boldsymbol{U}^T \boldsymbol{R}^{-\frac{1}{2}} \,, \tag{3.12a}$$

$$\hat{\boldsymbol{T}}_{\omega \text{n}_{\text{p}}}(s) = \boldsymbol{R}^{-\frac{1}{2}} \boldsymbol{U} \hat{\boldsymbol{H}}_{\text{p}}(s) \boldsymbol{U}^T \boldsymbol{R}^{-\frac{1}{2}} \hat{\boldsymbol{W}}_{\text{p}}(s) \,, \tag{3.12b}$$

$$\hat{\boldsymbol{T}}_{\omega \text{n}_{\omega}}(s) = \boldsymbol{R}^{-\frac{1}{2}} \boldsymbol{U} \hat{\boldsymbol{H}}_{\omega}(s) \boldsymbol{U}^T \boldsymbol{R}^{\frac{1}{2}} \hat{\boldsymbol{W}}_{\omega}(s) \,, \tag{3.12c}$$

respectively.[5]

As described in Section 2.3.2, the synchronous frequency, Nadir, RoCoF, synchronization cost, and steady-state effort share can all be characterized by a step response of the system $\hat{\boldsymbol{T}}_{\omega \text{p}}(s)$, while the sensitivity to stochastic power fluctuations and frequency measurement noise can be evaluated through the $\mathcal{H}_2$ norm of the system $\hat{\boldsymbol{T}}_{\omega \text{n}}(s) := \begin{bmatrix} \hat{\boldsymbol{T}}_{\omega \text{n}_{\text{p}}}(s) & \hat{\boldsymbol{T}}_{\omega \text{n}_{\omega}}(s) \end{bmatrix}$. Thus, there are two scenarios that are of our interest.

Assumption 3.2 (Step Input Scenario). *There is a step change on the power injection set point, i.e.,* $\boldsymbol{p}_{\text{in}} = \boldsymbol{\mu}_0 \mathbb{1}_{t \geq 0}$, $\boldsymbol{n}_{\text{p}} = \boldsymbol{0}_{n \times 1}$, *and* $\boldsymbol{n}_{\omega} = \boldsymbol{0}_{n \times 1}$, *where* $\boldsymbol{\mu}_0 \in \mathbb{R}^n$ *is a given vector direction that allows for power disturbances of different magnitudes at individual buses and* $\mathbb{1}_{t \geq 0}$ *is the unit-step function.*

Assumption 3.3 (Proportionally Weighted Noise Scenario). *The noise weighting functions are given by* $\hat{\boldsymbol{W}}_{\text{p}}(s) = \kappa_{\text{p}} \boldsymbol{R}^{\frac{1}{2}}$ *and* $\hat{\boldsymbol{W}}_{\omega}(s) = \kappa_{\omega} \boldsymbol{R}^{-\frac{1}{2}}$, *where* $\kappa_{\text{p}} > 0$ *and* $\kappa_{\omega} > 0$ *are weighting constants.*

Remark 3.3 (About the Weighting Assumption). *As a natural counterpart of*

[5] With abuse of notation, the specific generator dynamics involved in $\hat{h}_{\text{p},k}(s)$ depends on the input scenario which should be clear from the metric considered. Thus, in the rest of this thesis, there might be the cases where two input scenarios happen to share the transfer function symbol.

Assumption 3.1, we look at the case when the stochastic power fluctuations and frequency measurement noise are weighted directly and inversely proportional to the square root of the bus ratings, respectively. In the case of $\hat{\boldsymbol{W}}_{\mathrm{p}}(s)$, this is equivalent to assuming that demand fluctuation variances are proportional to the bus ratings, which is in agreement with the central limit theorem. As for $\hat{\boldsymbol{W}}_{\omega}(s)$, this is equivalent to assuming that the frequency measurement noise variances are inversely proportional to the bus ratings, which is in line with the inverse relationship between jitter variance and power consumption for an oscillator in a phase-locked loop [57].

3.1.2 Step Response Decomposition

Recall that in Section 2.3.2 there is a mention of a desire to separate individual bus frequencies into the COI frequency and oscillations around it for quantifying the frequency response performance when the system undergoes a sudden power imbalance. We now show that this separation can be done nicely for a proportionally heterogeneous system by mostly following the approach from [28].

Let Assumption 3.2 hold. Then, the step response of the system $\hat{\boldsymbol{T}}_{\omega\mathrm{p}}(s)$ in (3.12) can be described in the Laplace domain as

$$\hat{\boldsymbol{\omega}} = \hat{\boldsymbol{T}}_{\omega\mathrm{p}}(s)\hat{\boldsymbol{p}}_{\mathrm{in}} = \boldsymbol{R}^{-\frac{1}{2}}\boldsymbol{U}\hat{\boldsymbol{H}}_{\mathrm{p}}(s)\boldsymbol{U}^{T}\boldsymbol{R}^{-\frac{1}{2}}\frac{\boldsymbol{\mu}_0}{s}\,. \tag{3.13}$$

Next, we can separate the first mode from all others in (3.13) by using (3.5) and (3.9).

$$\hat{\boldsymbol{\omega}} = \boldsymbol{R}^{-\frac{1}{2}}\begin{bmatrix}(\sum_{i=1}^{n} r_i)^{-\frac{1}{2}}\boldsymbol{R}^{\frac{1}{2}}\mathbf{1}_n & \boldsymbol{U}_{\perp}\end{bmatrix}\begin{bmatrix}\hat{h}_{\mathrm{p},1}(s) & \mathbf{0}_{1\times(n-1)} \\ \mathbf{0}_{(n-1)\times 1} & \hat{\boldsymbol{H}}_{\mathrm{p}\perp}(s)\end{bmatrix}\begin{bmatrix}(\sum_{i=1}^{n} r_i)^{-\frac{1}{2}}\mathbf{1}_n^{T}\boldsymbol{R}^{\frac{1}{2}} \\ \boldsymbol{U}_{\perp}^{T}\end{bmatrix}\boldsymbol{R}^{-\frac{1}{2}}\frac{\boldsymbol{\mu}_0}{s}$$

$$= \left(\frac{\sum_{i=1}^{n} \mu_{0,i}}{\sum_{i=1}^{n} r_i} \frac{\hat{h}_{\mathrm{p},1}(s)}{s} \right) \mathbf{1}_n + \boldsymbol{R}^{-\frac{1}{2}} \boldsymbol{U}_\perp \hat{\boldsymbol{H}}_{\mathrm{p}\perp}(s) \boldsymbol{U}_\perp^T \boldsymbol{R}^{-\frac{1}{2}} \frac{\boldsymbol{\mu}_0}{s}, \tag{3.14}$$

where

$$\hat{\boldsymbol{H}}_{\mathrm{p}\perp}(s) := \mathrm{diag}\left(\hat{h}_{\mathrm{p},k}(s), k \in [n] \setminus \{1\} \right).$$

It is convenient to define

$$\hat{h}_{\mathrm{u},k}(s) := \frac{\hat{h}_{\mathrm{p},k}(s)}{s}, \ \forall k \in [n], \quad \text{and} \quad \hat{\boldsymbol{H}}_{\mathrm{u}\perp}(s) := \mathrm{diag}\left(\hat{h}_{\mathrm{u},k}(s), k \in [n] \setminus \{1\} \right),$$

with which (3.14) can be expressed as

$$\hat{\boldsymbol{\omega}} = \left(\frac{\sum_{i=1}^{n} \mu_{0,i}}{\sum_{i=1}^{n} r_i} \hat{h}_{\mathrm{u},1}(s) \right) \mathbf{1}_n + \boldsymbol{R}^{-\frac{1}{2}} \boldsymbol{U}_\perp \hat{\boldsymbol{H}}_{\mathrm{u}\perp}(s) \boldsymbol{U}_\perp^T \boldsymbol{R}^{-\frac{1}{2}} \boldsymbol{\mu}_0 . \tag{3.15}$$

Observe from (3.15) that each bus frequency deviation is partitioned into two terms, where the first term describes a tendency toward a common behavior among all buses and the second term represents the deviation of the actual dynamics from the common behavior.

To gain a better insight into the common behavior, we can use the trick that $(\sum_{i=1}^{n} r_i)^{-\frac{1}{2}} \mathbf{1}_n^T \boldsymbol{R}^{\frac{1}{2}} \boldsymbol{U}_\perp = \mathbf{0}_{1\times(n-1)}$ which is due to the inherent property of the orthogonal matrix $\boldsymbol{U}$, i.e., $\boldsymbol{U}^T\boldsymbol{U} = \boldsymbol{I}_n$. With this in mind, we can eliminate the second term in (3.15) after pre-multiplying it by $\mathbf{1}_n^T \boldsymbol{R}$. This yields

$$\mathbf{1}_n^T \boldsymbol{R} \hat{\boldsymbol{\omega}} = \left(\frac{\sum_{i=1}^{n} \mu_{0,i}}{\sum_{i=1}^{n} r_i} \hat{h}_{\mathrm{u},1}(s) \right) \mathbf{1}_n^T \boldsymbol{R} \mathbf{1}_n , \text{ i.e., } \sum_{i=1}^{n} r_i \hat{\omega}_i = \left(\frac{\sum_{i=1}^{n} \mu_{0,i}}{\sum_{i=1}^{n} r_i} \hat{h}_{\mathrm{u},1}(s) \right) \sum_{i=1}^{n} r_i ,$$

from which we can solve for the common behavior as

$$\left(\frac{\sum_{i=1}^{n} \mu_{0,i}}{\sum_{i=1}^{n} r_i} \hat{h}_{\mathrm{u},1}(s) \right) = \frac{\sum_{i=1}^{n} r_i \hat{\omega}_i}{\sum_{i=1}^{n} r_i} = \frac{\sum_{i=1}^{n} m_i \hat{\omega}_i}{\sum_{i=1}^{n} m_i} =: \hat{\bar{\omega}} , \tag{3.16}$$

where the second equality is due to $m_i = r_i m_\mathrm{o}$, $\forall i \in [n]$, and the last equality is due to the definition of the COI frequency deviation in (2.41). Clearly, the common behavior is exactly the motion of the COI, which endorses the tradition to consider the COI frequency as the global representative system frequency.

Naturally, the oscillations of all individual bus frequencies around the COI frequency correspond to the second term in (3.15) since

$$\begin{aligned}\hat{\tilde{\boldsymbol{\omega}}} :=& \hat{\boldsymbol{\omega}} - \hat{\bar{\omega}}\mathbf{1}_n \\ =& \hat{\boldsymbol{\omega}} - \left(\frac{\sum_{i=1}^n \mu_{0,i}}{\sum_{i=1}^n r_i}\hat{h}_{\mathrm{u},1}(s)\right)\mathbf{1}_n = \boldsymbol{R}^{-\frac{1}{2}}\boldsymbol{U}_\perp \hat{\boldsymbol{H}}_{\mathrm{u}\perp}(s)\boldsymbol{U}_\perp^T \boldsymbol{R}^{-\frac{1}{2}}\boldsymbol{\mu}_0\,. \end{aligned} \tag{3.17}$$

3.2 Generic Analysis of Performance Metrics

We now derive some important building blocks required for the performance analysis of the diagonalized system described in (3.12). Note that the results on the synchronous frequency in Section 3.2.1 and steady-state effort share in Section 3.2.6 do not rely on the proportionality of the power system characterized by Assumption 3.1.

3.2.1 Synchronous Frequency

The following lemma provides a general expression for the synchronous frequency ω_syn in our setting.

Lemma 3.2 (Synchronous Frequency). *Let Assumptions 2.2 and 3.2 hold. If $p_{\mathrm{b},i}$ is determined by a control law $\hat{c}_i(s)$, $\forall i \in [n]$, then the output $\boldsymbol{\omega}$ of the system $\hat{\boldsymbol{T}}_{\omega\mathrm{p}}(s)$*

synchronizes to the steady-state frequency deviation $\boldsymbol{\omega}(\infty) = \omega_{\text{syn}}\mathbf{1}_n$ *with*

$$\omega_{\text{syn}} = \frac{\sum_{i=1}^{n} \mu_{0,i}}{\sum_{i=1}^{n} \left(\alpha_{\text{l},i} + \alpha_{\text{t},i} - \hat{c}_i(0)\right)} \,. \tag{3.18}$$

Proof. Combining (2.16a), (2.30), and (2.31) through $\boldsymbol{u}_{\text{p}} = \boldsymbol{p}_{\text{in}} - \boldsymbol{p}_{\text{n}}$, we get the (partial) state-space representation of the system $\hat{\boldsymbol{T}}_{\omega\text{p}}(s)$ as

$$\dot{\boldsymbol{\theta}} = \Omega_0 \boldsymbol{\omega} \,, \tag{3.19a}$$

$$\boldsymbol{M}\dot{\boldsymbol{\omega}} = -\frac{\boldsymbol{L}'_{\text{B}}}{\Omega_0}\boldsymbol{\theta} - \boldsymbol{A}_{\text{l}}\boldsymbol{\omega} + \boldsymbol{p}_{\text{m}} + \boldsymbol{p}_{\text{b}} + \boldsymbol{p}_{\text{in}} \,. \tag{3.19b}$$

In the steady-state, (3.19) yields

$$\boldsymbol{L}'_{\text{B}}\boldsymbol{\omega}(\infty)t = -\frac{\boldsymbol{L}'_{\text{B}}}{\Omega_0}\boldsymbol{\Theta}_\star - \boldsymbol{A}_{\text{l}}\boldsymbol{\omega}(\infty) + \boldsymbol{p}_{\text{m}}(\infty) + \boldsymbol{p}_{\text{b}}(\infty) + \boldsymbol{\mu}_0 \,, \tag{3.20}$$

where $(\boldsymbol{\Theta}_\star + \Omega_0\boldsymbol{\omega}(\infty)t, \boldsymbol{\omega}(\infty), \boldsymbol{p}_{\text{m}}(\infty), \boldsymbol{p}_{\text{b}}(\infty))$ denotes the steady-state solution of (3.19). Equation (3.20) indicates that $\boldsymbol{L}'_{\text{B}}\boldsymbol{\omega}(\infty)t$ is constant. Thus, $\boldsymbol{L}'_{\text{B}}\boldsymbol{\omega}(\infty) = \mathbf{0}_{n\times 1}$. Recall from Section 2.2.2 that 0 is an eigenvalue of $\boldsymbol{L}'_{\text{B}}$ with algebraic multiplicity 1. Thus, every member of the null space of $\boldsymbol{L}'_{\text{B}}$ must be a multiple of the known eigenvector $\mathbf{1}_n$ associated with the 0 eigenvalue. It follows that, $\exists\omega_{\text{syn}}$, such that $\boldsymbol{\omega}(\infty) = \omega_{\text{syn}}\mathbf{1}_n$. Therefore, (3.20) becomes

$$\mathbf{0}_{n\times 1} = -\frac{\boldsymbol{L}'_{\text{B}}}{\Omega_0}\boldsymbol{\Theta}_\star - \boldsymbol{A}_{\text{l}}\omega_{\text{syn}}\mathbf{1}_n + \boldsymbol{p}_{\text{m}}(\infty) + \boldsymbol{p}_{\text{b}}(\infty) + \boldsymbol{\mu}_0 \,, \tag{3.21}$$

where $\boldsymbol{p}_{\text{b}}(\infty) = \left(\hat{c}_i(0)\omega_{\text{syn}}, i \in [n]\right) \in \mathbb{R}^n$ and $\boldsymbol{p}_{\text{m}}(\infty) = \left(-\alpha_{\text{t},i}\omega_{\text{syn}}, i \in [n]\right) \in \mathbb{R}^n$ for $\omega_\epsilon = 0$ by (2.16b). Pre-multiplying (3.21) by $\mathbf{1}_n^T$ and using the property in Section 2.2.2, i.e., $\mathbf{1}_n^T\boldsymbol{L}'_{\text{B}} = \mathbf{1}_n^T\boldsymbol{L}'^T_{\text{B}} = \left(\boldsymbol{L}'_{\text{B}}\mathbf{1}_n\right)^T = \mathbf{0}_{n\times 1}^T$, we get the desired result in (3.18). □

3.2.2 Nadir

A deep Nadir poses a threat to the reliable operation of a power system. Hence, one of the goals of frequency control is the reduction of Nadir. We seek to evaluate the ability of different frequency control laws to eliminate Nadir. To this end, we provide a necessary and sufficient condition for Nadir elimination in a second-order system with a zero.

Theorem 3.1 (Nadir Elimination for a Second-Order System). *Assume $K > 0$, $z > 0$, $\xi \geq 0$, $\omega_{\mathrm{n}} > 0$. The step response of a second-order system with a transfer function given by*

$$\hat{h}(s) = \frac{K(s+z)}{s^2 + 2\xi\omega_{\mathrm{n}} s + \omega_{\mathrm{n}}^2}$$

has no Nadir if and only if

$$1 \leq \xi \leq \frac{z}{\omega_{\mathrm{n}}} \qquad or \qquad \begin{cases} \xi > \dfrac{z}{\omega_{\mathrm{n}}} \\ \xi \geq \dfrac{1}{2}\left(\dfrac{z}{\omega_{\mathrm{n}}} + \dfrac{\omega_{\mathrm{n}}}{z}\right) \end{cases} . \tag{3.22}$$

Proof. Basically, Nadir must occur at some nonnegative finite time instant t_{nadir}, such that $\dot{y}_{\mathrm{u}}(t_{\mathrm{nadir}}) = 0$ and $y_{\mathrm{u}}(t_{\mathrm{nadir}})$ is a maximum, where $y_{\mathrm{u}}(t)$ denotes the unit-step response of $\hat{h}(s)$, i.e., $\hat{y}_{\mathrm{u}}(s) := \hat{h}(s)/s$. We consider three cases based on the value of the damping ratio ξ separately:

- Under damped case ($0 \leq \xi < 1$): The output is

$$\hat{y}_{\mathrm{u}}(s) = \frac{Kz}{\omega_{\mathrm{n}}^2}\left[\frac{1}{s} - \frac{s + \xi\omega_{\mathrm{n}}}{(s+\xi\omega_{\mathrm{n}})^2 + \omega_{\mathrm{d}}^2} - \frac{\xi\omega_{\mathrm{n}} - \omega_{\mathrm{n}}^2/z}{(s+\xi\omega_{\mathrm{n}})^2 + \omega_{\mathrm{d}}^2}\right]$$

with $\omega_{\mathrm{d}} := \omega_{\mathrm{n}}\sqrt{1-\xi^2}$, which gives the time domain response

$$y_{\mathrm{u}}(t) = \frac{Kz}{\omega_{\mathrm{n}}^2}\left[1 - e^{-\xi\omega_{\mathrm{n}}t}\left(\cos(\omega_{\mathrm{d}}t) + \frac{\xi\omega_{\mathrm{n}} - \omega_{\mathrm{n}}^2/z}{\omega_{\mathrm{d}}}\sin(\omega_{\mathrm{d}}t)\right)\right]$$

$$= \frac{Kz}{\omega_{\mathrm{n}}^2}\left(1 - e^{-\xi\omega_{\mathrm{n}}t}\frac{\sqrt{\omega_{\mathrm{d}}^2 + \left(\xi\omega_{\mathrm{n}} - \omega_{\mathrm{n}}^2/z\right)^2}}{\omega_{\mathrm{d}}}\cos(\omega_{\mathrm{d}}t - \phi)\right)$$

with

$$\phi = \arctan\left(\frac{\xi\omega_{\mathrm{n}} - \omega_{\mathrm{n}}^2/z}{\omega_{\mathrm{d}}}\right) \in \left(-\frac{\pi}{2}, \frac{\pi}{2}\right).$$

Clearly, the above response must have oscillations. Therefore, for the case $0 \leq \xi < 1$, Nadir always exists.

- Critically damped case ($\xi = 1$): The output is

$$\hat{y}_{\mathrm{u}}(s) = \frac{Kz}{\omega_{\mathrm{n}}^2}\left[\frac{1}{s} - \frac{1}{s+\omega_{\mathrm{n}}} - \frac{\omega_{\mathrm{n}} - \omega_{\mathrm{n}}^2/z}{(s+\omega_{\mathrm{n}})^2}\right],$$

which gives the time domain response

$$y_{\mathrm{u}}(t) = \frac{Kz}{\omega_{\mathrm{n}}^2}\left\{1 - e^{-\omega_{\mathrm{n}}t}\left[1 + \left(\omega_{\mathrm{n}} - \frac{\omega_{\mathrm{n}}^2}{z}\right)t\right]\right\}.$$

Thus,

$$\dot{y}_{\mathrm{u}}(t) = Kze^{-\omega_{\mathrm{n}}t}\left[\left(1 - \frac{\omega_{\mathrm{n}}}{z}\right)t + \frac{1}{z}\right].$$

Clearly, $\dot{y}_{\mathrm{u}}(t_{\mathrm{nadir}}) = 0$ has a nonnegative finite solution

$$t_{\mathrm{nadir}} = \frac{1}{\omega_{\mathrm{n}} - z}$$

whenever $\omega_n/z > 1$. In addition, $\forall \rho > 0$, it holds that

$$\begin{aligned}
\dot{y}_u(t_{\text{nadir}} - \rho) &= Kze^{-\omega_n(t_{\text{nadir}}-\rho)} \left[\left(1 - \frac{\omega_n}{z}\right)(t_{\text{nadir}} - \rho) + \frac{1}{z} \right] \\
&= e^{\omega_n \rho} \dot{y}_u(t_{\text{nadir}}) - Kze^{-\omega_n(t_{\text{nadir}}-\rho)} \left(1 - \frac{\omega_n}{z}\right) \rho \\
&= \rho Kze^{-\omega_n(t_{\text{nadir}}-\rho)} \left(\frac{\omega_n}{z} - 1\right) > 0 \,, \\
\dot{y}_u(t_{\text{nadir}} + \rho) &= Kze^{-\omega_n(t_{\text{nadir}}+\rho)} \left[\left(1 - \frac{\omega_n}{z}\right)(t_{\text{nadir}} + \rho) + \frac{1}{z} \right] \\
&= e^{-\omega_n \rho} \dot{y}_u(t_{\text{nadir}}) + Kze^{-\omega_n(t_{\text{nadir}}+\rho)} \left(1 - \frac{\omega_n}{z}\right) \rho \\
&= \rho Kze^{-\omega_n(t_{\text{nadir}}+\rho)} \left(1 - \frac{\omega_n}{z}\right) < 0 \,,
\end{aligned}$$

which implies that $y_u(t_{\text{nadir}})$ is a maximum. Thus, Nadir occurs at t_{nadir}. Therefore, for the case $\xi = 1$, Nadir is eliminated if and only if $\omega_n/z \leq 1$. To put it more succinctly, we combine the two conditions into

$$1 = \xi \leq \frac{z}{\omega_n} \,. \tag{3.23}$$

- Over damped case ($\xi > 1$): The output is

$$\hat{y}_u(s) = \frac{Kz}{\omega_n^2} \left(\frac{1}{s} - \frac{\eta_1}{s + \sigma_1} - \frac{\eta_2}{s + \sigma_2} \right)$$

with

$$\sigma_{1,2} = \omega_n \left(\xi \pm \sqrt{\xi^2 - 1} \right) \qquad \text{and} \qquad \eta_{1,2} = \frac{1}{2} \mp \frac{\xi - \omega_n/z}{2\sqrt{\xi^2 - 1}} \,,$$

which gives the time domain response

$$y_{\mathrm{u}}(t) = \frac{Kz}{\omega_{\mathrm{n}}^2}\left(1 - \eta_1 e^{-\sigma_1 t} - \eta_2 e^{-\sigma_2 t}\right) \ .$$

Thus,

$$\dot{y}_{\mathrm{u}}(t) = \frac{Kz}{\omega_{\mathrm{n}}^2}\left(\sigma_1\eta_1 e^{-\sigma_1 t} + \sigma_2\eta_2 e^{-\sigma_2 t}\right) \ .$$

Clearly, $\dot{y}_{\mathrm{u}}(t_{\mathrm{nadir}}) = 0$ yields $\sigma_1\eta_1 e^{-\sigma_1 t_{\mathrm{nadir}}} = -\sigma_2\eta_2 e^{-\sigma_2 t_{\mathrm{nadir}}}$, which has a nonnegative finite solution

$$t_{\mathrm{nadir}} = \frac{1}{2\omega_{\mathrm{n}}\sqrt{\xi^2-1}} \ln \frac{z - \omega_{\mathrm{n}}\left(\xi + \sqrt{\xi^2-1}\right)}{z - \omega_{\mathrm{n}}\left(\xi - \sqrt{\xi^2-1}\right)}$$

whenever $z - \omega_{\mathrm{n}}\left(\xi - \sqrt{\xi^2-1}\right) < 0$. In addition, $\forall \rho > 0$, it holds that

$$\begin{aligned}
\dot{y}_{\mathrm{u}}(t_{\mathrm{nadir}} - \rho) &= \frac{Kz}{\omega_{\mathrm{n}}^2}\left[\sigma_1\eta_1 e^{-\sigma_1(t_{\mathrm{nadir}}-\rho)} + \sigma_2\eta_2 e^{-\sigma_2(t_{\mathrm{nadir}}-\rho)}\right] \\
&> e^{\sigma_1\rho}\frac{Kz}{\omega_{\mathrm{n}}^2}\left(\sigma_1\eta_1 e^{-\sigma_1 t_{\mathrm{nadir}}} + \sigma_2\eta_2 e^{-\sigma_2 t_{\mathrm{nadir}}}\right) \\
&= e^{\sigma_1\rho}\dot{y}_{\mathrm{u}}(t_{\mathrm{nadir}}) = 0 \ , \\
\dot{y}_{\mathrm{u}}(t_{\mathrm{nadir}} + \rho) &= \frac{Kz}{\omega_{\mathrm{n}}^2}\left[\sigma_1\eta_1 e^{-\sigma_1(t_{\mathrm{nadir}}+\rho)} + \sigma_2\eta_2 e^{-\sigma_2(t_{\mathrm{nadir}}+\rho)}\right] \\
&< e^{-\sigma_1\rho}\frac{Kz}{\omega_{\mathrm{n}}^2}\left(\sigma_1\eta_1 e^{-\sigma_1 t_{\mathrm{nadir}}} + \sigma_2\eta_2 e^{-\sigma_2 t_{\mathrm{nadir}}}\right) \\
&= e^{-\sigma_1\rho}\dot{y}_{\mathrm{u}}(t_{\mathrm{nadir}}) = 0 \ ,
\end{aligned}$$

since $\sigma_1 > \sigma_2 > 0$ and one can show that $\sigma_2\eta_2 < 0$ under the condition $z - \omega_{\mathrm{n}}\left(\xi - \sqrt{\xi^2-1}\right) < 0$. This implies that $y_{\mathrm{u}}(t_{\mathrm{nadir}})$ is a maximum. Thus,

Nadir occurs at t_{nadir}. Therefore, for the case $\xi > 1$, Nadir is eliminated if and only if $z - \omega_{\text{n}} \left(\xi - \sqrt{\xi^2 - 1} \right) \geq 0$, i.e., $\sqrt{\xi^2 - 1} \geq \xi - z/\omega_{\text{n}}$, which holds if and only if

$$\xi \leq \frac{z}{\omega_{\text{n}}} \qquad \text{or} \qquad \begin{cases} \xi > \dfrac{z}{\omega_{\text{n}}} \\ \xi \geq \dfrac{1}{2} \left(\dfrac{z}{\omega_{\text{n}}} + \dfrac{\omega_{\text{n}}}{z} \right) \end{cases} .$$

Thus, we get the conditions

$$1 < \xi \leq \frac{z}{\omega_{\text{n}}} \quad \text{or} \quad \begin{cases} \xi > 1 \\ \xi > \dfrac{z}{\omega_{\text{n}}} \\ \xi \geq \dfrac{1}{2} \left(\dfrac{z}{\omega_{\text{n}}} + \dfrac{\omega_{\text{n}}}{z} \right) \end{cases} . \tag{3.24}$$

Note that, $\forall a, b \geq 0$, $(a + b)/2 \geq \sqrt{ab}$ with equality only when $a = b$. Thus, if $z \neq \omega_{\text{n}}$, then the third inequality in the brace ensures that $\xi > 1$. Moreover, if $z = \omega_{\text{n}}$, then the second inequality in the brace becomes $\xi > 1$. Therefore, we can remove $\xi > 1$ from the brace since the last two inequalities jointly imply this.

Finally, we can combine (3.23) and (3.24) to yield (3.22). □

3.2.3 RoCoF

Many technical reports claim that the theoretically highest RoCoF occurs at the moment just after a sudden power imbalance occurs [58]. However, to the best of our knowledge, there is no rigorous proofs for this up to now except the one provided for the specific second-order augmented synchronous generator model in [28]. Therefore, we fill this gap by showing that this claim is true for any asymptotically stable first-order system and any asymptotically

stable second-order system satisfying a minor condition. Yet, from our point of view, this claim is not necessarily true for higher order systems.

Theorem 3.2 (RoCoF of a First-Order System). *Assume $K > 0$ and $\sigma > 0$. Following a unit-step input at time $t = 0$, the (maximum) RoCoF of a first-order system with a transfer function given by*

$$\hat{h}(s) = \frac{K}{s + \sigma}$$

must occur exactly at time $t = 0^+$ with its value given by K.

Proof. Let $y_{\mathrm{u}}(t)$ denote the unit-step response of $\hat{h}(s)$, i.e., $\hat{y}_{\mathrm{u}}(s) := \hat{h}(s)/s$. Then we would like to show

$$\|\dot{y}_{\mathrm{u}}\|_{\mathcal{L}_\infty} := \max_{t \geq 0} |\dot{y}_{\mathrm{u}}(t)| = |\dot{y}_{\mathrm{u}}(0^+)| \,.$$

Note that the Laplace transform of $\dot{y}_{\mathrm{u}}(t)$ is given by

$$\mathscr{L}\{\dot{y}_{\mathrm{u}}(t)\} = s\hat{y}_{\mathrm{u}}(s) - y_{\mathrm{u}}(0^+) \,,$$

where, by the initial value theorem [59],

$$y_{\mathrm{u}}(0^+) = \lim_{s \to \infty} s\hat{y}_{\mathrm{u}}(s) = \lim_{s \to \infty} \hat{h}(s) = 0 \,.$$

Thus, we have

$$\mathscr{L}\{\dot{y}_{\mathrm{u}}(t)\} = s\hat{y}_{\mathrm{u}}(s) = \hat{h}(s)$$

whose inverse Laplace transform is

$$\dot{y}_{\mathrm{u}}(t) = Ke^{-\sigma t} > 0 \,.$$

Therefore, $|\dot{y}_{\mathrm{u}}(t)| = \dot{y}_{\mathrm{u}}(t)$ exponentially decreases from K to 0, which concludes the proof. □

Theorem 3.3 (RoCoF of a Second-Order System). *Assume $K > 0$, $z > 0$, $\xi \geq 0$, $\omega_{\mathrm{n}} > 0$. Following a unit-step input at time $t = 0$, the (maximum) RoCoF of a second-order system with a transfer function given by*

$$\hat{h}(s) = \frac{K(s+z)}{s^2 + 2\xi\omega_{\mathrm{n}}s + \omega_{\mathrm{n}}^2}$$

must occur exactly at time $t = 0^+$ with its value given by K if

$$2\xi\omega_{\mathrm{n}} > z\,. \tag{3.25}$$

Proof. Let $y_{\mathrm{u}}(t)$ denote the unit-step response of $\hat{h}(s)$, i.e., $\hat{y}_{\mathrm{u}}(s) := \hat{h}(s)/s$. Then we would like to show

$$\|\dot{y}_{\mathrm{u}}\|_{\mathcal{L}_\infty} := \max_{t\geq 0} |\dot{y}_{\mathrm{u}}(t)| = |\dot{y}_{\mathrm{u}}(0^+)|\,.$$

With this aim, we will first show that $|\dot{y}_{\mathrm{u}}(0^+)|$ is a local maximum and then verify that $|\dot{y}_{\mathrm{u}}(0^+)|$ is a global maximum. Note that the Laplace transform of $\dot{y}_{\mathrm{u}}(t)$ is given by

$$\mathscr{L}\{\dot{y}_{\mathrm{u}}(t)\} = s\hat{y}_{\mathrm{u}}(s) - y_{\mathrm{u}}(0^+)\,,$$

where, by the initial value theorem,

$$y_{\mathrm{u}}(0^+) = \lim_{s\to\infty} s\hat{y}_{\mathrm{u}}(s) = \lim_{s\to\infty} \hat{h}(s) = 0\,.$$

Thus, we have

$$\mathscr{L}\{\dot{y}_{\mathrm{u}}(t)\} = s\hat{y}_{\mathrm{u}}(s) = \hat{h}(s)\,.$$

By the initial value theorem, we have

$$\dot{y}_{\mathrm{u}}(0^+) = \lim_{s\to\infty} s\mathscr{L}\{\dot{y}_{\mathrm{u}}(t)\} = \lim_{s\to\infty} s\hat{h}(s) = K > 0\,.$$

Now, as usual, we consider three cases based on the value of the damping ratio ξ separately:

- Under damped case ($0 \le \xi < 1$): Define $\omega_{\mathrm{d}} := \omega_{\mathrm{n}}\sqrt{1-\xi^2}$. Then

$$\mathscr{L}\{\dot{y}_{\mathrm{u}}(t)\} = K\left[\frac{s+\xi\omega_{\mathrm{n}}}{(s+\xi\omega_{\mathrm{n}})^2+\omega_{\mathrm{d}}^2} + \frac{z-\xi\omega_{\mathrm{n}}}{(s+\xi\omega_{\mathrm{n}})^2+\omega_{\mathrm{d}}^2}\right],$$

  whose inverse Laplace transform is

$$\begin{aligned}\dot{y}_{\mathrm{u}}(t) &= Ke^{-\xi\omega_{\mathrm{n}}t}\left(\cos(\omega_{\mathrm{d}}t) + \frac{z-\xi\omega_{\mathrm{n}}}{\omega_{\mathrm{d}}}\sin(\omega_{\mathrm{d}}t)\right)\\ &= Ke^{-\xi\omega_{\mathrm{n}}t}\frac{\sqrt{\omega_{\mathrm{d}}^2+(z-\xi\omega_{\mathrm{n}})^2}}{\omega_{\mathrm{d}}}\cos(\omega_{\mathrm{d}}t-\phi_1) \qquad (3.26)\end{aligned}$$

  with

$$\phi_1 = \arctan\left(\frac{z-\xi\omega_{\mathrm{n}}}{\omega_{\mathrm{d}}}\right) \in \left(-\frac{\pi}{2},\frac{\pi}{2}\right).$$

  Taking time derivative of (3.26), we get

$$\ddot{y}_{\mathrm{u}}(t) = -Ke^{-\xi\omega_{\mathrm{n}}t}\frac{\sqrt{\omega_{\mathrm{d}}^2+(z-\xi\omega_{\mathrm{n}})^2}}{\omega_{\mathrm{d}}}(\xi\omega_{\mathrm{n}}\cos(\omega_{\mathrm{d}}t-\phi_1)+\omega_{\mathrm{d}}\sin(\omega_{\mathrm{d}}t-\phi_1))\,.$$

  Thus, we have

$$\begin{aligned}\ddot{y}_{\mathrm{u}}(0) &= -K\frac{\sqrt{\omega_{\mathrm{d}}^2+(z-\xi\omega_{\mathrm{n}})^2}}{\omega_{\mathrm{d}}}(\xi\omega_{\mathrm{n}}\cos(-\phi_1)+\omega_{\mathrm{d}}\sin(-\phi_1))\\ &= -K\frac{\sqrt{\omega_{\mathrm{d}}^2+(z-\xi\omega_{\mathrm{n}})^2}}{\omega_{\mathrm{d}}}(\xi\omega_{\mathrm{n}}\cos\phi_1-\omega_{\mathrm{d}}\sin\phi_1)\,. \qquad (3.27)\end{aligned}$$

Note that, by the way we construct ϕ_1, we have

$$\cos\phi_1 = \frac{\omega_\mathrm{d}}{\sqrt{\omega_\mathrm{d}^2 + (z - \xi\omega_\mathrm{n})^2}} \quad \text{and} \quad \sin\phi_1 = \frac{z - \xi\omega_\mathrm{n}}{\sqrt{\omega_\mathrm{d}^2 + (z - \xi\omega_\mathrm{n})^2}}\,. \tag{3.28}$$

Substituting (3.28) to (3.27) yields

$$\ddot{y}_\mathrm{u}(0) = -K\,(2\xi\omega_\mathrm{n} - z) < 0$$

if the condition (3.25) holds. Thus, at $t = 0$, $\dot{y}_\mathrm{u}(t)$ has a tendency to decrease. Therefore, $|\dot{y}_\mathrm{u}(0^+)| = \dot{y}_\mathrm{u}(0^+) = K$ is a local maximum. We next show that $|\dot{y}_\mathrm{u}(0^+)|$ is indeed a global maximum by comparing it with all other local extrema $|\dot{y}_\mathrm{u}(t^\star)|$ at any time instant $t^\star > 0$ such that $\ddot{y}_\mathrm{u}(t^\star) = 0$. Clearly, $\ddot{y}_\mathrm{u}(t^\star) = 0$ implies that

$$\xi\omega_\mathrm{n}\cos\left(\omega_\mathrm{d}t^\star - \phi_1\right) + \omega_\mathrm{d}\sin\left(\omega_\mathrm{d}t^\star - \phi_1\right) = 0\,,$$

from which we get

$$\frac{\sin\left(\omega_\mathrm{d}t^\star - \phi_1\right)}{\cos\left(\omega_\mathrm{d}t^\star - \phi_1\right)} = -\frac{\xi\omega_\mathrm{n}}{\omega_\mathrm{d}} = -\frac{\xi}{\sqrt{1-\xi^2}}\,. \tag{3.29}$$

Combining (3.29) with the identity $\sin\left(\omega_\mathrm{d}t^\star - \phi_1\right)^2 + \cos\left(\omega_\mathrm{d}t^\star - \phi_1\right)^2 = 1$, we can get

$$\left|\cos\left(\omega_\mathrm{d}t^\star - \phi_1\right)\right| = \sqrt{1-\xi^2}\,.$$

Therefore,

$$\begin{aligned}
|\dot{y}_\mathrm{u}(t^\star)| &= Ke^{-\xi\omega_\mathrm{n}t^\star}\frac{\sqrt{\omega_\mathrm{d}^2 + (z - \xi\omega_\mathrm{n})^2}}{\omega_\mathrm{d}}\left|\cos\left(\omega_\mathrm{d}t^\star - \phi_1\right)\right| \\
&= Ke^{-\xi\omega_\mathrm{n}t^\star}\frac{\sqrt{\omega_\mathrm{d}^2 + (z - \xi\omega_\mathrm{n})^2}}{\omega_\mathrm{d}}\sqrt{1-\xi^2}
\end{aligned}$$

$$= Ke^{-\xi\omega_n t^\star} \frac{\sqrt{\omega_d^2 + (z - \xi\omega_n)^2}}{\omega_n} .$$

Note that, if the condition (3.25) hold, it follows from $0 < z < 2\xi\omega_n$ that $-\xi\omega_n < z - \xi\omega_n < \xi\omega_n$, i.e., $|z - \xi\omega_n| < \xi\omega_n$, which further implies that

$$\frac{\sqrt{\omega_d^2 + (z - \xi\omega_n)^2}}{\omega_n} < \frac{\sqrt{\omega_d^2 + (\xi\omega_n)^2}}{\omega_n} = \frac{\sqrt{\omega_n^2 (1 - \xi^2) + \xi^2\omega_n^2}}{\omega_n} = \frac{\sqrt{\omega_n^2}}{\omega_n} = 1 .$$

Therefore, $\forall t^\star > 0$,

$$|\dot{y}_u(t^\star)| < Ke^{-\xi\omega_n 0} 1 = K = |\dot{y}_u(0^+)| ,$$

which indicates that $|\dot{y}_u(0^+)|$ is a global maximum.

- Critically damped case ($\xi = 1$):

$$\mathscr{L}\{\dot{y}_u(t)\} = K \left[\frac{1}{s + \omega_n} + \frac{z - \omega_n}{(s + \omega_n)^2} \right] ,$$

whose inverse Laplace transform is

$$\dot{y}_u(t) = Ke^{-\omega_n t} \left[1 + (z - \omega_n) t \right] . \tag{3.30}$$

Taking time derivative of (3.30), we get

$$\ddot{y}_u(t) = Ke^{-\omega_n t} \left[(z - 2\omega_n) - \omega_n (z - \omega_n) t \right] . \tag{3.31}$$

Thus, we have

$$\ddot{y}_u(0) = K (z - 2\omega_n) < 0$$

if the condition (3.25) holds. Thus, at $t = 0$, $\dot{y}_u(t)$ has a tendency to decrease.

Therefore, $|\dot{y}_{\mathrm{u}}(0^+)| = \dot{y}_{\mathrm{u}}(0^+) = K$ is a local maximum. We next show that $|\dot{y}_{\mathrm{u}}(0^+)|$ is indeed a global maximum by comparing it with all other local extrema $|\dot{y}_{\mathrm{u}}(t^\star)|$ at any time instant $t^\star > 0$ such that $\ddot{y}_{\mathrm{u}}(t^\star) = 0$. From (3.31), we know $\ddot{y}_{\mathrm{u}}(t^\star) = 0$ implies that

$$(z - \omega_{\mathrm{n}})\, t^\star = \frac{z - 2\omega_{\mathrm{n}}}{\omega_{\mathrm{n}}}\,.$$

Therefore,

$$|\dot{y}_{\mathrm{u}}(t^\star)| = Ke^{-\omega_{\mathrm{n}} t^\star}\left|1 + \frac{z - 2\omega_{\mathrm{n}}}{\omega_{\mathrm{n}}}\right| = Ke^{-\omega_{\mathrm{n}} t^\star}\left|\frac{z - \omega_{\mathrm{n}}}{\omega_{\mathrm{n}}}\right| = Ke^{-\omega_{\mathrm{n}} t^\star}\frac{|z - \omega_{\mathrm{n}}|}{\omega_{\mathrm{n}}}\,.$$

Note that, if the condition (3.25) hold, it follows from $0 < z < 2\omega_{\mathrm{n}}$ that $-\omega_{\mathrm{n}} < z - \omega_{\mathrm{n}} < \omega_{\mathrm{n}}$, i.e., $|z - \omega_{\mathrm{n}}| < \omega_{\mathrm{n}}$, which further implies that, $\forall t^\star > 0$,

$$|\dot{y}_{\mathrm{u}}(t^\star)| < Ke^{-\omega_{\mathrm{n}} 0}\frac{\omega_{\mathrm{n}}}{\omega_{\mathrm{n}}} = K = |\dot{y}_{\mathrm{u}}(0^+)|\,.$$

Therefore, $|\dot{y}_{\mathrm{u}}(0^+)|$ is a global maximum.

- Over damped case ($\xi > 1$):

$$\mathscr{L}\{\dot{y}_{\mathrm{u}}(t)\} = K\left(\frac{\chi_1}{s + \sigma_1} + \frac{\chi_2}{s + \sigma_2}\right)$$

with

$$\sigma_{1,2} = \omega_{\mathrm{n}}\left(\xi \pm \sqrt{\xi^2 - 1}\right) > 0 \qquad \text{and} \qquad \chi_{1,2} = \frac{1}{2} \mp \frac{z - \xi\omega_{\mathrm{n}}}{2\omega_{\mathrm{n}}\sqrt{\xi^2 - 1}}\,,$$

whose inverse Laplace transform is

$$\dot{y}_{\mathrm{u}}(t) = K\left(\chi_1 e^{-\sigma_1 t} + \chi_2 e^{-\sigma_2 t}\right)\,. \tag{3.32}$$

Taking time derivative of (3.32), we get

$$\ddot{y}_{\mathrm{u}}(t) = -K\left(\sigma_1\chi_1 e^{-\sigma_1 t} + \sigma_2\chi_2 e^{-\sigma_2 t}\right) . \tag{3.33}$$

Thus, we have

$$\ddot{y}_{\mathrm{u}}(0) = -K\left(\sigma_1\chi_1 + \sigma_2\chi_2\right) = -K\left(2\xi\omega_{\mathrm{n}} - z\right) < 0$$

if the condition (3.25) holds. Thus, at $t = 0$, $\dot{y}_{\mathrm{u}}(t)$ has a tendency to decrease. Therefore, $|\dot{y}_{\mathrm{u}}(0^+)| = \dot{y}_{\mathrm{u}}(0^+) = K$ is a local maximum. We next show that $|\dot{y}_{\mathrm{u}}(0^+)|$ is indeed a global maximum by comparing it with all other local extrema $|\dot{y}_{\mathrm{u}}(t^\star)|$ at any time instant $t^\star > 0$ such that $\ddot{y}_{\mathrm{u}}(t^\star) = 0$. From (3.33), we know $\ddot{y}_{\mathrm{u}}(t^\star) = 0$ implies that

$$\chi_1 e^{-\sigma_1 t^\star} = -\frac{\sigma_2}{\sigma_1}\chi_2 e^{-\sigma_2 t^\star} .$$

Therefore,

$$\begin{aligned}
|\dot{y}_{\mathrm{u}}(t^\star)| &= K\left|\chi_1 e^{-\sigma_1 t^\star} + \chi_2 e^{-\sigma_2 t^\star}\right| = K\left|-\frac{\sigma_2}{\sigma_1}\chi_2 e^{-\sigma_2 t^\star} + \chi_2 e^{-\sigma_2 t^\star}\right| \\
&= Ke^{-\sigma_2 t^\star}\left|\left(1 - \frac{\sigma_2}{\sigma_1}\right)\chi_2\right| = Ke^{-\sigma_2 t^\star}\left|\frac{z - \xi\omega_{\mathrm{n}} + \omega_{\mathrm{n}}\sqrt{\xi^2 - 1}}{\omega_{\mathrm{n}}\left(\xi + \sqrt{\xi^2 - 1}\right)}\right| .
\end{aligned}$$

Note that, if the condition (3.25) hold, it follows from $0 < z < 2\xi\omega_{\mathrm{n}}$ that

$$-\xi\omega_{\mathrm{n}} + \omega_{\mathrm{n}}\sqrt{\xi^2 - 1} < z - \xi\omega_{\mathrm{n}} + \omega_{\mathrm{n}}\sqrt{\xi^2 - 1} < \xi\omega_{\mathrm{n}} + \omega_{\mathrm{n}}\sqrt{\xi^2 - 1} . \tag{3.34}$$

Combining (3.34) with the fact that

$$-\xi\omega_{\mathrm{n}} - \omega_{\mathrm{n}}\sqrt{\xi^2 - 1} < -\xi\omega_{\mathrm{n}} + \omega_{\mathrm{n}}\sqrt{\xi^2 - 1} ,$$

we get

$$-\xi\omega_{\mathrm{n}}-\omega_{\mathrm{n}}\sqrt{\xi^2-1}<z-\xi\omega_{\mathrm{n}}+\omega_{\mathrm{n}}\sqrt{\xi^2-1}<\xi\omega_{\mathrm{n}}+\omega_{\mathrm{n}}\sqrt{\xi^2-1}\,,$$

which is equivalent to

$$\left|z-\xi\omega_{\mathrm{n}}+\omega_{\mathrm{n}}\sqrt{\xi^2-1}\right|<\xi\omega_{\mathrm{n}}+\omega_{\mathrm{n}}\sqrt{\xi^2-1}=\omega_{\mathrm{n}}\left(\xi+\sqrt{\xi^2-1}\right).$$

Therefore, $\forall t^\star>0$,

$$|\dot{y}_{\mathrm{u}}(t^\star)|<Ke^{-\sigma_2 0}\frac{\omega_{\mathrm{n}}\left(\xi+\sqrt{\xi^2-1}\right)}{\omega_{\mathrm{n}}\left(\xi+\sqrt{\xi^2-1}\right)}=K=|\dot{y}_{\mathrm{u}}(0^+)|\,,$$

which indicates that $|\dot{y}_{\mathrm{u}}(0^+)|$ is a global maximum.

The result follows. □

3.2.4 Synchronization Cost

The computation of the synchronization cost defined in (2.44) for a proportionally heterogeneous system in the absence of frequency control can be found in [28]. Taking this into account, we can get corresponding results for the system with any frequency control law readily.

Lemma 3.3 (Synchronization Cost). *Let Assumptions 2.2, 3.1, and 3.2 hold. Define* $\tilde{\boldsymbol{\mu}}_0:=\boldsymbol{U}_\perp^T\boldsymbol{R}^{-\frac{1}{2}}\boldsymbol{\mu}_0$ *and* $\tilde{\boldsymbol{\Gamma}}:=\boldsymbol{U}_\perp^T\boldsymbol{R}^{-1}\boldsymbol{U}_\perp$. *Then the synchronization cost of the system* $\hat{\boldsymbol{T}}_{\omega\mathrm{p}}(s)$ *is given by*

$$\|\tilde{\boldsymbol{\omega}}\|_{\mathcal{L}_2}^2=\tilde{\boldsymbol{\mu}}_0^T\left(\tilde{\boldsymbol{\Gamma}}\circ\tilde{\boldsymbol{H}}\right)\tilde{\boldsymbol{\mu}}_0\,,\tag{3.35}$$

where $\circ$ *denotes the Hadamard product and* $\tilde{\boldsymbol{H}}:=\left[\tilde{H}_{kl}\right]\in\mathbb{R}^{(n-1)\times(n-1)}$ *is the*

matrix with its klth entry given by

$$\tilde{H}_{kl} := \int_0^\infty h_{\mathrm{u},k+1}(t) h_{\mathrm{u},l+1}(t)\, \mathrm{d}t\,, \qquad \forall k,l \in [n-1]\ .$$

Proof. This is a direct extension of [28, Proposition 2]. According to the definition of the synchronization cost $\|\tilde{\boldsymbol{\omega}}\|_{\mathcal{L}_2}^2$ in (2.44), we begin with an examination of $\tilde{\boldsymbol{\omega}}(t)^T\tilde{\boldsymbol{\omega}}(t)$, which can be obtained from the time domain counterpart of (3.17) as

$$\begin{aligned}\tilde{\boldsymbol{\omega}}(t)^T\tilde{\boldsymbol{\omega}}(t) =& \boldsymbol{\mu}_0^T \boldsymbol{R}^{-\frac{1}{2}} \boldsymbol{U}_\perp \boldsymbol{H}_{\mathrm{u}\perp}(t)^T \boldsymbol{U}_\perp^T \boldsymbol{R}^{-1} \boldsymbol{U}_\perp \boldsymbol{H}_{\mathrm{u}\perp}(t) \boldsymbol{U}_\perp^T \boldsymbol{R}^{-\frac{1}{2}} \boldsymbol{\mu}_0 \\ =& \tilde{\boldsymbol{\mu}}_0^T \boldsymbol{H}_{\mathrm{u}\perp}(t)^T \tilde{\boldsymbol{\Gamma}} \boldsymbol{H}_{\mathrm{u}\perp}(t) \tilde{\boldsymbol{\mu}}_0\end{aligned}$$

with $\tilde{\boldsymbol{\mu}}_0 := \boldsymbol{U}_\perp^T \boldsymbol{R}^{-\frac{1}{2}} \boldsymbol{\mu}_0$ and $\tilde{\boldsymbol{\Gamma}} := \boldsymbol{U}_\perp^T \boldsymbol{R}^{-1} \boldsymbol{U}_\perp$. Thus,

$$\begin{aligned}\|\tilde{\boldsymbol{\omega}}\|_{\mathcal{L}_2}^2 :=& \int_0^\infty \tilde{\boldsymbol{\omega}}(t)^T \tilde{\boldsymbol{\omega}}(t) \mathrm{d}t \\ =& \int_0^\infty \tilde{\boldsymbol{\mu}}_0^T \boldsymbol{H}_{\mathrm{u}\perp}(t)^T \tilde{\boldsymbol{\Gamma}} \boldsymbol{H}_{\mathrm{u}\perp}(t) \tilde{\boldsymbol{\mu}}_0 \mathrm{d}t = \tilde{\boldsymbol{\mu}}_0^T \left(\int_0^\infty \boldsymbol{H}_{\mathrm{u}\perp}(t)^T \tilde{\boldsymbol{\Gamma}} \boldsymbol{H}_{\mathrm{u}\perp}(t) \mathrm{d}t \right) \tilde{\boldsymbol{\mu}}_0\,,\end{aligned}$$

which is just another way to express (3.35). □

Lemma 3.3 shows that the computation of the synchronization cost requires knowing the inner products $\tilde{H}_{kl}$. Yet, the general expressions of these inner products for an arbitrary combination of k and l are too tedious to be useful in analysis. Thus, we will investigate instead bounds on the synchronization cost in terms of the inner products $\tilde{H}_{kl}$ when $k = l$, which are exactly the squared $\mathcal{H}_2$ norms of the systems $\hat{h}_{\mathrm{u},k+1}(s)$.

Lemma 3.4 (Bounds for Hadamard Product). *Let $\boldsymbol{E} \in \mathbb{R}^{n\times n}$ be a symmetric*

matrix with the minimum and maximum eigenvalues given by $\lambda_{\min}(\boldsymbol{E})$ *and* $\lambda_{\max}(\boldsymbol{E})$*, respectively. Then,* $\forall\, \boldsymbol{x} := (x_k, k \in [n]) \in \mathbb{R}^n$ *and* $\boldsymbol{y} := (y_k, k \in [n]) \in \mathbb{R}^n$*,*

$$\lambda_{\min}(\boldsymbol{E}) \sum_{k=1}^{n} x_k^2 y_k^2 \leq \boldsymbol{x}^T \left(\boldsymbol{E} \circ \left(\boldsymbol{y}\boldsymbol{y}^T \right) \right) \boldsymbol{x} \leq \lambda_{\max}(\boldsymbol{E}) \sum_{k=1}^{n} x_k^2 y_k^2 \,.$$

Proof. First, note that

$$\boldsymbol{x}^T \left(\boldsymbol{E} \circ \left(\boldsymbol{y}\boldsymbol{y}^T \right) \right) \boldsymbol{x} = \operatorname{tr}\left(\boldsymbol{E}^T \left(\boldsymbol{x} \circ \boldsymbol{y} \right) \left(\boldsymbol{x} \circ \boldsymbol{y} \right)^T \right) = \left(\boldsymbol{x} \circ \boldsymbol{y} \right)^T \boldsymbol{E}^T \left(\boldsymbol{x} \circ \boldsymbol{y} \right).$$

Since $\boldsymbol{E}$ is symmetric, by Rayleigh [50],

$$\lambda_{\min}(\boldsymbol{E}) \left(\boldsymbol{x} \circ \boldsymbol{y} \right)^T \left(\boldsymbol{x} \circ \boldsymbol{y} \right) \leq \left(\boldsymbol{x} \circ \boldsymbol{y} \right)^T \boldsymbol{E}^T \left(\boldsymbol{x} \circ \boldsymbol{y} \right) \leq \lambda_{\max}(\boldsymbol{E}) \left(\boldsymbol{x} \circ \boldsymbol{y} \right)^T \left(\boldsymbol{x} \circ \boldsymbol{y} \right).$$

Observing that $\left(\boldsymbol{x} \circ \boldsymbol{y} \right)^T \left(\boldsymbol{x} \circ \boldsymbol{y} \right) = \sum_{k=1}^{n} x_k^2 y_k^2$ completes the proof. □

Lemma 3.4 implies the following bounds on the synchronization cost.

Theorem 3.4 (Bounds on Synchronization Cost). *Let Assumptions 2.2, 3.1, and 3.2 hold. Then the synchronization cost of the system* $\hat{\boldsymbol{T}}_{\omega \mathrm{p}}(s)$ *is bounded by* $\underline{\|\tilde{\boldsymbol{\omega}}\|_{\mathcal{L}_2}^2} \leq \|\tilde{\boldsymbol{\omega}}\|_{\mathcal{L}_2}^2 \leq \overline{\|\tilde{\boldsymbol{\omega}}\|_{\mathcal{L}_2}^2}$*, where*

$$\underline{\|\tilde{\boldsymbol{\omega}}\|_{\mathcal{L}_2}^2} := \frac{\sum_{k=1}^{n-1} \tilde{\mu}_{0,k}^2 \|\hat{h}_{\mathrm{u},k+1}\|_{\mathcal{H}_2}^2}{\max_{i \in [n]} (r_i)} \qquad \text{and} \qquad \overline{\|\tilde{\boldsymbol{\omega}}\|_{\mathcal{L}_2}^2} := \frac{\sum_{k=1}^{n-1} \tilde{\mu}_{0,k}^2 \|\hat{h}_{\mathrm{u},k+1}\|_{\mathcal{H}_2}^2}{\min_{i \in [n]} (r_i)} \,.$$

Proof. Let $\boldsymbol{h}_{\mathrm{u}\perp}(t) := (h_{\mathrm{u},k}(t), k \in [n] \setminus \{1\}) \in \mathbb{R}^{n-1}$. By Lemma 3.3,

$$\begin{aligned}
\|\tilde{\boldsymbol{\omega}}\|_{\mathcal{L}_2}^2 &= \tilde{\boldsymbol{\mu}}_0^T \left(\tilde{\boldsymbol{\Gamma}} \circ \tilde{\boldsymbol{H}} \right) \tilde{\boldsymbol{\mu}}_0 = \tilde{\boldsymbol{\mu}}_0^T \left(\tilde{\boldsymbol{\Gamma}} \circ \int_0^\infty \boldsymbol{h}_{\mathrm{u}\perp}(t) \boldsymbol{h}_{\mathrm{u}\perp}(t)^T \mathrm{d}t \right) \tilde{\boldsymbol{\mu}}_0 \\
&= \int_0^\infty \tilde{\boldsymbol{\mu}}_0^T \left(\tilde{\boldsymbol{\Gamma}} \circ \left(\boldsymbol{h}_{\mathrm{u}\perp}(t) \boldsymbol{h}_{\mathrm{u}\perp}(t)^T \right) \right) \tilde{\boldsymbol{\mu}}_0 \, \mathrm{d}t \\
&\geq \int_0^\infty \lambda_{\min}(\tilde{\boldsymbol{\Gamma}}) \sum_{k=1}^{n-1} \tilde{\mu}_{0,k}^2 h_{\mathrm{u},k+1}(t)^2 \, \mathrm{d}t = \lambda_{\min}(\tilde{\boldsymbol{\Gamma}}) \sum_{k=1}^{n-1} \tilde{\mu}_{0,k}^2 \|\hat{h}_{\mathrm{u},k+1}\|_{\mathcal{H}_2}^2
\end{aligned}$$

$$\geq \lambda_{\min}(\boldsymbol{R}^{-1}) \sum_{k=1}^{n-1} \tilde{\mu}_{0,k}^2 \|\hat{h}_{\mathrm{u},k+1}\|_{\mathcal{H}_2}^2 = \frac{\sum_{k=1}^{n-1} \tilde{\mu}_{0,k}^2 \|\hat{h}_{\mathrm{u},k+1}\|_{\mathcal{H}_2}^2}{\max_{i\in[n]}(r_i)},$$

which concludes the proof of the lower bound. The first inequality follows from Lemma 3.4 by setting $\boldsymbol{E} = \tilde{\boldsymbol{\Gamma}}$, $\boldsymbol{x} = \tilde{\boldsymbol{\mu}}_0$, and $\boldsymbol{y} = \boldsymbol{h}_{\mathrm{u}\perp}(t)$. The second inequality follows from the interlacing theorem [50, Theorem 4.3.17]. More precisely, $\tilde{\boldsymbol{\Gamma}}$ is a $(n-1)$th order principal submatrix of $\boldsymbol{U}^T\boldsymbol{R}^{-1}\boldsymbol{U}$ since

$$\begin{aligned}\boldsymbol{U}^T\boldsymbol{R}^{-1}\boldsymbol{U} &= \begin{bmatrix}\boldsymbol{u}_1^T \\ \boldsymbol{U}_\perp^T\end{bmatrix} \boldsymbol{R}^{-1} \begin{bmatrix}\boldsymbol{u}_1 & \boldsymbol{U}_\perp\end{bmatrix} \\ &= \begin{bmatrix}\boldsymbol{u}_1^T\boldsymbol{R}^{-1}\boldsymbol{u}_1 & \boldsymbol{u}_1^T\boldsymbol{R}^{-1}\boldsymbol{U}_\perp \\ \boldsymbol{U}_\perp^T\boldsymbol{R}^{-1}\boldsymbol{u}_1 & \boldsymbol{U}_\perp^T\boldsymbol{R}^{-1}\boldsymbol{U}_\perp\end{bmatrix} = \begin{bmatrix}\boldsymbol{u}_1^T\boldsymbol{R}^{-1}\boldsymbol{u}_1 & \boldsymbol{u}_1^T\boldsymbol{R}^{-1}\boldsymbol{U}_\perp \\ \boldsymbol{U}_\perp^T\boldsymbol{R}^{-1}\boldsymbol{u}_1 & \tilde{\boldsymbol{\Gamma}}\end{bmatrix},\end{aligned}$$

which implies that $\lambda_i(\tilde{\boldsymbol{\Gamma}}) \geq \lambda_i(\boldsymbol{U}^T\boldsymbol{R}^{-1}\boldsymbol{U})$, $\forall i \in [n-1]$, by the interlacing theorem. In addition, it is easy to see that $\boldsymbol{U}^T\boldsymbol{R}^{-1}\boldsymbol{U}$ is similar to $\boldsymbol{R}^{-1}$ since $\boldsymbol{U}^{-1} = \boldsymbol{U}^T$ by the property of orthogonal matrix, which indicates that $\lambda_i(\boldsymbol{U}^T\boldsymbol{R}^{-1}\boldsymbol{U}) = \lambda_i(\boldsymbol{R}^{-1})$, $\forall i \in [n]$. Hence, $\forall i \in [n-1]$, $\lambda_i(\tilde{\boldsymbol{\Gamma}}) \geq \lambda_i(\boldsymbol{U}^T\boldsymbol{R}^{-1}\boldsymbol{U}) = \lambda_i(\boldsymbol{R}^{-1})$, which ensures that $\lambda_{\min}(\tilde{\boldsymbol{\Gamma}}) = \lambda_1(\tilde{\boldsymbol{\Gamma}}) \geq \lambda_1(\boldsymbol{R}^{-1}) = \lambda_{\min}(\boldsymbol{R}^{-1})$. The proof of the upper bound is similar. □

Remark 3.4 (Synchronization Cost in Homogeneous Case). *In the system $\hat{\boldsymbol{T}}_{\omega\mathrm{p}}(s)$ with homogeneous parameters, i.e., $\boldsymbol{R} = r\boldsymbol{I}_n$ for some $r > 0$, the identical lower and upper bounds on the synchronization cost imply that*

$$\|\tilde{\boldsymbol{\omega}}\|_{\mathcal{L}_2}^2 = r^{-1} \sum_{k=1}^{n-1} \tilde{\mu}_{0,k}^2 \|\hat{h}_{\mathrm{u},k+1}\|_{\mathcal{H}_2}^2.$$

3.2.5 Frequency Variance

We seek to characterize the effect of the stochastic power fluctuations and frequency measurement noise on the frequency variance by quantifying the squared $\mathcal{H}_2$ norm of the system $\hat{\boldsymbol{T}}_{\omega \mathrm{n}}(s)$.

We first show that the squared $\mathcal{H}_2$ norm of the system $\hat{\boldsymbol{T}}_{\omega \mathrm{n}}(s)$ is a weighted sum of the squared $\mathcal{H}_2$ norms of each system $\hat{h}_{\mathrm{p},k}(s)$ and $\hat{h}_{\omega,k}(s)$ in the diagonalized system (3.12).

Theorem 3.5 (Frequency Variance). *Define* $\boldsymbol{\Gamma} := \boldsymbol{U}^T \boldsymbol{R}^{-1} \boldsymbol{U}$. *If Assumptions 2.2, 3.1, and 3.3 hold, then*

$$\|\hat{\boldsymbol{T}}_{\omega \mathrm{n}}\|_{\mathcal{H}_2}^2 = \sum_{k=1}^{n} \Gamma_{kk} \left(\kappa_{\mathrm{p}}^2 \|\hat{h}_{\mathrm{p},k}\|_{\mathcal{H}_2}^2 + \kappa_{\omega}^2 \|\hat{h}_{\omega,k}\|_{\mathcal{H}_2}^2 \right) .$$

Proof. It follows from (2.35) and (2.45) that

$$\begin{aligned}
&\|\hat{\boldsymbol{T}}_{\omega \mathrm{n}}\|_{\mathcal{H}_2}^2 \\
&:= \frac{1}{2\pi} \int_{-\infty}^{\infty} \mathrm{tr} \left(\hat{\boldsymbol{T}}_{\omega \mathrm{n}}(j\dot{\omega})^* \hat{\boldsymbol{T}}_{\omega \mathrm{n}}(j\dot{\omega}) \right) \mathrm{d}\dot{\omega} \\
&= \frac{1}{2\pi} \int_{-\infty}^{\infty} \mathrm{tr} \left(\begin{bmatrix} \hat{\boldsymbol{T}}_{\omega \mathrm{n}_{\mathrm{p}}}(j\dot{\omega}) & \hat{\boldsymbol{T}}_{\omega \mathrm{n}_{\omega}}(j\dot{\omega}) \end{bmatrix}^* \begin{bmatrix} \hat{\boldsymbol{T}}_{\omega \mathrm{n}_{\mathrm{p}}}(j\dot{\omega}) & \hat{\boldsymbol{T}}_{\omega \mathrm{n}_{\omega}}(j\dot{\omega}) \end{bmatrix} \right) \mathrm{d}\dot{\omega} \\
&= \frac{1}{2\pi} \int_{-\infty}^{\infty} \mathrm{tr} \left(\hat{\boldsymbol{T}}_{\omega \mathrm{n}_{\mathrm{p}}}(j\dot{\omega})^* \hat{\boldsymbol{T}}_{\omega \mathrm{n}_{\mathrm{p}}}(j\dot{\omega}) \right) \mathrm{d}\dot{\omega} + \frac{1}{2\pi} \int_{-\infty}^{\infty} \mathrm{tr} \left(\hat{\boldsymbol{T}}_{\omega \mathrm{n}_{\omega}}(j\dot{\omega})^* \hat{\boldsymbol{T}}_{\omega \mathrm{n}_{\omega}}(j\dot{\omega}) \right) \mathrm{d}\dot{\omega} \\
&=: \|\hat{\boldsymbol{T}}_{\omega \mathrm{n}_{\mathrm{p}}}\|_{\mathcal{H}_2}^2 + \|\hat{\boldsymbol{T}}_{\omega \mathrm{n}_{\omega}}\|_{\mathcal{H}_2}^2 .
\end{aligned}$$

We now compute $\|\hat{\boldsymbol{T}}_{\omega \mathrm{n}_{\mathrm{p}}}\|_{\mathcal{H}_2}^2$. Using (3.12b) and the fact that $\hat{\boldsymbol{W}}_{\mathrm{p}}(s) = \kappa_{\mathrm{p}} \boldsymbol{R}^{\frac{1}{2}}$ by

Assumption 3.3, we can get

$$\hat{\boldsymbol{T}}_{\omega \mathrm{n_p}}(s) = \kappa_{\mathrm{p}} \boldsymbol{R}^{-\frac{1}{2}} \boldsymbol{U} \hat{\boldsymbol{H}}_{\mathrm{p}}(s) \boldsymbol{U}^T .$$

Therefore,

$$\begin{aligned}
\hat{\boldsymbol{T}}_{\omega \mathrm{n_p}}(j\dot{\omega})^* \hat{\boldsymbol{T}}_{\omega \mathrm{n_p}}(j\dot{\omega}) &= \kappa_{\mathrm{p}}^2 \boldsymbol{U} \hat{\boldsymbol{H}}_{\mathrm{p}}(j\dot{\omega})^* \boldsymbol{U}^T \boldsymbol{R}^{-1} \boldsymbol{U} \hat{\boldsymbol{H}}_{\mathrm{p}}(j\dot{\omega}) \boldsymbol{U}^T \\
&= \kappa_{\mathrm{p}}^2 \boldsymbol{U} \hat{\boldsymbol{H}}_{\mathrm{p}}(j\dot{\omega})^* \boldsymbol{\Gamma} \hat{\boldsymbol{H}}_{\mathrm{p}}(j\dot{\omega}) \boldsymbol{U}^T
\end{aligned}$$

with $\boldsymbol{\Gamma} := \boldsymbol{U}^T \boldsymbol{R}^{-1} \boldsymbol{U}$. It follows that

$$\begin{aligned}
\|\hat{\boldsymbol{T}}_{\omega \mathrm{n_p}}\|_{\mathcal{H}_2}^2 &= \frac{1}{2\pi} \int_{-\infty}^{\infty} \mathrm{tr} \left(\hat{\boldsymbol{T}}_{\omega \mathrm{n_p}}(j\dot{\omega})^* \hat{\boldsymbol{T}}_{\omega \mathrm{n_p}}(j\dot{\omega}) \right) \mathrm{d}\dot{\omega} \\
&= \frac{1}{2\pi} \int_{-\infty}^{\infty} \mathrm{tr} \left(\kappa_{\mathrm{p}}^2 \boldsymbol{U} \hat{\boldsymbol{H}}_{\mathrm{p}}(j\dot{\omega})^* \boldsymbol{\Gamma} \hat{\boldsymbol{H}}_{\mathrm{p}}(j\dot{\omega}) \boldsymbol{U}^T \right) \mathrm{d}\dot{\omega} \\
&= \frac{\kappa_{\mathrm{p}}^2}{2\pi} \int_{-\infty}^{\infty} \mathrm{tr} \left(\boldsymbol{U}^T \boldsymbol{U} \hat{\boldsymbol{H}}_{\mathrm{p}}(j\dot{\omega})^* \boldsymbol{\Gamma} \hat{\boldsymbol{H}}_{\mathrm{p}}(j\dot{\omega}) \right) \mathrm{d}\dot{\omega} \\
&= \frac{\kappa_{\mathrm{p}}^2}{2\pi} \int_{-\infty}^{\infty} \mathrm{tr} \left(\hat{\boldsymbol{H}}_{\mathrm{p}}(j\dot{\omega})^* \boldsymbol{\Gamma} \hat{\boldsymbol{H}}_{\mathrm{p}}(j\dot{\omega}) \right) \mathrm{d}\dot{\omega} \\
&= \frac{\kappa_{\mathrm{p}}^2}{2\pi} \int_{-\infty}^{\infty} \sum_{k=1}^{n} \Gamma_{kk} \hat{h}_{\mathrm{p},k}(j\dot{\omega})^* \hat{h}_{\mathrm{p},k}(j\dot{\omega}) \, \mathrm{d}\dot{\omega} \\
&= \kappa_{\mathrm{p}}^2 \sum_{k=1}^{n} \frac{\Gamma_{kk}}{2\pi} \int_{-\infty}^{\infty} \hat{h}_{\mathrm{p},k}(j\dot{\omega})^* \hat{h}_{\mathrm{p},k}(j\dot{\omega}) \, \mathrm{d}\dot{\omega} =: \kappa_{\mathrm{p}}^2 \sum_{k=1}^{n} \Gamma_{kk} \|\hat{h}_{\mathrm{p},k}\|_{\mathcal{H}_2}^2 ,
\end{aligned}$$

where the third equality is due to the cyclic property of the trace and the fourth equality is by the property of orthogonal matrix, i.e., $\boldsymbol{U}^T \boldsymbol{U} = \boldsymbol{I}_n$. A similar argument on $\|\hat{\boldsymbol{T}}_{\omega \mathrm{n}_\omega}\|_{\mathcal{H}_2}^2$ yields the desired result. □

Theorem 3.5 allows us to compute the $\mathcal{H}_2$ norm of the system $\hat{\boldsymbol{T}}_{\omega \mathrm{n}}(s)$ by

computing the $\mathcal{H}_2$ norms of a set of simple scalar transfer functions. Although the specific transfer functions $\hat{h}_{\mathrm{p},k}(s)$ and $\hat{h}_{\omega,k}(s)$ will change according to the detailed generator and inverter dynamics involved, in the case where these transfer functions are of fourth-order or lower, the following lemma will suffice for the purpose of our comparison.

Lemma 3.5 ($\mathcal{H}_2$ Norm of a Fourth-Order Transfer Function). *Consider a stable transfer function*

$$\hat{h}(s) = \frac{b_3 s^3 + b_2 s^2 + b_1 s + b_0}{s^4 + a_3 s^3 + a_2 s^2 + a_1 s + a_0} + b_4 \,. \tag{3.36}$$

Then its $\mathcal{H}_2$ norm is given by

$$\|\hat{h}\|_{\mathcal{H}_2}^2 = \begin{cases} \infty & \text{if } b_4 \neq 0 \\ \dfrac{\zeta_0 b_0^2 + \zeta_1 b_1^2 + \zeta_2 b_2^2 + \zeta_3 b_3^2 + \zeta_4}{2a_0\left(a_1 a_2 a_3 - a_1^2 - a_0 a_3^2\right)} & \text{if } b_4 = 0 \end{cases}, \tag{3.37}$$

where

$$\zeta_0 := a_2 a_3 - a_1 \,, \qquad \zeta_1 := a_0 a_3 \,, \qquad \zeta_2 := a_0 a_1 \,, \qquad \zeta_3 := a_0 a_1 a_2 - a_0^2 a_3 \,,$$

$$\zeta_4 := -2a_0(a_1 b_1 b_3 + a_3 b_0 b_2) \,. \tag{3.38}$$

Proof. We can calculate $\|\hat{h}\|_{\mathcal{H}_2}^2$ by applying the approach provided at the end of Section 2.3.1 to the scalar transfer function $\hat{h}(s)$. That is, given any state-space realization of the stable transfer function $\hat{h}(s)$, i.e.,

$$\Sigma_{\hat{h}(s)} = \left[\begin{array}{c|c} \boldsymbol{A} & \boldsymbol{B} \\ \hline \boldsymbol{C} & D \end{array}\right],$$

we have

$$\|\hat{h}\|_{\mathcal{H}_2}^2 = \begin{cases} \infty & \text{if } D \neq 0 \\ \boldsymbol{C}\boldsymbol{X}\boldsymbol{C}^T & \text{if } D = 0 \end{cases}, \tag{3.39}$$

where $\boldsymbol{X}$ denotes the solution to the Lyapunov equation

$$\boldsymbol{A}\boldsymbol{X} + \boldsymbol{X}\boldsymbol{A}^T = -\boldsymbol{B}\boldsymbol{B}^T . \tag{3.40}$$

Consider the observable canonical form [51, Section 4.1.6] of $\hat{h}(s)$ given by

$$\Sigma_{\hat{h}(s)} = \left[\begin{array}{cccc|c} 0 & 0 & 0 & -a_0 & b_0 \\ 1 & 0 & 0 & -a_1 & b_1 \\ 0 & 1 & 0 & -a_2 & b_2 \\ 0 & 0 & 1 & -a_3 & b_3 \\ \hline 0 & 0 & 0 & 1 & b_4 \end{array}\right] . \tag{3.41}$$

Since $D = b_4$, it is trivial to see from (3.39) that if $b_4 \neq 0$ then $\|\hat{h}\|_{\mathcal{H}_2}^2 = \infty$. Hence, in the rest of the proof, we assume $b_4 = 0$. We will now solve the Lyapunov equation analytically for the realization (3.41). From (2.38), we know that $\boldsymbol{X}$ must be symmetric. Thus, it can be parameterized as

$$\boldsymbol{X} = \left[X_{ij}\right] \in \mathbb{R}^{4\times 4} \qquad \text{with} \qquad X_{ij} = X_{ji} . \tag{3.42}$$

Since it is easy to see that $\boldsymbol{C}\boldsymbol{X}\boldsymbol{C}^T = X_{44}$, the problem becomes solving for X_{44}. Substituting (3.41) and (3.42) into (3.40) yields the following equations

$$2a_0 X_{14} = b_0^2 , \tag{3.43a}$$

$$X_{12} - a_2 X_{14} - a_0 X_{34} = - b_0 b_2 , \tag{3.43b}$$

$$2(X_{12} - a_1 X_{24}) = - b_1^2 , \tag{3.43c}$$

$$X_{23} - a_3 X_{24} + X_{14} - a_1 X_{44} = -b_1 b_3 \,, \tag{3.43d}$$

$$2(X_{23} - a_2 X_{34}) = -b_2^2 \,, \tag{3.43e}$$

$$2(X_{34} - a_3 X_{44}) = -b_3^2 \,. \tag{3.43f}$$

Since $\hat{h}(s)$ is stable, by the Routh-Hurwitz criterion $a_0 \neq 0$. Thus, (3.43a) yields

$$X_{14} = \frac{b_0^2}{2a_0} \,. \tag{3.44}$$

Applying (3.44) to (3.43b) and (3.43d) gives

$$X_{12} = a_0 X_{34} + \frac{a_2 b_0^2}{2a_0} - b_0 b_2 \,, \tag{3.45a}$$

$$X_{23} - a_3 X_{24} = a_1 X_{44} - \frac{b_0^2}{2a_0} - b_1 b_3 \,. \tag{3.45b}$$

We now parameterize unknowns in X_{44}. Equation (3.43f) yields

$$X_{34} = a_3 X_{44} - \frac{b_3^2}{2} \,. \tag{3.46}$$

Substituting (3.46) into (3.43e) and (3.45a) gives

$$X_{23} = a_2 a_3 X_{44} - \frac{a_2 b_3^2 + b_2^2}{2} \,, \tag{3.47a}$$

$$X_{12} = a_0 a_3 X_{44} - \frac{a_0 b_3^2}{2} + \frac{a_2 b_0^2}{2a_0} - b_0 b_2 \,, \tag{3.47b}$$

respectively. Plugging (3.47b) into (3.43c) leads to

$$a_1 X_{24} = a_0 a_3 X_{44} - \frac{a_0 b_3^2}{2} + \frac{a_2 b_0^2}{2a_0} - b_0 b_2 + \frac{b_1^2}{2} \,. \tag{3.48}$$

Combining (3.45b), (3.47a), and (3.48), we can solve for X_{44} as the right hand side of (3.37) for $b_4 = 0$, which concludes the proof; the denominator is guaranteed to be nonzero by the Routh-Hurwitz criterion. □

Remark 3.5 ($\mathcal{H}_2$ Norm of a Transfer Function Lower Than Fourth-Order). *Although Lemma 3.5 is stated for a fourth-order transfer function, it can also be used to find the $\mathcal{H}_2$ norm of third-, second-, and first-order transfer functions by considering appropriate limits. For example, setting $a_0 = b_0 = \rho$ and considering the limit $\rho \to 0$, (3.37) gives the $\mathcal{H}_2$ norm of a generic third-order transfer function. This process shows that, given a stable transfer function $\hat{h}(s)$, if $b_4 = 0$ and:*

- *(third-order) $a_0 = b_0 = 0$, then*

$$\|\hat{h}\|_{\mathcal{H}_2}^2 = \frac{a_3 b_1^2 + a_1 b_2^2 + a_1 a_2 b_3^2 - 2 a_1 b_1 b_3}{2 a_1 (a_2 a_3 - a_1)};$$

- *(second-order) $a_0 = b_0 = a_1 = b_1 = 0$, then*

$$\|\hat{h}\|_{\mathcal{H}_2}^2 = \frac{b_2^2 + a_2 b_3^2}{2 a_2 a_3};$$

- *(first-order) $a_0 = b_0 = a_1 = b_1 = a_2 = b_2 = 0$, then*

$$\|\hat{h}\|_{\mathcal{H}_2}^2 = \frac{b_3^2}{2 a_3};$$

otherwise, $\|\hat{h}\|_{\mathcal{H}_2}^2 = \infty$.

Remark 3.6 (Well-Definedness by the Stability). *Note that the stability of $\hat{h}(s)$ guarantees that the denominators in all the above $\mathcal{H}_2$ norm expressions are nonzero by the Routh-Hurwitz stability criterion.*

3.2.6 Steady-State Effort Share

As indicated by (2.46), the key of computing the steady-state effort share lies in computing the steady-state frequency deviation $\boldsymbol{\omega}(\infty)$ of the system $\hat{\boldsymbol{T}}_{\omega\mathrm{p}}(s)$. By Lemma 3.2, in the steady-state, the system $\hat{\boldsymbol{T}}_{\omega\mathrm{p}}(s)$ synchronizes to $\boldsymbol{\omega}(\infty) = \omega_{\mathrm{syn}}\mathbf{1}_n$. With the formula for ω_{syn} in (3.18), we can easily get an explicit expression for the steady-state effort share as provided in the theorem below.

Theorem 3.6 (Steady-State Effort Share). *Let Assumptions 2.2 and 3.2 hold. If $p_{\mathrm{b},i}$ is determined by a control law $\hat{c}_i(s)$, $\forall i \in [n]$, then the steady-state effort share of the system $\hat{\boldsymbol{T}}_{\omega\mathrm{p}}(s)$ is given by*

$$\eta_{\mathrm{es}} = \left| \frac{\sum_{i=1}^{n} \hat{c}_i(0)}{\sum_{i=1}^{n} \left(\alpha_{\mathrm{l},i} + \alpha_{\mathrm{t},i} - \hat{c}_i(0)\right)} \right| . \tag{3.49}$$

Proof. It follows directly from Lemma 3.2 that $\omega_i(\infty) = \omega_{\mathrm{syn}}$ and

$$\sum_{i=1}^{n} p_{\mathrm{in},i}(0^+) = \sum_{i=1}^{n} \mu_{0,i} = \omega_{\mathrm{syn}} \sum_{i=1}^{n} \left(\alpha_{\mathrm{l},i} + \alpha_{\mathrm{t},i} - \hat{c}_i(0)\right) .$$

Plugging these two equations to the definition of the steady-state effort share η_{es} in (2.46) yields (3.49). □

Chapter 4

Performance Analysis of Frequency Control via Inverter-Interfaced Energy Storage

This chapter formally compares the performance of the traditional control laws—droop control (DC) and virtual inertia (VI)—with that of our proposed control laws—dynamic droop control (iDroop) and frequency shaping control (FS)—for frequency control via inverter-interfaced energy storage, which serves as both a motivation and a justification for our research. In Section 4.1, we illustrate the limitations of DC and VI so as to motivate the need for new control laws. In Section 4.2, we suggest iDroop as an improved alternative to DC and VI, whose advantages are verified through rigorous analysis using explicit expressions for performance metrics with the aid of the generic results in Chapter 3. In Section 4.3, we extend iDroop to FS by providing it with the extra ability to tune the RoCoF.

4.1 Traditional Control Laws: Droop Control and Virtual Inertia

Both DC and VI rest on the idea of imitating synchronous generator behavior via inverter-interfaced energy storage, where the former only provides additional droop response but the latter also compensates for inertial response.

Inverter Dynamics 1 (Droop Control). *The dynamics of an inverter with DC is given by the transfer function*

$$\hat{c}_i(s) = -\alpha_{\mathrm{b},i} \ , \tag{4.1}$$

where $\alpha_{\mathrm{b},i} > 0$ *is the inverter inverse droop coefficient.*

Inverter Dynamics 2 (Virtual Inertia). *The dynamics of an inverter with VI is given by the transfer function*

$$\hat{c}_i(s) = -\left(m_{\mathrm{v},i}s + \alpha_{\mathrm{b},i}\right) \ , \tag{4.2}$$

where $m_{\mathrm{v},i} > 0$ *is the virtual inertia constant.*

Under Assumption 3.1, the representative inverters under DC in (4.1) and VI in (4.2) are given by

$$\hat{c}_{\mathrm{o}}(s) = -\alpha_{\mathrm{b,o}} \tag{4.3}$$

and

$$\hat{c}_{\mathrm{o}}(s) = -\left(m_{\mathrm{v,o}}s + \alpha_{\mathrm{b,o}}\right) \tag{4.4}$$

with $m_{\mathrm{v},i} = r_i m_{\mathrm{v,o}}$ and $\alpha_{\mathrm{b},i} = r_i \alpha_{\mathrm{b,o}}$, $\forall i \in [n]$. To streamline the notation, we define $\breve{\alpha}_{\mathrm{o}} := \alpha_{\mathrm{l,o}} + \alpha_{\mathrm{b,o}}$ and $\breve{m}_{\mathrm{o}} := m_{\mathrm{o}} + m_{\mathrm{v,o}}$.

We now offer the following toy example to develop intuition about the impact of DC and VI via inverter-interfaced energy storage on frequency dynamics in power systems.

Example 4.1 (Great Britain Power System with DC/VI). *Consider the Great Britain power system described in Example 2.1 under the high renewable penetration scenario. Suppose that the inverter-interfaced energy storage characterized by (2.15) is deployed to improve the frequency dynamics of this low-inertia power system. To illustrate the impact of the parameters of DC in (4.1) and VI in (4.2) on frequency dynamics, Figure 4.1 plots system frequency deviations excited by the same p_{l} as in Example 2.1 when $\hat{c}(s) = -(m_{\mathrm{v}}s + \alpha_{\mathrm{b}})$ for different values of the virtual inertia constant $m_{\mathrm{v}} \geq 0$ and the inverter inverse droop coefficient $\alpha_{\mathrm{b}} \geq 0$. Here, we allow the degenerate cases where $m_{\mathrm{v}} = 0$ or $\alpha_{\mathrm{b}} = 0$ for the purpose of investigating the role of these two parameters one at a time. Obviously, in the case that $m_{\mathrm{v}} = \alpha_{\mathrm{b}} = 0$, we recover the original system, where there is no additional control from inverter-interfaced energy storage. Figure 4.1(a) shows the effect of m_{v} on frequency dynamics by fixing $\alpha_{\mathrm{b}} = 0$, from which we learn that m_{v} plays a part only in the transient duration. More precisely, in contrast to the irrelevance of the steady-state frequency to m_{v}, the RoCoF significantly depends on the choice of m_{v}. That is, greater values of m_{v} lead to a decrease of RoCoF, one of whose by-prodcuts is the improved Nadir until the Nadir elimination is achieved. Figure 4.1(b) shows the effect of α_{b} on frequency dynamics by fixing $m_{\mathrm{v}} = 0$, from which we know that α_{b} picks the whole frequency curve up. Especially, α_{b} directly contributes to raising the steady-state frequency up towards the nominal value, which results in the improved Nadir as well. Yet, α_{b} has no influence on the initial RoCoF.*

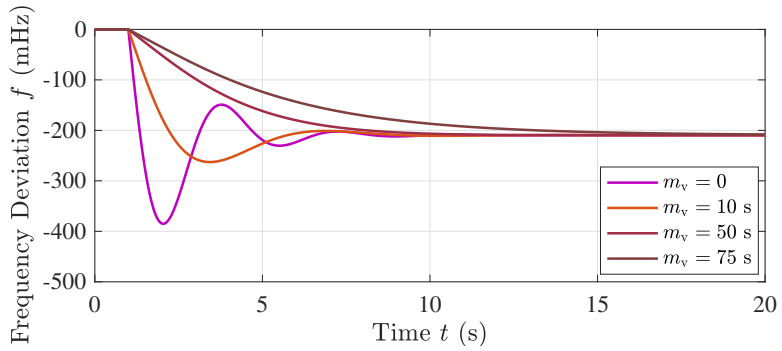

(a) Frequency deviations for various values of m_v, where $\alpha_b = 0$

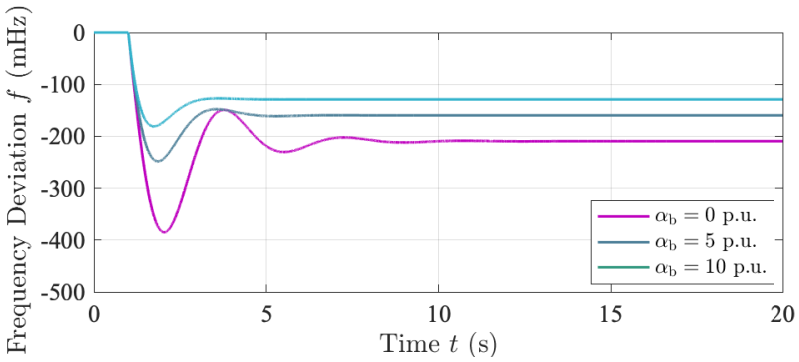

(b) Frequency deviations for various values of α_b, where $m_v = 0$

Figure 4.1: Frequency deviations in Great Britain system with DC or VI via Energy Storage (Example 4.1)

4.1.1 Performance Analysis

We now apply the results in Section 3.2 to illustrate the performance limitations of the traditional control laws DC and VI. With this aim, we seek to quantify the frequency variance (2.45) under DC and VI through the squared $\mathcal{H}_2$ norms of the systems $\hat{\boldsymbol{T}}_{\omega\mathrm{n,DC}}(s)$ and $\hat{\boldsymbol{T}}_{\omega\mathrm{n,VI}}(s)$, as well as the synchronous frequency, Nadir (2.42), RoCoF (2.43), synchronization cost (2.44), and steady-state effort share (2.46) through the step response characterizations of the systems $\hat{\boldsymbol{T}}_{\omega\mathrm{p,DC}}(s)$ and $\hat{\boldsymbol{T}}_{\omega\mathrm{p,VI}}(s)$.[1]

Synchronous Frequency

Corollary 4.1 (Synchronous Frequency via DC and VI). *Let Assumptions 2.2 and 3.2 hold. If $p_{\mathrm{b},i}$ is defined by the control law DC in (4.1) or VI in (4.2), $\forall i \in [n]$, then the steady-state frequency deviation of the respective system $\hat{\boldsymbol{T}}_{\omega\mathrm{p,DC}}(s)$ or $\hat{\boldsymbol{T}}_{\omega\mathrm{p,VI}}(s)$ synchronizes to the synchronous frequency, i.e., $\boldsymbol{\omega}(\infty) = \omega_{\mathrm{syn}}\mathbf{1}_n$ with*

$$\omega_{\mathrm{syn}} = \frac{\sum_{i=1}^{n} \mu_{0,i}}{\sum_{i=1}^{n} \left(\alpha_{\mathrm{l},i} + \alpha_{\mathrm{t},i} + \alpha_{\mathrm{b},i}\right)} \,. \tag{4.5}$$

Proof. The result follows directly from Lemma 3.2 if it is recognized that $\hat{c}_{\mathrm{i}}(0) = -\alpha_{\mathrm{b},i}$, $\forall i \in [n]$, for both DC and VI. □

Corollary 4.1 shows that the magnitude of the synchronous frequency is inversely proportional to the aggregate compensated inverse droop coefficient. Thus, with all other things unchanged, the greater the inverter inverse droop

[1] Depending on the specific inverter dynamics involved, we may add a subscript in the name of a transfer function (matrix) without making a further declaration in the rest of this thesis. Particularly, for the case where there is no additional control from inverter-interfaced energy storage, i.e, $\hat{c}_i(s) = 0$, $\forall i \in [n]$, we would add the subscript "SG".

coefficient $\alpha_{\mathrm{b},i}$ is, the closer the synchronous frequency ω_{syn} is to zero. Yet, without a secondary control layer, which is out of the scope of this thesis, in general, ω_{syn} cannot be made zero unless $\sum_{i=1}^{n} \mu_{0,i} = 0$.

Nadir

With the help of Theorem 3.1, we can determine the conditions that the parameters of DC and VI must satisfy to realize the Nadir elimination of the COI frequency.

Theorem 4.1 (Nadir Elimination via DC and VI). *Let Assumptions 2.2, 3.1, and 3.2 hold. Then the Nadir elimination of the COI frequency of*

- *the system $\hat{\boldsymbol{T}}_{\omega\mathrm{p,DC}}(s)$ is achieved if and only if the parameter $\alpha_{\mathrm{b,o}}$ of DC satisfies*

$$m_{\mathrm{o}} \geq \tau_{\mathrm{t,o}} \left(\sqrt{\alpha_{\mathrm{t,o}}} + \sqrt{\alpha_{\mathrm{l,o}} + \alpha_{\mathrm{b,o}} + \alpha_{\mathrm{t,o}}} \right)^2 \ ; \tag{4.6}$$

- *the system $\hat{\boldsymbol{T}}_{\omega\mathrm{p,VI}}(s)$ is achieved if and only if the parameters $\alpha_{\mathrm{b,o}}$ and $m_{\mathrm{v,o}}$ of VI satisfy*

$$m_{\mathrm{o}} + m_{\mathrm{v,o}} \geq \tau_{\mathrm{t,o}} \left(\sqrt{\alpha_{\mathrm{t,o}}} + \sqrt{\alpha_{\mathrm{l,o}} + \alpha_{\mathrm{b,o}} + \alpha_{\mathrm{t,o}}} \right)^2 \ . \tag{4.7}$$

Proof. We start by deriving the Nadir elimination condition for VI. According to (3.16), the COI frequency deviation of the system $\hat{\boldsymbol{T}}_{\omega\mathrm{p,VI}}(s)$ is given by

$$\bar{\omega}_{\mathrm{VI}}(t) = \frac{\sum_{i=1}^{n} \mu_{0,i}}{\sum_{i=1}^{n} r_i} h_{\mathrm{u,1,VI}}(t) \ ,$$

where $h_{\mathrm{u,1,VI}}(t)$ is the unit-step response of $\hat{h}_{\mathrm{p,1,VI}}(s)$. Clearly, as long as $h_{\mathrm{u,1,VI}}(t)$ achieves the Nadir elimination, so does $\bar{\omega}_{\mathrm{VI}}(t)$. Thus, as shown later,

the core is to apply Theorem 3.1 to $\hat{h}_{\mathrm{p},1,\mathrm{VI}}(s)$. Substituting (3.2) and (4.4) to (3.10) yields

$$\hat{h}_{\mathrm{p},1,\mathrm{VI}}(s) = \frac{1}{\check{m}_{\mathrm{o}}} \frac{s + 1/\tau_{\mathrm{t,o}}}{s^2 + 2\xi\omega_{\mathrm{n}} s + \omega_{\mathrm{n}}^2} \,, \tag{4.8}$$

where

$$\omega_{\mathrm{n}} := \sqrt{\frac{\check{\alpha}_{\mathrm{o}} + \alpha_{\mathrm{t,o}}}{\check{m}_{\mathrm{o}} \tau_{\mathrm{t,o}}}} \qquad \text{and} \qquad \xi := \frac{1/\tau_{\mathrm{t,o}} + \check{\alpha}_{\mathrm{o}}/\check{m}_{\mathrm{o}}}{2\sqrt{\left(\check{\alpha}_{\mathrm{o}} + \alpha_{\mathrm{t,o}}\right) / \left(\check{m}_{\mathrm{o}} \tau_{\mathrm{t,o}}\right)}} \,. \tag{4.9}$$

Now we are ready to search the Nadir elimination tuning region by means of Theorem 3.1. An easy computation shows that the following inequality holds:

$$2\xi\omega_{\mathrm{n}} - \frac{1}{\tau_{\mathrm{t,o}}} = \frac{\check{\alpha}_{\mathrm{o}}}{\check{m}_{\mathrm{o}}} < \frac{\check{\alpha}_{\mathrm{o}} + \alpha_{\mathrm{t,o}}}{\check{m}_{\mathrm{o}}} = \omega_{\mathrm{n}}^2 \tau_{\mathrm{t,o}} \,.$$

Equivalently, it holds that

$$\xi < \frac{1}{2}\left(\frac{1}{\omega_{\mathrm{n}}\tau_{\mathrm{t,o}}} + \omega_{\mathrm{n}}\tau_{\mathrm{t,o}}\right) \,,$$

which indicates that the second set of conditions in (3.22) cannot be satisfied. Hence, we turn to the first set of conditions in (3.22), which holds if and only if $\xi \geq 1$ and $\xi\omega_{\mathrm{n}} \leq 1/\tau_{\mathrm{t,o}}$. Via simple algebraic computations, we know this is equivalent to

$$\begin{cases} \check{m}_{\mathrm{o}}^2 - 2\tau_{\mathrm{t,o}}\left(\check{\alpha}_{\mathrm{o}} + 2\alpha_{\mathrm{t,o}}\right)\check{m}_{\mathrm{o}} + \tau_{\mathrm{t,o}}^2 \check{\alpha}_{\mathrm{o}}^2 \geq 0 \\ \check{m}_{\mathrm{o}} \geq \tau_{\mathrm{t,o}} \check{\alpha}_{\mathrm{o}} \end{cases} . \tag{4.10}$$

The first condition in (4.10) can be viewed as a quadratic inequality with respect to $\check{m}_{\mathrm{o}}$, which holds if and only if

$$\check{m}_{\mathrm{o}} \geq \tau_{\mathrm{t,o}}\left(\sqrt{\alpha_{\mathrm{t,o}}} + \sqrt{\check{\alpha}_{\mathrm{o}} + \alpha_{\mathrm{t,o}}}\right)^2 \quad \text{or} \quad \check{m}_{\mathrm{o}} \leq \tau_{\mathrm{t,o}}\left(\sqrt{\alpha_{\mathrm{t,o}}} - \sqrt{\check{\alpha}_{\mathrm{o}} + \alpha_{\mathrm{t,o}}}\right)^2 .$$

However, only the former region satisfies the second condition in (4.10). This concludes the proof of the second statement. The first statement follows trivially by setting $m_{v,o} = 0$. □

Important inferences can be made from Theorem 4.1. The fact that a small m_o tends to violate the requirement in (4.6) implies that in a low-inertia power system it is hard to achieve the Nadir elimination using only DC. Undoubtedly, the addition of $m_{v,o}$ makes the requirement in (4.7) more accessible, which indicates that VI can help a low-inertia power system largely improve the Nadir.

Remark 4.1 (Critical Value of $\check{m}_o$ for Nadir Elimination). *Theorem 4.1 suggests a critical value of the (compensated) representative inertia constant $\check{m}_o$ dependent on the turbine time constant $\tau_{t,o}$ as well as the inverse droop coefficients $\alpha_{l,o}$, $\alpha_{t,o}$, and $\alpha_{b,o}$ of the representative equipment, beyond which DC and VI are able to realize the Nadir elimination. We denote this value as m_c which is determined by*

$$m_c := \tau_{t,o} \left(\sqrt{\alpha_{t,o}} + \sqrt{\alpha_{l,o} + \alpha_{b,o} + \alpha_{t,o}} \right)^2 .$$

If it is recognized that in reality $\alpha_{l,o}$ and $\alpha_{b,o}$ is much smaller than $\alpha_{t,o}$, an approximate expression for m_c can be derived as

$$\begin{aligned} m_c &= \tau_{t,o} \left(2\alpha_{t,o} + \alpha_{l,o} + \alpha_{b,o} + 2\alpha_{t,o} \sqrt{\frac{\alpha_{l,o} + \alpha_{b,o}}{\alpha_{t,o}} + 1} \right) \\ &\approx \tau_{t,o} \left[2\alpha_{t,o} + \alpha_{l,o} + \alpha_{b,o} + 2\alpha_{t,o} \left(1 + \frac{\alpha_{l,o} + \alpha_{b,o}}{2\alpha_{t,o}} \right) \right] \\ &= 2\tau_{t,o} \left(2\alpha_{t,o} + \alpha_{l,o} + \alpha_{b,o} \right) , \end{aligned}$$

where the second line is obtained by ignoring higher order terms in the binomial series. Noticeably, the required m_c for Nadir elimination has rather high values, which makes it unrealistic to rely on DC or VI to take charge of this.

RoCoF

Corollary 4.2 (RoCoF under DC and VI). *Let Assumptions 2.2, 3.1, and 3.2 hold. Then the RoCoF of the COI frequency of the systems $\hat{\boldsymbol{T}}_{\omega \mathrm{p,DC}}(s)$ and $\hat{\boldsymbol{T}}_{\omega \mathrm{p,VI}}(s)$ are given by*

$$\|\dot{\bar{\omega}}_{\mathrm{DC}}\|_{\mathcal{L}_\infty} = \frac{|\sum_{i=1}^n \mu_{0,i}|}{\sum_{i=1}^n r_i} \frac{1}{m_{\mathrm{o}}} \qquad \textit{and} \qquad \|\dot{\bar{\omega}}_{\mathrm{VI}}\|_{\mathcal{L}_\infty} = \frac{|\sum_{i=1}^n \mu_{0,i}|}{\sum_{i=1}^n r_i} \frac{1}{m_{\mathrm{o}} + m_{\mathrm{v,o}}},$$

respectively.

Proof. We start by deriving the RoCoF for VI. From the proof of Theorem 4.1, we know that

$$\hat{\bar{\omega}}_{\mathrm{VI}}(s) = \frac{\sum_{i=1}^n \mu_{0,i}}{\sum_{i=1}^n r_i} \frac{\hat{h}_{\mathrm{p,1,VI}}(s)}{s}$$

with $\hat{h}_{\mathrm{p,1,VI}}(s)$ given by (4.8). Thus, $\bar{\omega}_{\mathrm{VI}}(t)$ is equivalent to the unit-step response of the second-order system $\hat{h}_{\mathrm{p,1,VI}}(s)$ scaled by $(\sum_{i=1}^n \mu_{0,i})/(\sum_{i=1}^n r_i)$. Thus, we can apply Theorem 3.3 to $\hat{h}_{\mathrm{p,1,VI}}(s)$. Clearly,

$$2\xi\omega_{\mathrm{n}} = 2\frac{1/\tau_{\mathrm{t,o}} + \check{\alpha}_{\mathrm{o}}/\check{m}_{\mathrm{o}}}{2\sqrt{(\check{\alpha}_{\mathrm{o}} + \alpha_{\mathrm{t,o}}) \,/\, (\check{m}_{\mathrm{o}}\tau_{\mathrm{t,o}})}} \sqrt{\frac{\check{\alpha}_{\mathrm{o}} + \alpha_{\mathrm{t,o}}}{\check{m}_{\mathrm{o}}\tau_{\mathrm{t,o}}}} = \frac{1}{\tau_{\mathrm{t,o}}} + \frac{\check{\alpha}_{\mathrm{o}}}{\check{m}_{\mathrm{o}}} > \frac{1}{\tau_{\mathrm{t,o}}} = z\,.$$

Thus, by Theorem 3.3,

$$\|\dot{\bar{\omega}}_{\mathrm{VI}}\|_{\mathcal{L}_\infty} = \left|\frac{\sum_{i=1}^n \mu_{0,i}}{\sum_{i=1}^n r_i}\right| K = \frac{|\sum_{i=1}^n \mu_{0,i}|}{\sum_{i=1}^n r_i} \frac{1}{\check{m}_{\mathrm{o}}},$$

which concludes the proof for VI. The result for DC follows trivially by setting $m_{\mathrm{v,o}} = 0$. □

Remark 4.2 (RoCoF of the Original System). *From the proof of Corollary 4.2, we can directly get the RoCoF of the original system without additional control from inverter-interfaced energy storage by further setting $\alpha_{\mathrm{b,o}} = 0$ on top of DC which in fact is a parameter that is irrelative to RoCoF. By doing so, we can get*

$$\|\dot{\omega}_{\mathrm{SG}}\|_{\mathcal{L}_\infty} = \frac{|\sum_{i=1}^{n} \mu_{0,i}|}{\sum_{i=1}^{n} r_i} \frac{1}{m_{\mathrm{o}}}.$$

Synchronization Cost

Theorem 3.4 implies that the synchronization costs of the system $\hat{\boldsymbol{T}}_{\omega \mathrm{p,DC}}(s)$ and the system $\hat{\boldsymbol{T}}_{\omega \mathrm{p,VI}}(s)$ are bounded by a weighted sum of $\|\hat{h}_{\mathrm{u},k+1,\mathrm{DC}}\|_{\mathcal{H}_2}^2$ and $\|\hat{h}_{\mathrm{u},k+1,\mathrm{VI}}\|_{\mathcal{H}_2}^2$ over $k \in [n-1]$, respectively. Hence, in order to see the limited ability of DC and VI to reduce the synchronization cost, we need to first gain a deeper understanding of $\|\hat{h}_{\mathrm{u},k+1,\mathrm{DC}}\|_{\mathcal{H}_2}^2$ and $\|\hat{h}_{\mathrm{u},k+1,\mathrm{VI}}\|_{\mathcal{H}_2}^2$.

Theorem 4.2 (Bounds of $\|\hat{h}_{\mathrm{u},k+1,\mathrm{DC}}\|_{\mathcal{H}_2}^2$ and $\|\hat{h}_{\mathrm{u},k+1,\mathrm{VI}}\|_{\mathcal{H}_2}^2$). *Let Assumptions 2.2, 3.1, and 3.2 hold. Then, $\forall k \in [n-1]$, given $\alpha_{\mathrm{b,o}} > 0$, $\forall m_{\mathrm{v,o}} > 0$,*

$$\frac{1}{2\lambda_{k+1}\left(\check{\alpha}_{\mathrm{o}} + \alpha_{\mathrm{t,o}}\right)} < \|\hat{h}_{\mathrm{u},k+1,\mathrm{VI}}\|_{\mathcal{H}_2}^2 < \|\hat{h}_{\mathrm{u},k+1,\mathrm{DC}}\|_{\mathcal{H}_2}^2 < \|\hat{h}_{\mathrm{u},k+1,\mathrm{SG}}\|_{\mathcal{H}_2}^2.$$

Proof. Considering that DC can be viewed as VI with $m_{\mathrm{v,o}} = 0$ and the case without additional control from inverters can be viewed as VI with $m_{\mathrm{v,o}} = \alpha_{\mathrm{b,o}} = 0$, we only compute $\|\hat{h}_{\mathrm{u},k+1,\mathrm{VI}}\|_{\mathcal{H}_2}^2$, which straightforwardly implies $\|\hat{h}_{\mathrm{u},k+1,\mathrm{DC}}\|_{\mathcal{H}_2}^2$ and $\|\hat{h}_{\mathrm{u},k+1,\mathrm{SG}}\|_{\mathcal{H}_2}^2$. Applying (3.2) and (4.4) to (3.10) shows that $\hat{h}_{\mathrm{u},k+1,\mathrm{VI}}(s) = \hat{h}_{\mathrm{p},k+1,\mathrm{VI}}(s)/s$ is a transfer function in the form of (3.36) with $b_4 = a_0 = b_0 = 0$, $a_1 = \lambda_{k+1}/\left(\check{m}_{\mathrm{o}}\tau_{\mathrm{t,o}}\right)$, $b_1 = 1/\left(\check{m}_{\mathrm{o}}\tau_{\mathrm{t,o}}\right)$, $a_2 = \left(\check{\alpha}_{\mathrm{o}} + \alpha_{\mathrm{t,o}} + \lambda_{k+1}\tau_{\mathrm{t,o}}\right)/\left(\check{m}_{\mathrm{o}}\tau_{\mathrm{t,o}}\right)$, $b_2 = 1/\check{m}_{\mathrm{o}}$, $a_3 = \left(\check{m}_{\mathrm{o}} + \check{\alpha}_{\mathrm{o}}\tau_{\mathrm{t,o}}\right)/\left(\check{m}_{\mathrm{o}}\tau_{\mathrm{t,o}}\right)$, and

$b_3 = 0$. Then it follows from Lemma 3.5 that

$$\|\hat{h}_{\mathrm{u},k+1,\mathrm{VI}}\|_{\mathcal{H}_2}^2 = \frac{\check{m}_{\mathrm{o}} + \tau_{\mathrm{t,o}}\left(\lambda_{k+1}\tau_{\mathrm{t,o}} + \check{\alpha}_{\mathrm{o}}\right)}{2\lambda_{k+1}\left[\tau_{\mathrm{t,o}}\check{\alpha}_{\mathrm{o}}\left(\lambda_{k+1}\tau_{\mathrm{t,o}} + \check{\alpha}_{\mathrm{o}} + \alpha_{\mathrm{t,o}}\right) + \check{m}_{\mathrm{o}}\left(\check{\alpha}_{\mathrm{o}} + \alpha_{\mathrm{t,o}}\right)\right]}\,.$$

Since $\|\hat{h}_{\mathrm{u},k+1,\mathrm{VI}}\|_{\mathcal{H}_2}^2$ is a function of $\alpha_{\mathrm{b,o}}$ and $m_{\mathrm{v,o}}$, in what follows we denote it by $\zeta(\alpha_{\mathrm{b,o}}, m_{\mathrm{v,o}})$. In order to have an insight on how $\|\hat{h}_{\mathrm{u},k+1,\mathrm{VI}}\|_{\mathcal{H}_2}^2$ changes with $\alpha_{\mathrm{b,o}}$ and $m_{\mathrm{v,o}}$, we take partial derivatives of $\zeta(\alpha_{\mathrm{b,o}}, m_{\mathrm{v}})$ with respect to $\alpha_{\mathrm{b,o}}$ and $m_{\mathrm{v,o}}$, i.e.,

$$\partial_{\alpha_{\mathrm{b,o}}}\zeta(\alpha_{\mathrm{b,o}}, m_{\mathrm{v,o}}) = -\frac{\left[\check{m}_{\mathrm{o}} + \tau_{\mathrm{t,o}}\left(\lambda_{k+1}\tau_{\mathrm{t,o}} + \check{\alpha}_{\mathrm{o}}\right)\right]^2 + \lambda_{k+1}\tau_{\mathrm{t,o}}^3\alpha_{\mathrm{t,o}}}{2\lambda_{k+1}\left[\tau_{\mathrm{t,o}}\check{\alpha}_{\mathrm{o}}\left(\lambda_{k+1}\tau_{\mathrm{t,o}} + \check{\alpha}_{\mathrm{o}} + \alpha_{\mathrm{t,o}}\right) + \check{m}_{\mathrm{o}}\left(\check{\alpha}_{\mathrm{o}} + \alpha_{\mathrm{t,o}}\right)\right]^2}\,,$$

$$\partial_{m_{\mathrm{v,o}}}\zeta(\alpha_{\mathrm{b,o}}, m_{\mathrm{v,o}}) = -\frac{\tau_{\mathrm{t,o}}^2\alpha_{\mathrm{t,o}}}{2\left[\tau_{\mathrm{t,o}}\check{\alpha}_{\mathrm{o}}\left(\lambda_{k+1}\tau_{\mathrm{t,o}} + \check{\alpha}_{\mathrm{o}} + \alpha_{\mathrm{t,o}}\right) + \check{m}_{\mathrm{o}}\left(\check{\alpha}_{\mathrm{o}} + \alpha_{\mathrm{t,o}}\right)\right]^2}\,.$$

Clearly, $\forall \alpha_{\mathrm{b,o}} \geq 0$, we have $\partial_{\alpha_{\mathrm{b,o}}}\zeta(\alpha_{\mathrm{b,o}}, m_{\mathrm{v,o}}) < 0$, which means that $\zeta(\alpha_{\mathrm{b,o}}, m_{\mathrm{v,o}})$ is a monotonically decreasing function of $\alpha_{\mathrm{b,o}}$. Similarly, $\forall m_{\mathrm{v,o}} \geq 0$, we have $\partial_{m_{\mathrm{v,o}}}\zeta(\alpha_{\mathrm{b,o}}, m_{\mathrm{v,o}}) < 0$, which means that $\zeta(\alpha_{\mathrm{b,o}}, m_{\mathrm{v,o}})$ is a monotonically decreasing function of $m_{\mathrm{v,o}}$. Therefore, given $\alpha_{\mathrm{b,o}} > 0$, $\forall m_{\mathrm{v,o}} > 0$, it holds that

$$\lim_{m_{\mathrm{v,o}}\to\infty}\zeta(\alpha_{\mathrm{b,o}}, m_{\mathrm{v,o}}) < \zeta(\alpha_{\mathrm{b,o}}, m_{\mathrm{v,o}}) < \zeta(\alpha_{\mathrm{b,o}}, 0) < \zeta(0,0)\,.$$

Finally, recall that $\|\hat{h}_{\mathrm{u},k+1,\mathrm{VI}}\|_{\mathcal{H}_2}^2 = \zeta(\alpha_{\mathrm{b,o}}, m_{\mathrm{v,o}})$, $\|\hat{h}_{\mathrm{u},k+1,\mathrm{DC}}\|_{\mathcal{H}_2}^2 = \zeta(\alpha_{\mathrm{b,o}}, 0)$, and $\|\hat{h}_{\mathrm{u},k+1,\mathrm{SG}}\|_{\mathcal{H}_2}^2 = \zeta(0,0)$. The result follows. □

Corollary 4.3 (Ordering of Synchronization Costs in Homogeneous Case). *Let Assumptions 2.2, 3.1, and 3.2 hold. If $\boldsymbol{R} = r\boldsymbol{I}_n$ for some $r > 0$, then, given $\alpha_{\mathrm{b,o}} > 0$, $\forall m_{\mathrm{v,o}} > 0$, we can order the synchronization costs as:*

$$\frac{\sum_{k=1}^{n-1}\left(\tilde{\mu}_{0,k}^2/\lambda_{k+1}\right)}{2r\left(\check{\alpha}_{\mathrm{o}} + \alpha_{\mathrm{t,o}}\right)} < \|\tilde{\boldsymbol{\omega}}_{\mathrm{VI}}\|_{\mathcal{L}_2}^2 < \|\tilde{\boldsymbol{\omega}}_{\mathrm{DC}}\|_{\mathcal{L}_2}^2 < \|\tilde{\boldsymbol{\omega}}_{\mathrm{SG}}\|_{\mathcal{L}_2}^2\,.$$

Proof. The result follows by combining Remark 3.4 and Theorem 4.2. □

Corollary 4.4 (Lower Bound of Synchronization Costs under DC and VI). *Let Assumptions 2.2, 3.1, and 3.2 hold. For a proportionally heterogeneous power system, the ordering of the sizes of the bounds on the synchronization cost in the case without additional control from inverters, the case with DC, and the case with VI depends on the parameter values. Thus, we cannot order* $\|\tilde{\omega}_{\mathrm{VI}}\|_{\mathcal{L}_2}^2$, $\|\tilde{\omega}_{\mathrm{DC}}\|_{\mathcal{L}_2}^2$, *and* $\|\tilde{\omega}_{\mathrm{SG}}\|_{\mathcal{L}_2}^2$ *strictly in general. Instead, we highlight that, given* $\alpha_{\mathrm{b,o}} > 0$, *the synchronization cost under DC and VI are bounded below by*

$$\frac{\sum_{k=1}^{n-1}\left(\tilde{\mu}_{0,k}^2/\lambda_{k+1}\right)}{2\max_{i\in[n]}\left(r_i\right)\left(\breve{\alpha}_{\mathrm{o}}+\alpha_{\mathrm{t,o}}\right)}.$$

Proof. The result follows from Theorems 3.4 and 4.2. □

Corollary 4.3 provides both upper and lower bounds for the synchronization costs under DC and VI in the homogeneous case. The upper bound verifies that DC and VI do reduce the synchronization cost by introducing additional droop and inertial response while the lower bound indicates that the reduction of the synchronization cost through DC and VI is limited by certain value that is dependent on $\alpha_{\mathrm{b,o}}$. Corollary 4.4 implies that, in the proportionally heterogeneous case, the synchronization costs under DC and VI are also bounded below by a value that is dependent on $\alpha_{\mathrm{b,o}}$. More precisely, the lower bound of the synchronization costs under DC and VI is reduced as $\alpha_{\mathrm{b,o}}$ increases.

Frequency Variance

Using Theorem 3.5 and Lemma 3.5, it is possible to get closed-form expressions of the squared $\mathcal{H}_2$ norms for the systems $\hat{\boldsymbol{T}}_{\omega\mathrm{n,DC}}(s)$ and $\hat{\boldsymbol{T}}_{\omega\mathrm{n,VI}}(s)$, which can be interpreted as the frequency variances of the respective systems facing stochastic power fluctuations and frequency measurement noise.

Corollary 4.5 (Frequency Variances under DC and VI). *Let Assumptions 2.2, 3.1, and 3.3 hold. The squared $\mathcal{H}_2$ norms of the systems $\hat{\boldsymbol{T}}_{\omega\mathrm{n,DC}}(s)$ and $\hat{\boldsymbol{T}}_{\omega\mathrm{n,VI}}(s)$ are given by*

$$\|\hat{\boldsymbol{T}}_{\omega\mathrm{n,DC}}\|_{\mathcal{H}_2}^2 = \frac{\kappa_{\mathrm{p}}^2 + \kappa_\omega^2 \alpha_{\mathrm{b,o}}^2}{2m_{\mathrm{o}}\breve{\alpha}_{\mathrm{o}}} \sum_{i=1}^{n} \frac{1}{r_i}\,, \tag{4.11a}$$

$$\|\hat{\boldsymbol{T}}_{\omega\mathrm{n,VI}}\|_{\mathcal{H}_2}^2 = \infty\,, \tag{4.11b}$$

respectively.

Proof. We study the two cases separately.

We begin with $\|\hat{\boldsymbol{T}}_{\omega\mathrm{n,DC}}\|_{\mathcal{H}_2}^2$. Applying (3.1) and (4.3) to (3.10) and (3.11) shows that $\hat{h}_{\mathrm{p},k,\mathrm{DC}}(s)$ is a transfer function in the form of (3.36) with $b_4 = a_0 = b_0 = a_1 = b_1 = 0$, $a_2 = \lambda_k/m_{\mathrm{o}}$, $b_2 = 0$, $a_3 = \breve{\alpha}_{\mathrm{o}}/m_{\mathrm{o}}$, $b_3 = 1/m_{\mathrm{o}}$, while $\hat{h}_{\omega,k,\mathrm{DC}}(s)$ is a transfer function in the form of (3.36) with $b_4 = a_0 = b_0 = a_1 = b_1 = 0$, $a_2 = \lambda_k/m_{\mathrm{o}}$, $b_2 = 0$, $a_3 = \breve{\alpha}_{\mathrm{o}}/m_{\mathrm{o}}$, $b_3 = -\alpha_{\mathrm{b,o}}/m_{\mathrm{o}}$. Thus, by Lemma 3.5,

$$\|\hat{h}_{\mathrm{p},k,\mathrm{DC}}\|_{\mathcal{H}_2}^2 = \frac{1}{2m_{\mathrm{o}}\breve{\alpha}_{\mathrm{o}}} \qquad \text{and} \qquad \|\hat{h}_{\omega,k,\mathrm{DC}}\|_{\mathcal{H}_2}^2 = \frac{\alpha_{\mathrm{b,o}}^2}{2m_{\mathrm{o}}\breve{\alpha}_{\mathrm{o}}}\,, \qquad \forall k \in [n]\ .$$

Then it follows from Theorem 3.5 that

$$\|\hat{\boldsymbol{T}}_{\omega\mathrm{n,DC}}\|_{\mathcal{H}_2}^2 = \sum_{k=1}^{n} \Gamma_{kk} \frac{\kappa_{\mathrm{p}}^2 + \kappa_\omega^2 \alpha_{\mathrm{b,o}}^2}{2m_{\mathrm{o}}\check{\alpha}_{\mathrm{o}}} = \frac{\kappa_{\mathrm{p}}^2 + \kappa_\omega^2 \alpha_{\mathrm{b,o}}^2}{2m_{\mathrm{o}}\check{\alpha}_{\mathrm{o}}} \sum_{k=1}^{n} \Gamma_{kk}\,. \tag{4.12}$$

Note that

$$\sum_{k=1}^{n} \Gamma_{kk} = \sum_{i=1}^{n} \lambda_i(\boldsymbol{\Gamma}) = \sum_{i=1}^{n} \lambda_i(\boldsymbol{U}^T \boldsymbol{R}^{-1} \boldsymbol{U}) = \sum_{i=1}^{n} \lambda_i(\boldsymbol{R}^{-1}) = \sum_{i=1}^{n} \frac{1}{r_i}\,. \tag{4.13}$$

The first and last equalities use the property of the trace. The second equality is a direct result of the definition that $\boldsymbol{\Gamma} := \boldsymbol{U}^T \boldsymbol{R}^{-1} \boldsymbol{U}$. The third equality is due to the similarity between $\boldsymbol{R}^{-1}$ and $\boldsymbol{U}^T \boldsymbol{R}^{-1} \boldsymbol{U}$, which has been discussed in the proof of Theorem 3.4. Applying (4.13) to (4.12), we get (4.11a).

We now turn to show that $\|\hat{\boldsymbol{T}}_{\omega\mathrm{n,VI}}\|_{\mathcal{H}_2}^2$ is infinite. Applying (3.1) and (4.4) to (3.11) yields

$$\hat{h}_{\omega,k,\mathrm{VI}}(s) = -\frac{m_{\mathrm{v,o}} s^2 + \alpha_{\mathrm{b,o}} s}{\check{m}_{\mathrm{o}} s^2 + \check{\alpha}_{\mathrm{o}} s + \lambda_k}\,,$$

which if turned into the form of (3.36) has $b_4 = \hat{h}_{\omega,k,\mathrm{VI}}(\infty) = -m_{\mathrm{v,o}}/\check{m}_{\mathrm{o}} \neq 0$. Thus, by Lemma 3.5, $\|\hat{h}_{\omega,k,\mathrm{VI}}\|_{\mathcal{H}_2}^2 = \infty$. Then (4.11b) follows directly from Theorem 3.5. □

Corollary 4.6 (Optimal $\alpha_{\mathrm{b,o}}$ for $\|\hat{\boldsymbol{T}}_{\omega\mathrm{n,DC}}\|_{\mathcal{H}_2}^2$). *Let Assumptions 2.2, 3.1, and 3.3 hold. Then*

$$\alpha_{\mathrm{b,o}}^\star := \operatorname*{argmin}_{\alpha_{\mathrm{b,o}} > 0} \|\hat{\boldsymbol{T}}_{\omega\mathrm{n,DC}}\|_{\mathcal{H}_2}^2 = -\alpha_{\mathrm{l,o}} + \sqrt{\alpha_{\mathrm{l,o}}^2 + \left(\frac{\kappa_{\mathrm{p}}}{\kappa_\omega}\right)^2}\,. \tag{4.14}$$

Proof. The partial derivative of $\|\hat{\boldsymbol{T}}_{\omega\mathrm{n,DC}}\|_{\mathcal{H}_2}^2$ with respect to $\alpha_{\mathrm{b,o}}$ is

$$\partial_{\alpha_{\mathrm{b,o}}} \|\hat{\boldsymbol{T}}_{\omega\mathrm{n,DC}}\|_{\mathcal{H}_2}^2 = \frac{\kappa_\omega^2 \alpha_{\mathrm{b,o}}^2 + 2\kappa_\omega^2 \alpha_{\mathrm{l,o}} \alpha_{\mathrm{b,o}} - \kappa_{\mathrm{p}}^2}{2m_{\mathrm{o}}\check{\alpha}_{\mathrm{o}}^2} \sum_{i=1}^{n} \frac{1}{r_i}\,. \tag{4.15}$$

By equating (4.15) to 0, we can solve for the corresponding $\alpha_{\mathrm{b,o}}$ as $\alpha^{\star}_{\mathrm{b,o}_{\pm}} = -\alpha_{\mathrm{l,o}} \pm \sqrt{\alpha^2_{\mathrm{l,o}} + (\kappa_{\mathrm{p}}/\kappa_{\omega})^2}$. The only positive root is therefore $\alpha^{\star}_{\mathrm{b,o}} := -\alpha_{\mathrm{l,o}} + \sqrt{\alpha^2_{\mathrm{l,o}} + (\kappa_{\mathrm{p}}/\kappa_{\omega})^2}$. Clearly, $\sum_{i=1}^{n}(1/r_i) > 0$ since $r_i > 0$, $\forall i \in [n]$. Thus, we only need to focus on the polynomial in $\alpha_{\mathrm{b,o}}$ in (4.15). Since the denominator of that polynomial is always positive and the highest order coefficient of the numerator is positive, whenever $0 < \alpha_{\mathrm{b,o}} < \alpha^{\star}_{\mathrm{b,o}}$, then $\partial_{\alpha_{\mathrm{b,o}}} \|\hat{\boldsymbol{T}}_{\omega\mathrm{n,DC}}\|^2_{\mathcal{H}_2} < 0$, and, if $\alpha_{\mathrm{b,o}} > \alpha^{\star}_{\mathrm{b,o}}$, then $\partial_{\alpha_{\mathrm{b,o}}} \|\hat{\boldsymbol{T}}_{\omega\mathrm{n,DC}}\|^2_{\mathcal{H}_2} > 0$. Therefore, $\alpha^{\star}_{\mathrm{b,o}}$ is the minimizer of $\|\hat{\boldsymbol{T}}_{\omega\mathrm{n,DC}}\|^2_{\mathcal{H}_2}$. □

Two main observations can be made from Corollaries 4.5 and 4.6. First, the control parameter $\alpha_{\mathrm{b,o}}$ of DC has a direct effect on the size of the frequency variance. Particularly, by tuning $\alpha_{\mathrm{b,o}} = \alpha^{\star}_{\mathrm{b,o}}$, we can minimize the frequency variance. The other important point is that VI will induce unbounded frequency variance, which poses a threat to the operation of the power system.

Steady-State Effort Share

The corollary below gives the expression for the steady-state effort share of inverter-interfaced energy storage when the control law DC or VI is employed.

Corollary 4.7 (Steady-State Effort Share of DC and VI). *Let Assumptions 2.2 and 3.2 hold. If $p_{\mathrm{b},i}$ is defined by the control law DC in (4.1) or VI in (4.2), $\forall i \in [n]$, then the steady-state effort share of of the respective system $\hat{\boldsymbol{T}}_{\omega\mathrm{p,DC}}(s)$ or $\hat{\boldsymbol{T}}_{\omega\mathrm{p,VI}}(s)$ is given by*

$$\eta_{\mathrm{es}} = \frac{\sum_{i=1}^{n} \alpha_{\mathrm{b},i}}{\sum_{i=1}^{n} (\alpha_{\mathrm{l},i} + \alpha_{\mathrm{t},i} + \alpha_{\mathrm{b},i})} \,. \tag{4.16}$$

Proof. The result follows directly from Theorem 3.6 if it is recognized that $\hat{c}_{\mathrm{i}}(0) = -\alpha_{\mathrm{b},i}$, $\forall i \in [n]$, for both DC and VI. □

Table 4.1: A Comparison Between Traditional Control Laws

METRICS	DROOP CONTROL	VIRTUAL INERTIA
Synchronous frequency	$\frac{\sum_{i=1}^{n} \mu_{0,i}}{\sum_{i=1}^{n} (\alpha_{l,i} + \alpha_{t,i} + \alpha_{b,i})}$	
Nadir elimination condition	$m_o \geq m_c$	$m_o + m_{v,o} \geq m_c$
	$m_c := \tau_{t,o} \left(\sqrt{\alpha_{t,o}} + \sqrt{\check{\alpha}_o + \alpha_{t,o}} \right)^2$	
RoCoF	$\frac{\lvert\sum_{i=1}^{n} \mu_{0,i}\rvert}{\sum_{i=1}^{n} r_i} \frac{1}{m_o}$	$\frac{\lvert\sum_{i=1}^{n} \mu_{0,i}\rvert}{\sum_{i=1}^{n} r_i} \frac{1}{m_o + m_{v,o}}$
Synchronization cost lower bound	$\frac{\sum_{k=1}^{n-1} \left(\tilde{\mu}_{0,k}^2 / \lambda_{k+1} \right)}{2 \max_{i \in [n]} (r_i) (\check{\alpha}_o + \alpha_{t,o})}$	
Frequency variance	$\frac{\kappa_p^2 + \kappa_\omega^2 \alpha_{b,o}^2}{2 m_o \check{\alpha}_o} \sum_{i=1}^{n} \frac{1}{r_i}$	∞
Steady-state effort share	$\frac{\sum_{i=1}^{n} \alpha_{b,i}}{\sum_{i=1}^{n} (\alpha_{l,i} + \alpha_{t,i} + \alpha_{b,i})}$	

Corollary 4.7 indicates that DC and VI have the same steady-state effort share, which increases as $\alpha_{b,i}$ increases. However, $\alpha_{b,i}$ is a parameter that also directly affects the frequency response performance of the system, which can be seen clearly from the frequency response performance analysis provided before.

4.1.2 Need for a Better Solution

Table 4.1 summarizes the performance metrics determined for DC and VI in Section 4.1.1, from which some important comments can be made.

First, DC and VI share the same synchronous frequency and steady-state effort share, of which the former gets improved but the latter gets worse as $\alpha_{b,i}$ increases. This is easy to understand since it is natural for a better steady-state

frequency performance to require a higher steady-state power output from inverter-interfaced energy storage.

Second, the (compensated) representative inertia constant $\check{m}_{\mathrm{o}}$ has to be greater than the critical value m_{c} for the purpose of Nadir elimination via DC or VI. Thus, DC alone can barely achieve the Nadir elimination for a low-inertia power system due to its inability to provide additional inertial response. As for VI, although the additional inertial response provided by it does make the Nadir elimination condition easier to meet, the resultant extremely high $\check{m}_{\mathrm{o}}$ can largely slow down the dynamics of a power system.

Third, the synchronization costs under DC and VI are bounded below by a value depending upon $\alpha_{\mathrm{b,o}}$. The fact that the lower bound of the synchronization costs under DC and VI is reduced as $\alpha_{\mathrm{b,o}}$ increases is not satisfactory, since, from the steady-state effort share point of view, a smaller $\alpha_{\mathrm{b,o}}$ is preferred. However, given a small $\alpha_{\mathrm{b,o}}$, even if the virtual inertia constant is very high, i.e., $m_{\mathrm{v,o}} \to \infty$, the synchronization cost under VI can never reach zero, not to mention the one under DC, which poses a limitation on the synchronization cost reduction.

Last but not least, caution is needed before widely using VI since it could introduce unbounded frequency variance in response to noise. As for DC, although there is a way to optimize the frequency variance by properly tuning $\alpha_{\mathrm{b,o}}$, the coupling between the values of the steady-state effort share and the frequency variance through this unique control parameter $\alpha_{\mathrm{b,o}}$ makes it impossible to require DC to bear an assigned amount of the steady-state effort share and reduce the frequency variance at the same time.

Above comments assist us to weigh up the pros and cons of DC and VI:

- DC has only one control parameter $\alpha_{b,o}$, which not only leads to an undesirable coupling between the steady-state effort share and most of the frequency response performance metrics but also prevents itself from achieving the Nadir elimination in a low-inertia power system.
- VI has one more control parameter $m_{v,o}$ besides $\alpha_{b,o}$, which provides itself the freedom to relatively improve the Nadir, RoCoF, and synchronization cost without affecting the steady-state effort share. However, this comes at the price of introducing unbounded frequency variance in response to noise. Moreover, the achievement of the Nadir elimination via VI requires sufficient large $\alpha_{b,o}$, which can slow down the dynamics of a power system a lot.

Therefore, although mimicking synchronous generator characteristics via inverter-interfaced energy storage seems to be a straightforward choice for frequency control in low-inertia power systems, there is a need for a better solution that overcomes the above mentioned performance limitations. This motivates our research on novel control laws that are able to strike a good trade-off among various performance metrics.

4.2 Dynamic Droop Control

We now show how, by moving away from the broadly proposed approach of mimicking synchronous generator response, one can overcome the weaknesses presented in Section 4.1. With this aim, we introduce an alternative

dynam-i-c Droop (iDroop) control that uses dynamic feedback to make a trade-off among the several different objectives described in Section 2.3.2. The proposed solution is described below.

Inverter Dynamics 3 (Dynamic Droop Control). *The dynamics of an inverter with iDroop is given by the transfer function*

$$\hat{c}_i(s) = -\frac{\nu_i s + \delta_i \alpha_{\mathrm{b},i}}{s + \delta_i}\,, \tag{4.17}$$

where $\delta_i > 0$ *and* $\nu_i > 0$ *are tunable parameters.*

Under Assumption 3.1, the representative inverter under iDroop in (4.17) is given by

$$\hat{c}_{\mathrm{o}}(s) = -\frac{\nu_{\mathrm{o}} s + \delta_{\mathrm{o}} \alpha_{\mathrm{b,o}}}{s + \delta_{\mathrm{o}}} \tag{4.18}$$

with $\nu_i = r_i \nu_{\mathrm{o}}$, $\alpha_{\mathrm{b},i} = r_i \alpha_{\mathrm{b,o}}$, and $\delta_i = \delta_{\mathrm{o}}$, $\forall i \in [n]$.

4.2.1 Performance Analysis

We now expose iDroop to the same performance analysis done for DC and VI in Section 4.1.1.

Synchronous Frequency

Corollary 4.8 (Synchronous Frequency via iDroop). *Let Assumptions 2.2 and 3.2 hold. If* $p_{\mathrm{b},i}$ *is defined by the control law iDroop in (4.17),* $\forall i \in [n]$*, then the steady-state frequency deviation of the system* $\hat{\boldsymbol{T}}_{\omega\mathrm{p,iDroop}}(s)$ *synchronizes to the synchronous frequency given by (4.5).*

Proof. The result follows directly from Lemma 3.2 if it is recognized that

$\hat{c}_{\mathrm{i}}(0) = -\alpha_{\mathrm{b},i}$, $\forall i \in [n]$, for iDroop. □

Corollary 4.8 shows that iDroop preserves the synchronous frequency given by DC and VI.

Nadir

We now show that, with δ_{o} and ν_{o} tuned appropriately, iDroop enables the COI frequency of the system $\hat{\boldsymbol{T}}_{\omega\mathrm{p,iDroop}}(s)$ to evolve as a first-order response to a step power imbalance, which effectively realizes the Nadir elimination. The following theorem summarizes this idea.

Theorem 4.3 (Nadir Elimination via iDroop). *Let Assumptions 2.2, 3.1, and 3.2 hold. By setting $\delta_{\mathrm{o}} = 1/\tau_{\mathrm{t,o}}$ and $\nu_{\mathrm{o}} = \alpha_{\mathrm{b,o}} + \alpha_{\mathrm{t,o}}$, the Nadir elimination of the COI frequency of the system $\hat{\boldsymbol{T}}_{\omega\mathrm{p,iDroop}}(s)$ is achieved.*

Proof. From (3.16), we know that the COI frequency deviation of the system $\hat{\boldsymbol{T}}_{\omega\mathrm{p,iDroop}}(s)$ is given by

$$\bar{\omega}_{\mathrm{iDroop}}(t) = \frac{\sum_{i=1}^{n} \mu_{0,i}}{\sum_{i=1}^{n} r_i} h_{\mathrm{u,1,iDroop}}(t) \ , \tag{4.19}$$

where $h_{\mathrm{u,1,iDroop}}(t)$ is the unit-step response of $\hat{h}_{\mathrm{p,1,iDroop}}(s)$. If we set $\delta_{\mathrm{o}} = 1/\tau_{\mathrm{t,o}}$ and $\nu_{\mathrm{o}} = \alpha_{\mathrm{b,o}} + \alpha_{\mathrm{t,o}}$, then (4.18) can be rewritten as

$$\hat{c}_{\mathrm{o}}(s) = \frac{\alpha_{\mathrm{t,o}}}{\tau_{\mathrm{t,o}} s + 1} - (\alpha_{\mathrm{b,o}} + \alpha_{\mathrm{t,o}}) \ . \tag{4.20}$$

Applying (3.2) and (4.20) to (3.10) yields

$$\hat{h}_{\mathrm{p,1,iDroop}}(s) = \frac{1}{m_{\mathrm{o}} s + \check{\alpha}_{\mathrm{o}} + \alpha_{\mathrm{t,o}}} \ ,$$

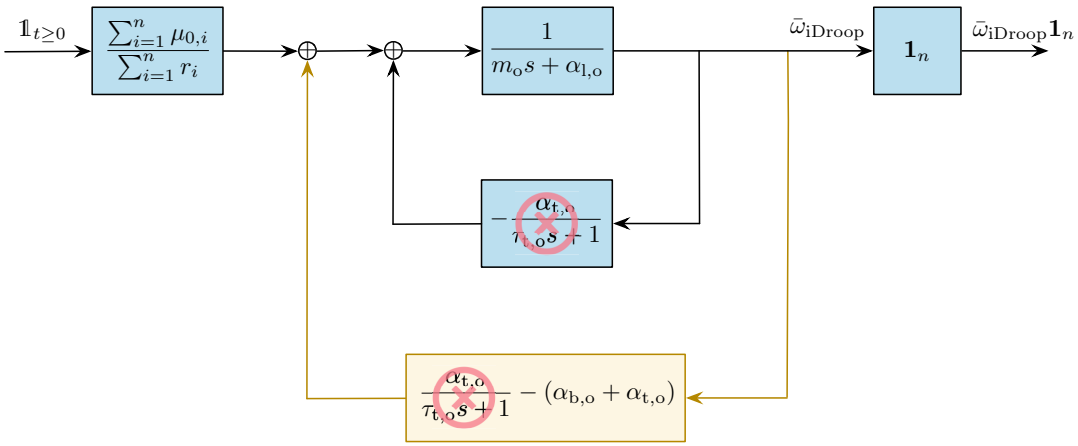

Figure 4.2: Block diagram for the main mode under iDroop with the Nadir elimination tuning

whose unit-step response $h_{\mathrm{u},1,\mathrm{iDroop}}(t)$ must be a first-order evolution. Thus, (4.19) indicates that $\bar{\omega}_{\mathrm{iDroop}}(t)$ is also a first-order evolution, which naturally achieves the Nadir elimination. □

Remark 4.3 (Intuition Behind the Nadir Elimination via iDroop). *The intuition behind the Nadir elimination tuning of iDroop is the following. Observe that* (4.20) *is composed of a lag element and a proportional element, where the former is used to cancel out the turbine-governor dynamics in the representative generator and the latter is used to improve the synchronous frequency, as illustrated in Figure* 4.2*. This makes the main mode of the system the one effectively first-order with a specified synchronous frequency.*

RoCoF

Corollary 4.9 (RoCoF under iDroop). *Let Assumptions* 2.2*,* 3.1*, and* 3.2 *hold. Then the (maximum) RoCoF of the COI frequency of the systems* $\hat{\boldsymbol{T}}_{\omega\mathrm{p,iDroop}}(s)$ *is*

bounded below as follows:

$$\|\dot{\bar{\omega}}_{\text{iDroop}}\|_{\mathcal{L}_\infty} \geq \left|\dot{\bar{\omega}}_{\text{iDroop}}(0)\right| = \frac{\left|\sum_{i=1}^{n} \mu_{0,i}\right|}{\sum_{i=1}^{n} r_i} \frac{1}{m_{\text{o}}} .$$

Proof. From the proof of Theorem 4.3, we know that

$$\hat{\bar{\omega}}_{\text{iDroop}}(s) = \frac{\sum_{i=1}^{n} \mu_{0,i}}{\sum_{i=1}^{n} r_i} \frac{\hat{h}_{\text{p,1,iDroop}}(s)}{s} . \tag{4.21}$$

Applying (3.2) and (4.18) to (3.10) yields

$$\hat{h}_{\text{p,1,iDroop}}(s) \tag{4.22}$$

$$= \frac{(\tau_{\text{t,o}} s + 1)(s + \delta_{\text{o}})}{\left[m_{\text{o}} \tau_{\text{t,o}} s^2 + (m_{\text{o}} + \alpha_{\text{l,o}} \tau_{\text{t,o}}) s + \alpha_{\text{l,o}} + \alpha_{\text{t,o}}\right](s + \delta_{\text{o}}) + (\tau_{\text{t,o}} s + 1)(\nu_{\text{o}} s + \delta_{\text{o}} \alpha_{\text{b,o}})} .$$

Thus, $\bar{\omega}_{\text{iDroop}}(t)$ is equivalent to the unit-step response of the third-order system $\hat{h}_{\text{p,1,iDroop}}(s)$ in (4.22) scaled by $(\sum_{i=1}^{n} \mu_{0,i})/(\sum_{i=1}^{n} r_i)$. It is in general tough to analyze the (maximum) RoCoF of a third-order system. However, we can bound it from below by $\left|\dot{\bar{\omega}}_{\text{iDroop}}(0)\right|$, a value can be easily found. Thus, applying the initial value theorem to (4.21) with $\hat{h}_{\text{p,1,T,iDroop}}(s)$ given by (4.22), we get

$$\dot{\bar{\omega}}_{\text{iDroop}}(0) = \lim_{s \to \infty} s^2 \hat{\bar{\omega}}_{\text{iDroop}}(s) = \lim_{s \to \infty} \frac{\sum_{i=1}^{n} \mu_{0,i}}{\sum_{i=1}^{n} r_i} \frac{s^2 \hat{h}_{\text{p,1,iDroop}}(s)}{s} = \frac{\sum_{i=1}^{n} \mu_{0,i}}{\sum_{i=1}^{n} r_i} \frac{1}{m_{\text{o}}} ,$$

which concludes the proof. □

Corollary 4.9 reflects the shortcoming of iDroop. That is, iDroop cannot reduce the RoCoF below the RoCoF of the original system without additional control from inverter-interfaced energy storage.

Synchronization Cost

Theorem 3.4 implies that the bounds on the synchronization cost of the system $\hat{\boldsymbol{T}}_{\omega\mathrm{p,iDroop}}(s)$ are closely related to $\|\hat{h}_{\mathrm{u},k+1,\mathrm{iDroop}}\|_{\mathcal{H}_2}^2$. If we can find a tuning that forces $\|\hat{h}_{\mathrm{u},k+1,\mathrm{iDroop}}\|_{\mathcal{H}_2}^2$ to be zero, $\forall k \in [n-1]$, then both the lower and upper bounds on the synchronization cost under iDroop converge to zero. Then, the zero synchronization cost is achieved naturally. The next theorem addresses this problem.

Theorem 4.4 (Zero Synchronization Cost Tuning of iDroop). *Let Assumptions 2.2, 3.1, and 3.2 hold. By setting $\delta_{\mathrm{o}} \to 0$ and $\nu_{\mathrm{o}} \to \infty$, a zero synchronization cost of the system $\hat{\boldsymbol{T}}_{\omega\mathrm{p,iDroop}}(s)$, i.e., $\|\tilde{\boldsymbol{\omega}}_{\mathrm{iDroop}}\|_{\mathcal{L}_2}^2 = 0$, can be achieved.*

Proof. Since the key is to show that, $\forall k \in [n-1]$, $\|\hat{h}_{\mathrm{u},k+1,\mathrm{iDroop}}\|_{\mathcal{H}_2}^2 \to 0$ as $\delta_{\mathrm{o}} \to 0$ and $\nu_{\mathrm{o}} \to \infty$, we can use Lemma 3.5. Applying (3.2) and (4.18) to (3.10) shows that $\hat{h}_{\mathrm{u},k+1,\mathrm{iDroop}}(s) = \hat{h}_{\mathrm{p},k+1,\mathrm{iDroop}}(s)/s$ is a transfer function in the form of (3.36) with

$$a_0 = \frac{\lambda_{k+1}\delta_{\mathrm{o}}}{m_{\mathrm{o}}\tau_{\mathrm{t,o}}}\,, \qquad a_1 = \frac{\delta_{\mathrm{o}}\left(\check{\alpha}_{\mathrm{o}} + \alpha_{\mathrm{t,o}} + \lambda_{k+1}\tau_{\mathrm{t,o}}\right) + \lambda_{k+1}}{m_{\mathrm{o}}\tau_{\mathrm{t,o}}}\,,$$

$$a_2 = \frac{\delta_{\mathrm{o}}\left(m_{\mathrm{o}} + \check{\alpha}_{\mathrm{o}}\tau_{\mathrm{t,o}}\right) + \alpha_{\mathrm{l,o}} + \alpha_{\mathrm{t,o}} + \lambda_{k+1}\tau_{\mathrm{t,o}} + \nu_{\mathrm{o}}}{m_{\mathrm{o}}\tau_{\mathrm{t,o}}}\,, \quad a_3 = \delta_{\mathrm{o}} + \frac{1}{\tau_{\mathrm{t,o}}} + \frac{\alpha_{\mathrm{l,o}} + \nu_{\mathrm{o}}}{m_{\mathrm{o}}}\,,$$

$$b_0 = \frac{\delta_{\mathrm{o}}}{m_{\mathrm{o}}\tau_{\mathrm{t,o}}}\,, \qquad b_1 = \frac{\delta_{\mathrm{o}}\tau_{\mathrm{t,o}} + 1}{m_{\mathrm{o}}\tau_{\mathrm{t,o}}}\,, \qquad b_2 = \frac{1}{m_{\mathrm{o}}}\,, \qquad b_3 = 0\,, \qquad b_4 = 0\,.$$

Considering that $a_0 \to 0$ and $b_0 \to 0$ as $\delta_{\mathrm{o}} \to 0$ and $\nu_{\mathrm{o}} \to \infty$, we can employ the $\mathcal{H}_2$ norm computation formula for the third-order transfer function in

Remark 3.5. Then

$$\lim_{\delta_o \to 0, \nu_o \to \infty} \|\hat{h}_{u,k+1,\text{iDroop}}\|_{\mathcal{H}_2}^2$$

$$= \lim_{\delta_o \to 0, \nu_o \to \infty} \frac{a_3 b_1^2 + a_1 b_2^2}{2a_1 (a_2 a_3 - a_1)}$$

$$= \lim_{\delta_o \to 0, \nu_o \to \infty} \frac{(\nu_o / m_o) [1/ (m_o \tau_{t,o})]^2 + [\lambda_{k+1}/ (m_o \tau_{t,o})] (1/m_o)^2}{2 [\lambda_{k+1}/ (m_o \tau_{t,o})] \{[\nu_o/ (m_o \tau_{t,o})] (\nu_o/m_o) - [\lambda_{k+1}/ (m_o \tau_{t,o})]\}} = 0 .$$

Thus, by Theorem 3.4, we have

$$\underline{\|\tilde{\omega}_{\text{iDroop}}\|_{\mathcal{L}_2}^2} = \overline{\|\tilde{\omega}_{\text{iDroop}}\|_{\mathcal{L}_2}^2} = 0 ,$$

which forces $\|\tilde{\omega}_{\text{iDroop}}\|_{\mathcal{L}_2}^2 = 0$. □

Theorem 4.4 shows that, unlike DC and VI that require changes on $\alpha_{b,o}$ to arbitrarily reduce the synchronization cost, iDroop can achieve zero synchronization cost without affecting the steady-state effort share. Naturally, $\delta_o \approx 0$ may lead to slow response and $\nu_o \to \infty$ may hinder robustness. Thus this result should be appreciated from the viewpoint of the additional tuning flexibility that iDroop provides.

Frequency Variance

The following theorem quantifies the squared $\mathcal{H}_2$ norm of the system $\hat{\boldsymbol{T}}_{\omega n,\text{iDroop}}(s)$, which corresponds to the frequency variance in response to stochastic power fluctuations and frequency measurement noise under iDroop.

Corollary 4.10 (Frequency Variance under iDroop). *Let Assumptions 2.2, 3.1,*

and 3.3 hold. The squared $\mathcal{H}_2$ norm of the system $\hat{\boldsymbol{T}}_{\omega\text{n,iDroop}}(s)$ is given by

$$\|\hat{\boldsymbol{T}}_{\omega\text{n,iDroop}}\|_{\mathcal{H}_2}^2 = \frac{\left(\kappa_{\text{p}}^2+\kappa_\omega^2\alpha_{\text{b,o}}^2\right)m_{\text{o}}\delta_{\text{o}}^2+\left(\kappa_{\text{p}}^2+\kappa_\omega^2\nu_{\text{o}}^2\right)\left(\breve{\alpha}_{\text{o}}\delta_{\text{o}}+\lambda_k\right)}{2m_{\text{o}}\left[\breve{\alpha}_{\text{o}}m_{\text{o}}\delta_{\text{o}}^2+\left(\alpha_{\text{l,o}}+\nu_{\text{o}}\right)\left(\breve{\alpha}_{\text{o}}\delta_{\text{o}}+\lambda_k\right)\right]}\sum_{i=1}^{n}\frac{1}{r_i}\,. \quad (4.23)$$

Proof. The proof is based on the Theorem 3.5 and Lemma 3.5. Applying (3.1) and (4.18) to (3.10) and (3.11) shows that, after being written in the form of (3.36), $\hat{h}_{\text{p},k,\text{iDroop}}(s)$ is a transfer function with $b_4 = a_0 = b_0 = 0$, $a_1 = \left(\lambda_k\delta_{\text{o}}\right)/m_{\text{o}}$, $b_1 = 0$, $a_2 = \left(\breve{\alpha}_{\text{o}}\delta_{\text{o}}+\lambda_k\right)/m_{\text{o}}$, $b_2 = \delta_{\text{o}}/m_{\text{o}}$, $a_3 = \left(m_{\text{o}}\delta_{\text{o}}+\alpha_{\text{l,o}}+\nu_{\text{o}}\right)/m_{\text{o}}$, $b_3 = 1/m_{\text{o}}$, while $\hat{h}_{\omega,k,\text{iDroop}}(s)$ is a transfer function with $b_4 = a_0 = b_0 = 0$, $a_1 = \left(\lambda_k\delta_{\text{o}}\right)/m_{\text{o}}$, $b_1 = 0$, $a_2 = \left(\breve{\alpha}_{\text{o}}\delta_{\text{o}}+\lambda_k\right)/m_{\text{o}}$, $b_2 = -\left(\alpha_{\text{b,o}}\delta_{\text{o}}\right)/m_{\text{o}}$, $a_3 = \left(m_{\text{o}}\delta_{\text{o}}+\alpha_{\text{l,o}}+\nu_{\text{o}}\right)/m_{\text{o}}$, $b_3 = -\nu_{\text{o}}/m_{\text{o}}$. Thus, by Lemma 3.5, $\forall k\in[n]$,

$$\|\hat{h}_{\text{p},k,\text{iDroop}}\|_{\mathcal{H}_2}^2 = \frac{m_{\text{o}}\delta_{\text{o}}^2+\breve{\alpha}_{\text{o}}\delta_{\text{o}}+\lambda_k}{2m_{\text{o}}\left[\breve{\alpha}_{\text{o}}m_{\text{o}}\delta_{\text{o}}^2+\left(\alpha_{\text{l,o}}+\nu_{\text{o}}\right)\left(\breve{\alpha}_{\text{o}}\delta_{\text{o}}+\lambda_k\right)\right]}\,,$$

$$\|\hat{h}_{\omega,k,\text{iDroop}}\|_{\mathcal{H}_2}^2 = \frac{\alpha_{\text{b,o}}^2m_{\text{o}}\delta_{\text{o}}^2+\nu_{\text{o}}^2\left(\breve{\alpha}_{\text{o}}\delta_{\text{o}}+\lambda_k\right)}{2m_{\text{o}}\left[\breve{\alpha}_{\text{o}}m_{\text{o}}\delta_{\text{o}}^2+\left(\alpha_{\text{l,o}}+\nu_{\text{o}}\right)\left(\breve{\alpha}_{\text{o}}\delta_{\text{o}}+\lambda_k\right)\right]}\,.$$

Then it follows from Theorem 3.5 that

$$\begin{aligned}\|\hat{\boldsymbol{T}}_{\omega\text{n,iDroop}}\|_{\mathcal{H}_2}^2 &= \sum_{k=1}^{n}\Gamma_{kk}\frac{\left(\kappa_{\text{p}}^2+\kappa_\omega^2\alpha_{\text{b,o}}^2\right)m_{\text{o}}\delta_{\text{o}}^2+\left(\kappa_{\text{p}}^2+\kappa_\omega^2\nu_{\text{o}}^2\right)\left(\breve{\alpha}_{\text{o}}\delta_{\text{o}}+\lambda_k\right)}{2m_{\text{o}}\left[\breve{\alpha}_{\text{o}}m_{\text{o}}\delta_{\text{o}}^2+\left(\alpha_{\text{l,o}}+\nu_{\text{o}}\right)\left(\breve{\alpha}_{\text{o}}\delta_{\text{o}}+\lambda_k\right)\right]}\\ &= \frac{\left(\kappa_{\text{p}}^2+\kappa_\omega^2\alpha_{\text{b,o}}^2\right)m_{\text{o}}\delta_{\text{o}}^2+\left(\kappa_{\text{p}}^2+\kappa_\omega^2\nu_{\text{o}}^2\right)\left(\breve{\alpha}_{\text{o}}\delta_{\text{o}}+\lambda_k\right)}{2m_{\text{o}}\left[\breve{\alpha}_{\text{o}}m_{\text{o}}\delta_{\text{o}}^2+\left(\alpha_{\text{l,o}}+\nu_{\text{o}}\right)\left(\breve{\alpha}_{\text{o}}\delta_{\text{o}}+\lambda_k\right)\right]}\sum_{k=1}^{n}\Gamma_{kk}\,.\end{aligned}$$

Recall that in the proof of Corollary 4.5, we have shown that $\sum_{k=1}^{n}\Gamma_{kk} = \sum_{i=1}^{n}\left(1/r_i\right)$, which concludes the proof of (4.23). □

The explicit expression of $\|\hat{\boldsymbol{T}}_{\omega\mathrm{n,iDroop}}\|_{\mathcal{H}_2}^2$ given in Corollary 4.10 is useful to show that iDroop can reduce the frequency variance relative to DC and VI. Given the fact that $\|\hat{\boldsymbol{T}}_{\omega\mathrm{n,VI}}\|_{\mathcal{H}_2}^2$ is infinite, the question indeed lies in whether we can find a set of values for parameters δ_o and ν_o that ensure $\|\hat{\boldsymbol{T}}_{\omega\mathrm{n,iDroop}}\|_{\mathcal{H}_2}^2 \leq \|\hat{\boldsymbol{T}}_{\omega\mathrm{n,DC}}\|_{\mathcal{H}_2}^2$. Fortunately, we can not only find such a set but also the optimal setting for (4.23). The following three lemmas set the foundation of this important result which is given as Theorem 4.5.

Lemma 4.1 (Limit of $\|\hat{\boldsymbol{T}}_{\omega\mathrm{n,iDroop}}\|_{\mathcal{H}_2}^2$). *Let Assumptions 2.2, 3.1, and 3.3 hold. If $\delta_\mathrm{o} \to \infty$, then $\|\hat{\boldsymbol{T}}_{\omega\mathrm{n,iDroop}}\|_{\mathcal{H}_2}^2 = \|\hat{\boldsymbol{T}}_{\omega\mathrm{n,DC}}\|_{\mathcal{H}_2}^2$.*

Proof. The limit of (4.23) as $\delta_\mathrm{o} \to \infty$ can be computed as

$$\lim_{\delta_\mathrm{o}\to\infty} \|\hat{\boldsymbol{T}}_{\omega\mathrm{n,iDroop}}\|_{\mathcal{H}_2}^2 = \frac{\kappa_\mathrm{p}^2 + \kappa_\omega^2\alpha_{\mathrm{b,o}}^2}{2m_\mathrm{o}\check{\alpha}_\mathrm{o}} \sum_{i=1}^{n} \frac{1}{r_i} = \|\hat{\boldsymbol{T}}_{\omega\mathrm{n,DC}}\|_{\mathcal{H}_2}^2,$$

where the second equality follows from (4.11a). □

Lemma 4.1 shows that $\|\hat{\boldsymbol{T}}_{\omega\mathrm{n,iDroop}}\|_{\mathcal{H}_2}^2$ converges to $\|\hat{\boldsymbol{T}}_{\omega\mathrm{n,DC}}\|_{\mathcal{H}_2}^2$ as $\delta_\mathrm{o} \to \infty$. The next lemma shows that this convergence is monotonically from either above or below depending on the value of the parameter ν_o.

Lemma 4.2 (ν_o-Dependent Monotonicity of $\|\hat{\boldsymbol{T}}_{\omega\mathrm{n,iDroop}}\|_{\mathcal{H}_2}^2$ in Regard to δ_o). *Let Assumptions 2.2, 3.1, and 3.3 hold. Define*

$$\sigma_1(\nu_\mathrm{o}) := \frac{-\check{\alpha}_\mathrm{o}\kappa_\omega^2\nu_\mathrm{o}^2 + \left(\kappa_\mathrm{p}^2 + \kappa_\omega^2\alpha_{\mathrm{b,o}}^2\right)\nu_\mathrm{o} + \alpha_{\mathrm{l,o}}\alpha_{\mathrm{b,o}}^2\kappa_\omega^2 - \alpha_{\mathrm{b,o}}\kappa_\mathrm{p}^2}{\alpha_{\mathrm{l,o}} + \nu_\mathrm{o}}.$$

Then

- *$\|\hat{\boldsymbol{T}}_{\omega\mathrm{n,iDroop}}\|_{\mathcal{H}_2}^2$ is a monotonically increasing or decreasing function of $\delta_\mathrm{o} > 0$ if and only if $\sigma_1(\nu_\mathrm{o})$ is positive or negative, respectively.*

- $\|\hat{\boldsymbol{T}}_{\omega\text{n,iDroop}}\|_{\mathcal{H}_2}^2$ *is independent of* $\delta_\text{o} > 0$ *if and only if* $\sigma_1(\nu_\text{o})$ *is zero.*

Proof. Provided that $\|\hat{\boldsymbol{T}}_{\omega\text{n,iDroop}}\|_{\mathcal{H}_2}^2$ is a function of δ_o and ν_o, in what follows we denote it by $\Pi(\delta_\text{o}, \nu_\text{o})$. To make it clear how $\Pi(\delta_\text{o}, \nu_\text{o})$ changes with δ_o, we firstly put it into the equivalent form of

$$\Pi(\delta_\text{o}, \nu_\text{o}) = \left[\frac{\sigma_1(\nu_\text{o})\delta_\text{o}^2}{\sigma_2\delta_\text{o}^2 + \sigma_3(\nu_\text{o})\delta_\text{o} + \sigma_4(\nu_\text{o}, \lambda_k)} + \sigma_5(\nu_\text{o})\right] \sum_{i=1}^{n} \frac{1}{r_i}$$

with

$$\sigma_1(\nu_\text{o}) := \frac{-\check{\alpha}_\text{o}\kappa_\omega^2\nu_\text{o}^2 + \left(\kappa_\text{p}^2 + \kappa_\omega^2\alpha_{\text{b,o}}^2\right)\nu_\text{o} + \alpha_{\text{l,o}}\alpha_{\text{b,o}}^2\kappa_\omega^2 - \alpha_{\text{b,o}}\kappa_\text{p}^2}{\alpha_{\text{l,o}} + \nu_\text{o}} ,$$

$$\sigma_2 := 2m_\text{o}\check{\alpha}_\text{o} , \qquad \sigma_3(\nu_\text{o}) := 2\left(\alpha_{\text{l,o}} + \nu_\text{o}\right)\check{\alpha}_\text{o} ,$$

$$\sigma_4(\nu_\text{o}, \lambda_k) := 2\left(\alpha_{\text{l,o}} + \nu_\text{o}\right)\lambda_k , \qquad \sigma_5(\nu_\text{o}) := \frac{\kappa_\text{p}^2 + \kappa_\omega^2\nu_\text{o}^2}{2m_\text{o}\left(\alpha_{\text{l,o}} + \nu_\text{o}\right)} .$$

We then take the partial derivative of $\Pi(\delta_\text{o}, \nu_\text{o})$ with respect to δ_o as

$$\partial_{\delta_\text{o}}\Pi(\delta_\text{o}, \nu_\text{o}) = \sigma_1(\nu_\text{o}) \left[\frac{\sigma_3(\nu_\text{o})\delta_\text{o}^2 + 2\sigma_4(\nu_\text{o}, \lambda_k)\delta_\text{o}}{\left(\sigma_2\delta_\text{o}^2 + \sigma_3(\nu_\text{o})\delta_\text{o} + \sigma_4(\nu_\text{o}, \lambda_k)\right)^2}\right] \sum_{i=1}^{n} \frac{1}{r_i} .$$

Since $m_\text{o} > 0$, $\alpha_{\text{l,o}} > 0$, $\nu_\text{o} > 0$, and $\alpha_{\text{b,o}} > 0$, σ_2 and $\sigma_3(\nu_\text{o})$ are positive. Also, given that all the eigenvalues of the scaled Laplacian matrix $\boldsymbol{L}_\text{R}$ are nonnegative, $\sigma_4(\nu_\text{o}, \lambda_k)$ must be nonnegative. Thus, $\forall\delta_\text{o} > 0$, $(\sigma_3(\nu_\text{o})\delta_\text{o}^2 + 2\sigma_4(\nu_\text{o}, \lambda_k)\delta_\text{o}) / \left(\sigma_2\delta_\text{o}^2 + \sigma_3(\nu_\text{o})\delta_\text{o} + \sigma_4(\nu_\text{o}, \lambda_k)\right)^2 > 0$. In addition, $r_i > 0$, $\forall i \in [n]$. Therefore, $\text{sign}\left(\partial_{\delta_\text{o}}\Pi(\delta_\text{o}, \nu_\text{o})\right) = \text{sign}\left(\sigma_1(\nu_\text{o})\right)$, $\forall\delta_\text{o} > 0$, which concludes the proof. □

By Lemma 4.2, for a given ν_o, if $\sigma_1(\nu_\text{o}) < 0$, then $\|\hat{\boldsymbol{T}}_{\omega\text{n,iDroop}}\|_{\mathcal{H}_2}^2$ always decreases as δ_o increases. However, according to Lemma 4.1, even if $\delta_\text{o} \to \infty$,

we can only obtain $\|\hat{\boldsymbol{T}}_{\omega\mathrm{n,iDroop}}\|_{\mathcal{H}_2}^2 = \|\hat{\boldsymbol{T}}_{\omega\mathrm{n,DC}}\|_{\mathcal{H}_2}^2$. Similarly, if $\sigma_1(\nu_\mathrm{o}) = 0$, then $\|\hat{\boldsymbol{T}}_{\omega\mathrm{n,iDroop}}\|_{\mathcal{H}_2}^2$ keeps constant as δ_o increases, which means that whatever δ_o is we will always obtain $\|\hat{\boldsymbol{T}}_{\omega\mathrm{n,iDroop}}\|_{\mathcal{H}_2}^2 = \|\hat{\boldsymbol{T}}_{\omega\mathrm{n,DC}}\|_{\mathcal{H}_2}^2$. Therefore, iDroop cannot outperform DC when $\sigma_1(\nu_\mathrm{o}) \leq 0$. To put it another way, Lemmas 4.1 and 4.2 imply that, in order to improve the frequency variance through iDroop, one needs to set ν_o such that $\sigma_1(\nu_\mathrm{o}) > 0$ and δ_o as small as practically possible. The following lemma characterizes the minimizer $\nu_\mathrm{o}^\star$ of $\|\hat{\boldsymbol{T}}_{\omega\mathrm{n,iDroop}}\|_{\mathcal{H}_2}^2$ when $\delta_\mathrm{o} = 0$.

Lemma 4.3 (Minimizer $\nu_\mathrm{o}^\star$ of $\|\hat{\boldsymbol{T}}_{\omega\mathrm{n,iDroop}}\|_{\mathcal{H}_2}^2$ for $\delta_\mathrm{o} = 0$). *Let Assumptions 2.2, 3.1, and 3.3 hold. Then*

$$\nu_\mathrm{o}^\star := \operatorname*{argmin}_{\delta_\mathrm{o}=0,\nu_\mathrm{o}>0} \|\hat{\boldsymbol{T}}_{\omega\mathrm{n,iDroop}}\|_{\mathcal{H}_2}^2 = -\alpha_{\mathrm{l,o}} + \sqrt{\alpha_{\mathrm{l,o}}^2 + \left(\frac{\kappa_\mathrm{p}}{\kappa_\omega}\right)^2}. \tag{4.24}$$

Proof. Recall from the proof of Lemma 4.2 that $\|\hat{\boldsymbol{T}}_{\omega\mathrm{n,iDroop}}\|_{\mathcal{H}_2}^2 = \Pi(\delta_\mathrm{o}, \nu_\mathrm{o})$. Then we have

$$\Pi(0, \nu_\mathrm{o}) = \sigma_5(\nu_\mathrm{o}) \sum_{i=1}^{n} \frac{1}{r_i} = \frac{\kappa_\mathrm{p}^2 + \kappa_\omega^2 \nu_\mathrm{o}^2}{2m_\mathrm{o}\left(\alpha_{\mathrm{l,o}} + \nu_\mathrm{o}\right)} \sum_{i=1}^{n} \frac{1}{r_i},$$

whose derivative with respect to ν_o is given by

$$\frac{\mathrm{d}\Pi(0, \nu_\mathrm{o})}{\mathrm{d}\nu_\mathrm{o}} = \frac{\kappa_\omega^2 \nu_\mathrm{o}^2 + 2\kappa_\omega^2 \alpha_{\mathrm{l,o}} \nu_\mathrm{o} - \kappa_\mathrm{p}^2}{2m_\mathrm{o}\left(\alpha_{\mathrm{l,o}} + \nu_\mathrm{o}\right)^2} \sum_{i=1}^{n} \frac{1}{r_i}. \tag{4.25}$$

Note that (4.25) and (4.15) are in the same form. Thus, $\nu_\mathrm{o}^\star$ is determined in the same way as in the proof of Corollary 4.6. □

We are now ready to prove the next theorem.

Theorem 4.5 ($\|\hat{\boldsymbol{T}}_{\omega\mathrm{n,iDroop}}\|_{\mathcal{H}_2}^2$ Optimal Tuning). *Let Assumptions 2.2, 3.1, and*

3.3 hold. Define $\nu_{\mathrm{o}}^{\star}$ as in (4.24).

- *Whenever $(\kappa_{\mathrm{p}}/\kappa_{\omega})^2 \neq 2\alpha_{\mathrm{b,o}}\alpha_{\mathrm{l,o}} + \alpha_{\mathrm{b,o}}^2$, $\forall\, \delta_{\mathrm{o}} > 0$ and ν_{o} such that*

$$\nu_{\mathrm{o}} \in [\nu_{\mathrm{o}}^{\star}, \alpha_{\mathrm{b,o}}) \qquad \textit{or} \qquad \nu_{\mathrm{o}} \in (\alpha_{\mathrm{b,o}}, \nu_{\mathrm{o}}^{\star}] \,, \tag{4.26}$$

  iDroop outperforms DC in terms of frequency variance, i.e.,

$$\|\hat{\boldsymbol{T}}_{\omega\mathrm{n,iDroop}}\|_{\mathcal{H}_2}^2 < \|\hat{\boldsymbol{T}}_{\omega\mathrm{n,DC}}\|_{\mathcal{H}_2}^2 \,.$$

  Moreover, the global minimum of $\|\hat{\boldsymbol{T}}_{\omega\mathrm{n,iDroop}}\|_{\mathcal{H}_2}^2$ is obtained by setting $\delta_{\mathrm{o}} \to 0$ and $\nu_{\mathrm{o}} \to \nu_{\mathrm{o}}^{\star}$.

- *If $(\kappa_{\mathrm{p}}/\kappa_{\omega})^2 = 2\alpha_{\mathrm{b,o}}\alpha_{\mathrm{l,o}} + \alpha_{\mathrm{b,o}}^2$, then, $\forall \delta_{\mathrm{o}} > 0$, by setting $\nu_{\mathrm{o}} \to \nu_{\mathrm{o}}^{\star} = \alpha_{\mathrm{b,o}}$, iDroop matches DC in terms of frequency variance, i.e.,*

$$\|\hat{\boldsymbol{T}}_{\omega\mathrm{n,iDroop}}\|_{\mathcal{H}_2}^2 = \|\hat{\boldsymbol{T}}_{\omega\mathrm{n,DC}}\|_{\mathcal{H}_2}^2 \,.$$

Proof. As discussed before, to guarantee $\|\hat{\boldsymbol{T}}_{\omega\mathrm{n,iDroop}}\|_{\mathcal{H}_2}^2 < \|\hat{\boldsymbol{T}}_{\omega\mathrm{n,DC}}\|_{\mathcal{H}_2}^2$, one needs to set ν_{o} to such that $\sigma_1(\nu_{\mathrm{o}}) > 0$. In this case, $\|\hat{\boldsymbol{T}}_{\omega\mathrm{n,iDroop}}\|_{\mathcal{H}_2}^2$ always increases as δ_{o} increases, so choosing δ_{o} arbitrarily small is optimal for any fixed ν_{o}.

We now look for the values of ν_{o} that satisfy the requirement $\sigma_1(\nu_{\mathrm{o}}) > 0$. Since the denominator of $\sigma_1(\nu_{\mathrm{o}})$ is always positive, the sign of $\sigma_1(\nu_{\mathrm{o}})$ only depends on its numerator. Denote the numerator of $\sigma_1(\nu_{\mathrm{o}})$ as $N_{\sigma_1}(\nu_{\mathrm{o}})$. Clearly, $N_{\sigma_1}(\nu_{\mathrm{o}})$ is a univariate quadratic function in ν_{o}, whose roots can be calculated

as:

$$\begin{aligned}\nu_{\mathrm{o}1,2} =& \frac{-\left(\kappa_{\mathrm{p}}^2+\kappa_\omega^2\alpha_{\mathrm{b,o}}^2\right) \pm \sqrt{\left(\kappa_{\mathrm{p}}^2+\kappa_\omega^2\alpha_{\mathrm{b,o}}^2\right)^2+4\check{\alpha}_{\mathrm{o}}\kappa_\omega^2\left(\alpha_{\mathrm{l,o}}\alpha_{\mathrm{b,o}}^2\kappa_\omega^2-\alpha_{\mathrm{b,o}}\kappa_{\mathrm{p}}^2\right)}}{-2\check{\alpha}_{\mathrm{o}}\kappa_\omega^2} \\ =& \frac{\kappa_{\mathrm{p}}^2+\kappa_\omega^2\alpha_{\mathrm{b,o}}^2 \mp \sqrt{\kappa_{\mathrm{p}}^4-2\kappa_{\mathrm{p}}^2\kappa_\omega^2\alpha_{\mathrm{b,o}}\left(\alpha_{\mathrm{b,o}}+2\alpha_{\mathrm{l,o}}\right)+\kappa_\omega^4\alpha_{\mathrm{b,o}}^2\left(\alpha_{\mathrm{b,o}}+2\alpha_{\mathrm{l,o}}\right)^2}}{2\check{\alpha}_{\mathrm{o}}\kappa_\omega^2} \\ =& \frac{\kappa_{\mathrm{p}}^2+\kappa_\omega^2\alpha_{\mathrm{b,o}}^2 \mp \left[\kappa_{\mathrm{p}}^2-\kappa_\omega^2\alpha_{\mathrm{b,o}}\left(\alpha_{\mathrm{b,o}}+2\alpha_{\mathrm{l,o}}\right)\right]}{2\check{\alpha}_{\mathrm{o}}\kappa_\omega^2}\,.\end{aligned}$$

They can be further simplified to

$$\nu_{\mathrm{o}1}=\alpha_{\mathrm{b,o}} \qquad \text{and} \qquad \nu_{\mathrm{o}2}=\frac{(\kappa_{\mathrm{p}}/\kappa_\omega)^2-\alpha_{\mathrm{b,o}}\alpha_{\mathrm{l,o}}}{\check{\alpha}_{\mathrm{o}}}\,.$$

Provided that the highest order coefficient of $N_{\sigma_1}(\nu_{\mathrm{o}})$ is negative, the graph of $N_{\sigma_1}(\nu_{\mathrm{o}})$ is a parabola that opens downwards. Therefore, if $\nu_{\mathrm{o}1}<\nu_{\mathrm{o}2}$, then $\nu_{\mathrm{o}}\in(\nu_{\mathrm{o}1},\nu_{\mathrm{o}2})$ guarantees $\sigma_1(\nu_{\mathrm{o}})>0$; if $\nu_{\mathrm{o}1}>\nu_{\mathrm{o}2}$, then $\nu_{\mathrm{o}}\in(\nu_{\mathrm{o}2},\nu_{\mathrm{o}1})\cap(0,\infty)$ guarantees $\sigma_1(\nu_{\mathrm{o}})>0$. Notably, if $\nu_{\mathrm{o}1}=\nu_{\mathrm{o}2}$, there is no feasible point of ν_{o} to make $\sigma_1(\nu_{\mathrm{o}})>0$.

The condition $\nu_{\mathrm{o}1}=\nu_{\mathrm{o}2}$ happens only if $(\kappa_{\mathrm{p}}/\kappa_\omega)^2=2\alpha_{\mathrm{b,o}}\alpha_{\mathrm{l,o}}+\alpha_{\mathrm{b,o}}^2$, from which it follows that $\nu_{\mathrm{o}}^\star=\alpha_{\mathrm{b,o}}=\nu_{\mathrm{o}1}=\nu_{\mathrm{o}2}$. Then $\sigma_1(\nu_{\mathrm{o}}^\star)=\sigma_1(\alpha_{\mathrm{b,o}})=0$. Therefore, by setting $\nu_{\mathrm{o}}\to\nu_{\mathrm{o}}^\star=\alpha_{\mathrm{b,o}}$, we get $\|\hat{\boldsymbol{T}}_{\omega\mathrm{n,iDroop}}\|_{\mathcal{H}_2}^2=\|\hat{\boldsymbol{T}}_{\omega\mathrm{n,DC}}\|_{\mathcal{H}_2}^2$. This concludes the proof of the second part.

We now focus on the case where the set

$$\mathcal{S}:=(\nu_{\mathrm{o}1},\nu_{\mathrm{o}2})\cup\{(\nu_{\mathrm{o}2},\nu_{\mathrm{o}1})\cap(0,\infty)\}$$

is nonempty. Recall from the proof of Lemma 4.2 that $\|\hat{\boldsymbol{T}}_{\omega\mathrm{n,iDroop}}\|_{\mathcal{H}_2}=$

$\Pi(\delta_o, \nu_o)$. For any fixed $\nu_o \in \mathcal{S}$, it holds that $\sigma_1(\nu_o) > 0$ and thus $\Pi(\delta_o, \nu_o) > \Pi(0, \nu_o)$, $\forall \delta_o > 0$. Recall from the proof of Lemma 4.3 that $\nu_o^\star$ is the minimizer of $\Pi(0, \nu_o)$. Hence, $(0, \nu_o^\star)$ globally minimizes $\Pi(\delta_o, \nu_o)$ as long as $\nu_o^\star \in \mathcal{S}$. In fact, we will show next that $\nu_o^\star$ is always within $\mathcal{S}$ whenever $\mathcal{S} \neq \emptyset$.

Firstly we consider the case when $\nu_{o1} < \nu_{o2}$, which implies that $(\kappa_p/\kappa_\omega)^2 > 2\alpha_{b,o}\alpha_{l,o} + \alpha_{b,o}^2$. Then we have

$$\nu_o^\star > -\alpha_{l,o} + \sqrt{\alpha_{l,o}^2 + 2\alpha_{b,o}\alpha_{l,o} + \alpha_{b,o}^2} = -\alpha_{l,o} + (\alpha_{l,o} + \alpha_{b,o}) = \alpha_{b,o} = \nu_{o1}\,.$$

We also want to show $\nu_o^\star < \nu_{o2}$ which holds if and only if

$$\sqrt{\alpha_{l,o}^2 + \left(\frac{\kappa_p}{\kappa_\omega}\right)^2} < \frac{(\kappa_p/\kappa_\omega)^2 - \alpha_{b,o}\alpha_{l,o}}{\check{\alpha}_o} + \alpha_{l,o} = \frac{(\kappa_p/\kappa_\omega)^2 + \alpha_{l,o}^2}{\check{\alpha}_o}\,.$$

This is equivalent to

$$\check{\alpha}_o < \sqrt{\alpha_{l,o}^2 + \left(\frac{\kappa_p}{\kappa_\omega}\right)^2}\,,$$

which always holds since $(\kappa_p/\kappa_\omega)^2 > 2\alpha_{b,o}\alpha_{l,o} + \alpha_{b,o}^2$. Thus, $\nu_{o1} < \nu_o^\star < \nu_{o2}$. Similarly, we can prove that in the case when $\nu_{o1} > \nu_{o2}$, $\nu_{o2} < \nu_o^\star < \nu_{o1}$ holds and thus $\nu_o^\star \in (\nu_{o2}, \nu_{o1}) \cap (0, \infty)$.

Therefore, $(0, \nu_o^\star)$ is the global minimizer of $\Pi(\delta_o, \nu_o)$.

Finally, by Lemma 4.1, $\|\hat{\boldsymbol{T}}_{\omega n,DC}\|_{\mathcal{H}_2}^2 = \Pi(\infty, \nu_o)$. The condition (4.26) actually guarantees $\nu_o \in \mathcal{S}$ and thus $\sigma_1(\nu_o) > 0$. Then, by Lemma 4.2, we have $\|\hat{\boldsymbol{T}}_{\omega n,DC}\|_{\mathcal{H}_2}^2 = \Pi(\infty, \nu_o) > \Pi(\delta_o, \nu_o)$. This concludes the proof of the first part. □

Theorem 4.5 shows that, to optimally improve the frequency variance, iDroop needs to first set δ_o arbitrarily close to zero. Interestingly, this implies

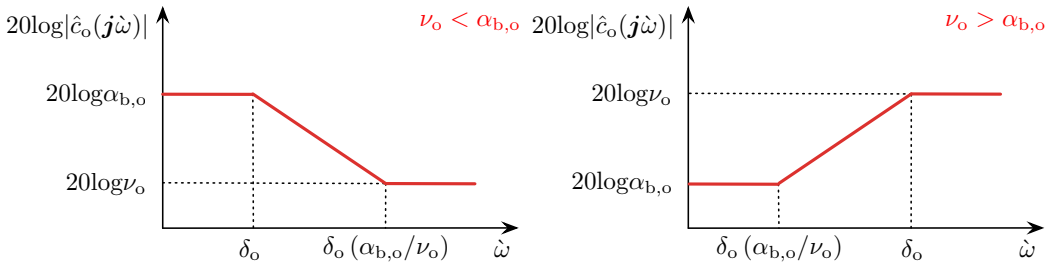

(a) As a lag compensator (b) As a lead compensator

Figure 4.3: Asymptotic approximation of Bode diagram for dynamic droop control

that the transfer function $\hat{c}_o(s) \approx -\nu_o$ except for $\hat{c}_o(0) = -\alpha_{b,o}$. In other words, iDroop uses its first-order lead/lag property to effectively decouple the dc gain $\hat{c}_o(0)$ from the gain at all the other frequencies such that $\hat{c}_o(j\dot{\omega}) \approx -\nu_o$, $\forall \dot{\omega} \neq 0$. Once we rewrite (4.18) as

$$\hat{c}_o(s) = -\nu_o \frac{s + \delta_o\,(\alpha_{b,o}/\nu_o)}{s + \delta_o},$$

this decouple is particularly easy to understand in two special regimes as illustrated in Figure 4.3: (i) If $\kappa_p \ll \kappa_\omega$, the system is dominated by frequency measurement noise and therefore, by Lemma 4.3, $\nu_o^\star \approx 0 < \alpha_{b,o}$ which makes iDroop a lag compensator. Thus, by using the low gain at high frequencies in the lag compensation (setting $\nu_o < \alpha_{b,o}$), iDroop can attenuate frequency measurement noise; (ii) If $\kappa_p \gg \kappa_\omega$, the system is dominated by stochastic power fluctuations and therefore, by Lemma 4.3, $\nu_o^\star \approx \kappa_p/\kappa_\omega > \alpha_{b,o}$ which makes iDroop a lead compensator. Thus, by using the high gain at high frequencies in the lead compensation (setting $\nu_o > \alpha_{b,o}$), iDroop can mitigate stochastic power fluctuations.

Steady-State Effort Share

The corollary below shows that iDroop is able to preserve the steady-state effort share of DC and VI.

Corollary 4.11 (Steady-State Effort Share of iDroop). *Let Assumptions 2.2 and 3.2 hold. If $p_{\mathrm{b},i}$ is defined by the control law iDroop in (4.17), $\forall i \in [n]$, then the steady-state effort share of of the system $\hat{\boldsymbol{T}}_{\omega\mathrm{p,iDroop}}(s)$ is given by (4.16).*

Proof. The result follows directly from Theorem 3.6 if it is recognized that $\hat{c}_{\mathrm{i}}(0) = -\alpha_{\mathrm{b},i}$, $\forall i \in [n]$, for iDroop. □

Corollaries 4.8 and 4.11 suggest that iDroop achieves the same steady-state behavior as DC and VI do, which depends on $\alpha_{\mathrm{b},i}$. Note that, besides $\alpha_{\mathrm{b},i}$, iDroop provides us with two more degrees of freedom by δ_i and ν_i. Thus, iDroop makes it possible to improve the dynamic frequency response performance of the system discussed above without affecting the steady-state performance.

4.2.2 Trade-Off among Performance Metrics

Table 4.2 summarizes the performance metrics determined for iDroop in Section 4.2.1, with which we can review the advantages of iDroop over DC and VI.

Clearly, iDroop achieves the same synchronous frequency and steady-state effort share as DC and VI do, both of which depend on $\alpha_{\mathrm{b},i}$. Yet, besides $\alpha_{\mathrm{b},i}$, iDroop provides us with two more degrees of freedom, δ_i and ν_i, which makes it capable of provably enhancing the dynamic frequency response performance

Table 4.2: Performance under Dynamic Droop Control

METRICS	DYNAMIC DROOP CONTROL
Synchronous frequency	$\frac{\sum_{i=1}^{n} \mu_{0,i}}{\sum_{i=1}^{n} (\alpha_{l,i} + \alpha_{t,i} + \alpha_{b,i})}$
Nadir elimination condition	$\delta_o = \frac{1}{\tau_{t,o}}$ and $\nu_o = \alpha_{b,o} + \alpha_{t,o}$
(Maximum) RoCoF lower bound	$\frac{\lvert\sum_{i=1}^{n} \mu_{0,i}\rvert}{\sum_{i=1}^{n} r_i} \frac{1}{m_o}$
Synchronization cost	0 if $\delta_o \to 0$ and $\nu_o \to \infty$
Frequency variance	$\frac{\left(\kappa_p^2 + \kappa_\omega^2 \alpha_{b,o}^2\right) m_o \delta_o^2 + \left(\kappa_p^2 + \kappa_\omega^2 \nu_o^2\right) (\check{\alpha}_o \delta_o + \lambda_k)}{2m_o \left[\check{\alpha}_o m_o \delta_o^2 + (\alpha_{l,o} + \nu_o) (\check{\alpha}_o \delta_o + \lambda_k)\right]} \sum_{i=1}^{n} \frac{1}{r_i}$
Steady-state effort share	$\frac{\sum_{i=1}^{n} \alpha_{b,i}}{\sum_{i=1}^{n} (\alpha_{l,i} + \alpha_{t,i} + \alpha_{b,i})}$

while preserving the desired steady-state performance. More precisely, iDroop can be tuned to achieve the Nadir elimination, zero synchronization cost, and low noise sensitivity, all of which are done in a way that incurs no influence on the steady-state performance.

Particularly, the Nadir elimination tuning given by $\delta_o = 1/\tau_{t,o}$ and $\nu_o = \alpha_{b,o} + \alpha_{t,o}$ has the potential to strike a good trade-off among various performance metrics in reality for the following reason. Usually, in real power systems, the stochastic power fluctuations are larger than the frequency measurement noise, i.e., $\kappa_p \gg \kappa_\omega$. Provided that $\kappa_p \gg \kappa_\omega$, we know from Lemma 4.3 that $\nu_o^\star \approx \kappa_p/\kappa_\omega$. Thus, for realistic values of parameters, $\nu_o^\star \gg \alpha_{b,o}$ always holds. It follows directly that $\nu_o = \alpha_{b,o} + \alpha_{t,o} \in (\alpha_{b,o}, \nu_o^\star]$. By Theorem 4.5, iDroop performs better than DC in terms of frequency variance. Therefore,

no matter in step or noise input scenarios, the Nadir elimination tuning of iDroop is a promising choice.

Nevertheless, iDroop has no control over the RoCoF, which is undesirable. It is known that a large RoCoF can trigger Loss of Mains protection [44] which is designed to ensure that generators shut down safely if a disconnection from the main grid is detected. However, in low-inertia power systems, this kind of protection is regarded as overly sensitive to distinguish between a local disconnection and the normal operation. Thus, we wish to propose a control law that is able to tune the RoCoF.

4.3 Frequency Shaping Control

Inverter Dynamics 4 (Frequency Shaping Control). *The dynamics of an inverter with FS is given by the transfer function*

$$\hat{c}_i(s) = -\frac{m_{\mathrm{v},i}s^2 + \nu_i s + \delta_i \alpha_{\mathrm{b},i}}{(\tau_{\mathrm{h},i}s + 1)(s + \delta_i)}, \tag{4.27}$$

where $m_{\mathrm{v},i} \geq 0$, $\nu_i \geq 0$, $\alpha_{\mathrm{b},i} \geq 0$, $\delta_i \geq 0$, *and* $\tau_{\mathrm{h},i} \geq 0$ *are tunable parameters.*

Under Assumption 3.1, the representative inverter under FS in (4.27) is given by

$$\hat{c}_{\mathrm{o}}(s) = -\frac{m_{\mathrm{v,o}}s^2 + \nu_{\mathrm{o}} s + \delta_{\mathrm{o}} \alpha_{\mathrm{b,o}}}{(\tau_{\mathrm{h,o}}s + 1)(s + \delta_{\mathrm{o}})} \tag{4.28}$$

with $m_{\mathrm{v},i} = r_i m_{\mathrm{v,o}}$, $\nu_i = r_i \nu_{\mathrm{o}}$, $\alpha_{\mathrm{b},i} = r_i \alpha_{\mathrm{b,o}}$, $\delta_i = \delta_{\mathrm{o}}$, and $\tau_{\mathrm{h},i} = \tau_{\mathrm{h,o}}$, $\forall i \in [n]$. Again, we define $\breve{\alpha}_{\mathrm{o}} := \alpha_{\mathrm{l,o}} + \alpha_{\mathrm{b,o}}$ and $\breve{m}_{\mathrm{o}} := m_{\mathrm{o}} + m_{\mathrm{v,o}}$ as in previous chapters.

Theorem 4.6 (Frequency Shaping Tuning). *Let Assumptions 2.2, 3.1, and 3.2*

hold. By setting

$$\nu_{\mathrm{o}} = \alpha_{\mathrm{b,o}} + \alpha_{\mathrm{t,o}} + \frac{m_{\mathrm{v,o}}}{\tau_{\mathrm{t,o}}}, \qquad \delta_{\mathrm{o}} = \frac{1}{\tau_{\mathrm{t,o}}}, \qquad \textit{and} \qquad \tau_{\mathrm{h,o}} \gg \tau_{\mathrm{t,o}} \tag{4.29}$$

in (4.28)*, the COI frequency deviation of the system* $\hat{\boldsymbol{T}}_{\omega\mathrm{p,FS}}(s)$ *is shaped approximately into a first-order response given by*

$$\bar{\omega}_{\mathrm{FS}}(t) \approx \frac{\sum_{i=1}^{n} \mu_{0,i}}{(\alpha_{\mathrm{l,o}} + \alpha_{\mathrm{b,o}} + \alpha_{\mathrm{t,o}}) \sum_{i=1}^{n} r_i} \left(1 - e^{-\frac{\alpha_{\mathrm{l,o}} + \alpha_{\mathrm{b,o}} + \alpha_{\mathrm{t,o}}}{m_{\mathrm{o}} + m_{\mathrm{v,o}}} t}\right), \tag{4.30}$$

whose Nadir elimination is achieved naturally. In this case, the synchronous frequency and RoCoF of the system $\hat{\boldsymbol{T}}_{\omega\mathrm{p,FS}}(s)$ *are determined by* (4.5) *and*

$$\|\dot{\bar{\omega}}_{\mathrm{FS}}\|_{\mathcal{L}_\infty} \approx \frac{|\sum_{i=1}^{n} \mu_{0,i}|}{\sum_{i=1}^{n} r_i} \frac{1}{m_{\mathrm{o}} + m_{\mathrm{v,o}}}, \tag{4.31}$$

respectively.

Proof. From (3.16), we know that the COI frequency deviation of the system $\hat{\boldsymbol{T}}_{\omega\mathrm{p,FS}}(s)$ is given by

$$\bar{\omega}_{\mathrm{FS}}(t) = \frac{\sum_{i=1}^{n} \mu_{0,i}}{\sum_{i=1}^{n} r_i} h_{\mathrm{u,1,FS}}(t), \tag{4.32}$$

where $h_{\mathrm{u,1,FS}}(t)$ is the unit-step response of $\hat{h}_{\mathrm{p,1,FS}}(s)$. Suppose that our desired $\hat{h}_{\mathrm{p,1,FS}}(s)$ is a first-order transfer function given by

$$\hat{h}_{\mathrm{p,1,FS}}(s) = \frac{1}{\breve{m}_{\mathrm{o}} s + \breve{\alpha}_{\mathrm{o}} + \alpha_{\mathrm{t,o}}}. \tag{4.33}$$

Then, using (3.2) and (4.33), one can directly solve for the desired representative control law $\hat{c}_{\mathrm{od}}(s)$ from (3.10) as

$$\hat{c}_{\mathrm{od}}(s) = \frac{\hat{h}_{\mathrm{p,1,FS}}(s) - \hat{g}_{\mathrm{o}}(s)}{\hat{h}_{\mathrm{p,1,FS}}(s)\hat{g}_{\mathrm{o}}(s)} = -\frac{m_{\mathrm{v,o}} s^2 + \nu_{\mathrm{o}} s + \delta_{\mathrm{o}} \alpha_{\mathrm{b,o}}}{s + \delta_{\mathrm{o}}} \tag{4.34}$$

with ν_{o} and δ_{o} given by (4.29).

However, $\hat{c}_{\mathrm{od}}(s)$ could introduce unbounded frequency variance in response to noise for a similar reason as in the case of VI. To see this, we apply (3.1) and $\hat{c}_{\mathrm{o}}(s) = \hat{c}_{\mathrm{od}}(s)$ to (3.11), which yields

$$\hat{h}_{\omega,k,\mathrm{FSd}}(s) = -\frac{m_{\mathrm{v,o}}s^3 + \nu_{\mathrm{o}}s^2 + \delta_{\mathrm{o}}\alpha_{\mathrm{b,o}}s}{\check{m}_{\mathrm{o}}s^3 + (m_{\mathrm{o}}\delta_{\mathrm{o}} + \alpha_{\mathrm{l,o}} + \nu_{\mathrm{o}})\,s^2 + (\delta_{\mathrm{o}}\check{\alpha}_{\mathrm{o}} + \lambda_k)\,s + \delta_{\mathrm{o}}\lambda_k}\,.$$

This can be turned into the form of (3.36) with $b_4 = \hat{h}_{\omega,k,\mathrm{FSd}}(\infty) = -m_{\mathrm{v,o}}/\check{m}_{\mathrm{o}} \neq 0$. Thus, by Lemma 3.5, $\|\hat{h}_{\omega,k,\mathrm{FSd}}\|^2_{\mathcal{H}_2} = \infty$. Then, $\|\hat{\boldsymbol{T}}_{\omega\mathrm{n,FSd}}\|^2_{\mathcal{H}_2} = \infty$ follows directly from Theorem 3.5. Therefore, to overcome this problem, we add a high frequency pole at $s = -1/\tau_{\mathrm{h,o}}$ with $\tau_{\mathrm{h,o}} \gg \tau_{\mathrm{t,o}}$ to $\hat{c}_{\mathrm{od}}(s)$, which yields the representative FS in (4.28).

Since the added high frequency pole in the representative FS would not interfere the desired evolution of the COI frequency deviation so much, from (4.32) and (4.33), we have

$$\begin{aligned}\hat{\bar{\omega}}_{\mathrm{FS}}(s) &\approx \frac{\sum_{i=1}^n \mu_{0,i}}{\sum_{i=1}^n r_i}\frac{1}{s\,(\check{m}_{\mathrm{o}}s + \check{\alpha}_{\mathrm{o}} + \alpha_{\mathrm{t,o}})} \\ &= \frac{\sum_{i=1}^n \mu_{0,i}}{(\check{\alpha}_{\mathrm{o}} + \alpha_{\mathrm{t,o}})\sum_{i=1}^n r_i}\left[\frac{1}{s} - \frac{1}{s + (\check{\alpha}_{\mathrm{o}} + \alpha_{\mathrm{t,o}})/\check{m}_{\mathrm{o}}}\right],\end{aligned}$$

whose time domain counterpart is exactly (4.30). From (4.30), we know

$$\bar{\omega}_{\mathrm{FS}}(\infty) \approx \frac{\sum_{i=1}^n \mu_{0,i}}{(\alpha_{\mathrm{l,o}} + \alpha_{\mathrm{b,o}} + \alpha_{\mathrm{t,o}})\sum_{i=1}^n r_i} = \frac{\sum_{i=1}^n \mu_{0,i}}{\sum_{i=1}^n (\alpha_{\mathrm{l},i} + \alpha_{\mathrm{t},i} + \alpha_{\mathrm{b},i})}\,.$$

Note that $\bar{\omega}_{\mathrm{FS}}(t)$ is equivalent to the unit-step response of the first-order system $\hat{h}_{\mathrm{p,1,FS}}(s)$ in (4.33) scaled by $(\sum_{i=1}^n \mu_{0,i})/(\sum_{i=1}^n r_i)$. Thus, we can apply

Theorem 3.2 to $\hat{h}_{\mathrm{p},1,\mathrm{FS}}(s)$, which yields

$$\|\dot{\tilde{\omega}}_{\mathrm{FS}}\|_{\mathcal{L}_\infty} = \left|\frac{\sum_{i=1}^n \mu_{0,i}}{\sum_{i=1}^n r_i}\right| K = \frac{|\sum_{i=1}^n \mu_{0,i}|}{\sum_{i=1}^n r_i}\frac{1}{\check{m}_{\mathrm{o}}}.$$

This concludes the proof. □

Theorem 4 reflects the most outstanding feature of FS. That is, with the tuning in (4.29), FS is able to fashion the COI frequency dynamics following a sudden power imbalance into a first-order one with the specified synchronous frequency and RoCoF by adjusting the control parameters $\alpha_{\mathrm{b,o}}$ and $m_{\mathrm{v,o}}$, respectively. Notably, a first-order COI frequency evolution naturally avoids the overshoot so that the Nadir elimination is achieved inherently.

Remark 4.4 (Relationship Between FS and iDroop). *Note that FS reduces to iDroop if we set $m_{\mathrm{v},i} = 0$ and $\tau_{\mathrm{h},i} = 0$. Thus, it preserves all the properties of iDroop. More precisely, it can achieve low noise sensitivity and zero synchronization cost with properly chosen ν_i and δ_i. Although the preferred values of parameters for different performance metrics may not necessarily coincide with each other, FS does provide us with the extra freedom to tune the RoCoF compared with iDroop.*

Remark 4.5 (Simple Frequency Security Certification Procedure under FS). *The significance of Nadir elimination lies in that it allows us to certify the frequency security of the power system by performing simple algebraic calculations instead of running explicit dynamic simulations. For example, given the expected maximum magnitude of net power imbalance $|\sum_{i=1}^n \mu_{0,i}|_{\mathrm{allowed}}$ as well as the acceptable maximum magnitude of RoCoF $\|\dot{\tilde{\omega}}\|_{\mathcal{L}_\infty,\mathrm{allowed}}$ and COI frequency deviation*

$\|\bar{\omega}\|_{\mathcal{L}_\infty,\text{allowed}}$, *according to the frequency shaping tuning, one can simply choose:*

$$m_{\text{v,o}} = \max\left(\frac{|\sum_{i=1}^{n}\mu_{0,i}|_{\text{allowed}}}{\|\dot{\bar{\omega}}\|_{\mathcal{L}_\infty,\text{allowed}}\sum_{i=1}^{n}r_i} - m_{\text{o}}, 0\right),$$

$$\alpha_{\text{b,o}} = \max\left(\frac{|\sum_{i=1}^{n}\mu_{0,i}|_{\text{allowed}}}{\|\bar{\omega}\|_{\mathcal{L}_\infty,\text{allowed}}\sum_{i=1}^{n}r_i} - \alpha_{\text{l,o}} - \alpha_{\text{t,o}}, 0\right),$$

and ν_{o}, δ_{o}, $\tau_{\text{h,o}}$ *as in* (4.29).

Remark 4.6 (Generalization of FS Tuning). *The FS tuning described by* (4.29) *was derived for a simplified first-order turbine-governor model. Actually, the same methodology can be applied to deriving FS tuning for more general cases. To see this, we rewrite* (4.28) *with FS tuning in* (4.29) *as*

$$\begin{aligned}
\hat{c}_{\text{o}}(s) &= -\frac{m_{\text{v,o}}s^2 + (\alpha_{\text{b,o}} + \alpha_{\text{t,o}} + m_{\text{v,o}}/\tau_{\text{t,o}})\,s + \alpha_{\text{b,o}}/\tau_{\text{t,o}}}{(\tau_{\text{h,o}}s+1)\,(s+1/\tau_{\text{t,o}})} \\
&= -\frac{m_{\text{v,o}}s\,(s+1/\tau_{\text{t,o}}) + \alpha_{\text{b,o}}\,(s+1/\tau_{\text{t,o}}) + \alpha_{\text{t,o}}s}{(\tau_{\text{h,o}}s+1)\,(s+1/\tau_{\text{t,o}})} \\
&= -\frac{1}{\tau_{\text{h,o}}s+1}\left(m_{\text{v,o}}s + \alpha_{\text{b,o}} + \frac{\alpha_{\text{t,o}}\tau_{\text{t,o}}s}{\tau_{\text{t,o}}s+1}\right) \\
&= \frac{1}{\tau_{\text{h,o}}s+1}\left[-m_{\text{v,o}}s - (\alpha_{\text{b,o}} + \alpha_{\text{t,o}}) + \frac{\alpha_{\text{t,o}}}{\tau_{\text{t,o}}s+1}\right].
\end{aligned} \tag{4.35}$$

Observe from (4.35) *that the FS tuning is a filtered combination of VI and iDroop with Nadir elimination tuning. More precisely, the* $-m_{\text{v,o}}s$ *term from VI represents the inertial response that is responsible for the RoCoF, while the* $-(\alpha_{\text{b,o}} + \alpha_{\text{t,o}})$ *term and the* $\alpha_{\text{t,o}}/(\tau_{\text{t,o}}s+1)$ *term from iDroop are responsible for the synchronous frequency and Nadir elimination, respectively. As discussed in Remark* 4.3*, the key to achieving Nadir elimination is to cancel out the turbine-governor dynamics. Thus, if we denote the transfer function of any arbitrary turbine-governor as* $-\alpha_{\text{t},i}\hat{v}_i(s)$ *with* $\hat{v}_i(0) = 1$,

then we can easily generalize (4.35) *by replacing the simplified* $\alpha_{t,o}/\left(\tau_{t,o}s+1\right)$ *with* $\alpha_{t,o}\hat{v}_o(s)$ *satisfying*

$$\alpha_{t,o}\hat{v}_o(s) := \frac{\sum_{i=1}^{n}\alpha_{t,i}\hat{v}_i(s)}{\sum_{i=1}^{n} r_i} \qquad \textit{and} \qquad \hat{v}_o(0) = 1\,. \tag{4.36}$$

This leads to the following generalization of FS tuning for any arbitrary turbine-governor modelled as $-\alpha_{t,i}\hat{v}_i(s)$ *with* $\hat{v}_i(0) = 1$*:*

$$\hat{c}_o(s) = \frac{1}{\tau_{h,o}s+1}\left[-m_{v,o}s - (\alpha_{b,o}+\alpha_{t,o}) + \alpha_{t,o}\hat{v}_o(s)\right]\,. \tag{4.37}$$

Similarly, the Nadir elimination tuning of iDroop can be generalized to

$$\hat{c}_o(s) = -\left(\alpha_{b,o}+\alpha_{t,o}\right) + \alpha_{t,o}\hat{v}_o(s)\,. \tag{4.38}$$

Note that, although it is possible to use the fully detailed $\alpha_{t,o}\hat{v}_o(s)$ *as defined in* (4.36)*, numerical simulations suggest that even a simple second-order reduced model [43] of* $\alpha_{t,o}\hat{v}_o(s)$ *obtained from the balanced truncation procedure provides remarkably good performance for above tuning.*

Chapter 5

Numerical Illustrations

This chapter validates our theoretical results through a numerical example with more complex models for both the energy storage and the power system. In Section 5.1, we provide a more detailed representation of the energy storage, which explicitly models the dynamics of the interfacing voltage source converter (VSC) with the phase-locked loop (PLL) and inner current control loop. In Section 5.2, we perform simulations on a more realistic power system test case using Power System Toolbox (PST) [60] for Matlab.

5.1 Modelling of Voltage Source Converter

When conducting our theoretical analysis, we have assumed that the measurement process of the grid frequency is rather fast and accurate. Thus, we used the grid frequency as an input signal to the frequency control directly. Likewise, an assumption of rapid power injection variations by the energy storage was made so that the energy storage is considered to follow power commands for frequency control instantly. However, in practice, energy

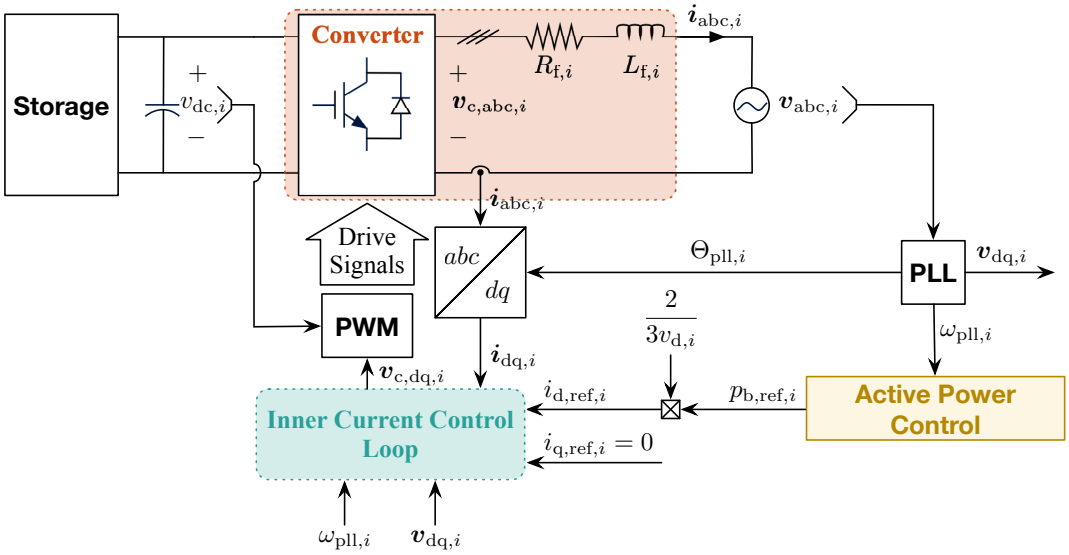

Figure 5.1: Energy storage control scheme

storage is interfaced to the grid through power electronic converters, where a VSC is commonly applied. Therefore, we extend our modelling approach to explicitly account for VSC dynamics in this section.

Figure 5.1 shows the configuration of the energy storage feeding into the grid through a VSC for frequency control. Here, the main objective of the grid-following VSC acting as a current source is to adjust its power injection to the grid according to the grid frequency deviation at the bus where it is located [61, 62]. With this aim, the VSC first measures the grid frequency deviation using a PLL, and then generates the current reference following the power control, and finally yields the modulation reference that is fed to the pulse width modulation (PWM) from the inner current control loop.

We now discuss the elements mentioned above in more detail. We mostly follow the approach from [63], since the energy storage models presented there are specifically derived and tested for power systems transient stability

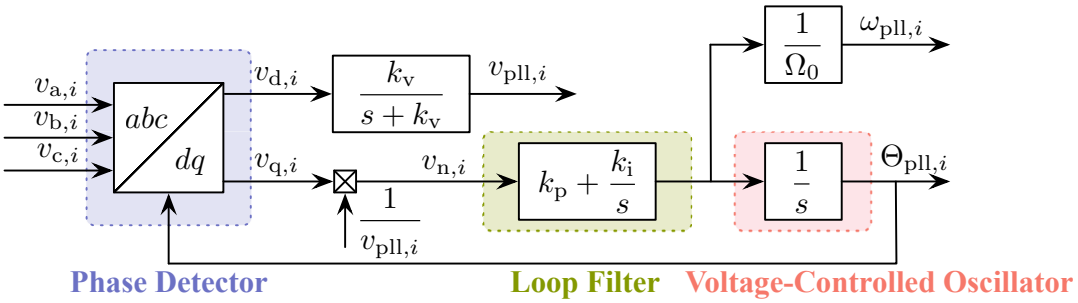

Figure 5.2: Block diagram of the SRF-PLL

analysis. We also refer to [16, 64–66].

5.1.1 Phase-Locked Loop

We adopt a typical synchronous reference frame PLL (SRF-PLL) [65] composed of a phase detector, a loop filter, and a voltage-controlled oscillator as shown in Figure 5.2 to measure the grid frequency deviation at the ith bus, $\forall i \in [n]$.

The phase detector provides the phase error information by transforming the three-phase grid voltage at the ith bus $v_{\text{abc},i}$ from the abc natural reference frame to the dq synchronous reference frame. Here, we assume ideal grid conditions with neither imbalance nor harmonics, i.e,

$$v_{\text{abc},i} := \begin{bmatrix} v_{\text{a},i} \\ v_{\text{b},i} \\ v_{\text{c},i} \end{bmatrix} = |V_i| \begin{bmatrix} \cos\left(\Omega_0 t + \Theta_i\right) \\ \cos\left(\Omega_0 t + \Theta_i - \frac{2\pi}{3}\right) \\ \cos\left(\Omega_0 t + \Theta_i + \frac{2\pi}{3}\right) \end{bmatrix}, \tag{5.1}$$

where $|V_i|$ and Θ_i are the amplitude (in p.u.) and phase (in rad) of the grid voltage at the ith bus, respectively. Then the d- and q-axis components of the grid voltage at the ith bus are known to be

$$v_{\text{d},i} = |V_i| \cos\left(\Theta_i - \Theta_{\text{pll},i}\right), \tag{5.2a}$$

$$v_{\mathrm{q},i} = |V_i| \sin\left(\Theta_i - \Theta_{\mathrm{pll},i}\right), \tag{5.2b}$$

where $\Theta_{\mathrm{pll},i}$ is the estimated grid phase (in rad) at the ith bus. Equation (5.2) indicates that the key to estimate Θ_i is to keep $v_{\mathrm{q},i}$ close to zero since $v_{\mathrm{q},i} \approx |V_i|\left(\Theta_i - \Theta_{\mathrm{pll},i}\right) \approx 0$ requires $\Theta_{\mathrm{pll},i} \approx \Theta_i$. It also follows that $v_{\mathrm{d},i} \approx |V_i|$, which means that $v_{\mathrm{d},i}$ estimates the amplitude of the grid voltage at the ith bus. To make the PLL performance insensitive to variations in $|V_i|$, a normalization dividing $v_{\mathrm{q},i}$ by $v_{\mathrm{pll},i}$ is included [65], where $v_{\mathrm{pll},i}$ is obtained by passing $v_{\mathrm{d},i}$ through a low-pass filter with a cutoff frequency k_{v}, i.e.,

$$\hat{v}_{\mathrm{pll},i} = \frac{k_{\mathrm{v}}}{s + k_{\mathrm{v}}} \hat{v}_{\mathrm{d},i} \qquad \text{or} \qquad \dot{v}_{\mathrm{pll},i} = k_{\mathrm{v}}\left(v_{\mathrm{d},i} - v_{\mathrm{pll},i}\right). \tag{5.3}$$

The loop filter forces $v_{\mathrm{q},i}$ to zero through a proportional–integral controller. Thus, the estimated grid frequency deviation (in p.u.) at the ith bus $\omega_{\mathrm{pll},i}$ is determined from the normalized $v_{\mathrm{q},i}$, i.e., $v_{\mathrm{n},i} := v_{\mathrm{q},i}/v_{\mathrm{pll},i}$, through the following dynamics

$$\Omega_0 \hat{\omega}_{\mathrm{pll},i} = \left(k_{\mathrm{p}} + \frac{k_{\mathrm{i}}}{s}\right) \hat{v}_{\mathrm{n},i} \qquad \text{or} \qquad \Omega_0 \dot{\omega}_{\mathrm{pll},i} = k_{\mathrm{p}} \dot{v}_{\mathrm{n},i} + k_{\mathrm{i}} v_{\mathrm{n},i}, \tag{5.4}$$

where k_{p} and k_{i} are the proportional and integral gains.

The voltage-controlled oscillator generates the estimated grid phase at the ith bus $\Theta_{\mathrm{pll},i}$ via the integration of the estimated grid frequency deviation (in rad s^{-1}) at the ith bus $\Omega_0 \omega_{\mathrm{pll},i}$, i.e.,

$$\hat{\Theta}_{\mathrm{pll},i} = \frac{\Omega_0 \hat{\omega}_{\mathrm{pll},i}}{s} \qquad \text{or} \qquad \dot{\Theta}_{\mathrm{pll},i} = \Omega_0 \omega_{\mathrm{pll},i}. \tag{5.5}$$

Therefore, the PLL dynamics is included in our simulations through

the model described by (5.2)–(5.5), where we set $k_{\mathrm{v}} = 140\,\mathrm{s}^{-1}$ [66], $k_{\mathrm{p}} = 8.4\,\mathrm{rad\,s}^{-1}$, and $k_{\mathrm{i}} = 100\,\mathrm{rad\,s}^{-2}$, corresponding to a bandwidth around $17.4\,\mathrm{rad\,s}^{-1}$ [16, Table 4.1].

5.1.2 Power Controller

The inverter control laws discussed in Chapter 4, including DC, VI, iDroop, and FS, play the role of a active power controller. The active power controller at the ith bus maps the estimated grid frequency deviation $\omega_{\mathrm{pll},i}$ to a real power output variation reference (in p.u.) $p_{\mathrm{b,ref},i}$ around the equilibrium operating point according to the particular law $\hat{c}_i(s)$ adopted, i.e.,

$$\hat{p}_{\mathrm{b,ref},i} = \hat{c}_i(s)\hat{\omega}_{\mathrm{pll},i}\,, \tag{5.6}$$

where $p_{\mathrm{b,ref},i}$ is used to generate the reference signals (in p.u.) $i_{\mathrm{d,ref},i}$ and $i_{\mathrm{q,ref},i}$ for the inner current controller. Note that we assume that no reactive power control is executed by the converter, i.e., $i_{\mathrm{q,ref},i} = 0$. Thus, $i_{\mathrm{d,ref},i}$ can be found from the active power expression

$$p_{\mathrm{b,ref},i} = \frac{3}{2}\left(v_{\mathrm{d},i}i_{\mathrm{d,ref},i} + v_{\mathrm{q},i}i_{\mathrm{q,ref},i}\right) = \frac{3}{2}v_{\mathrm{d},i}i_{\mathrm{d,ref},i}$$

as

$$i_{\mathrm{d,ref},i} = \frac{2p_{\mathrm{b,ref},i}}{3v_{\mathrm{d},i}}\,. \tag{5.7}$$

5.1.3 Converter and Current Controller

We consider a conventional converter and inner current control loop in the dq-frame [16, 63, 64] with the block diagram as shown in Figure 5.3. The

dynamics of the d- and q-axis components of the converter output current at the ith bus $\boldsymbol{i}_{\mathrm{abc},i}$ are given by

$$L_{\mathrm{f},i}\dot{i}_{\mathrm{d},i} = -R_{\mathrm{f},i}i_{\mathrm{d},i} + \omega_{\mathrm{pll},i}L_{\mathrm{f},i}i_{\mathrm{q},i} + v_{\mathrm{c,d},i} - v_{\mathrm{d},i}\,, \tag{5.8a}$$

$$L_{\mathrm{f},i}\dot{i}_{\mathrm{q},i} = -R_{\mathrm{f},i}i_{\mathrm{q},i} - \omega_{\mathrm{pll},i}L_{\mathrm{f},i}i_{\mathrm{d},i} + v_{\mathrm{c,q},i} - v_{\mathrm{q},i}\,, \tag{5.8b}$$

with $R_{\mathrm{f},i}$ and $L_{\mathrm{f},i}$ being the resistance and inductance of the converter output filter at the ith bus. Here, $\boldsymbol{v}_{\mathrm{c,dq},i}$ are the converter output voltages before the filter in the dq-frame at the ith bus. A standard technique for decoupling $i_{\mathrm{d},i}$ and $i_{\mathrm{q},i}$ is to set [64]

$$\boldsymbol{v}_{\mathrm{c,dq}} := \begin{bmatrix} v_{\mathrm{c,d},i} \\ v_{\mathrm{c,q},i} \end{bmatrix} = \begin{bmatrix} u_{\mathrm{d},i} - \omega_{\mathrm{pll},i}L_{\mathrm{f},i}i_{\mathrm{q},i} + v_{\mathrm{d},i} \\ u_{\mathrm{q},i} + \omega_{\mathrm{pll},i}L_{\mathrm{f},i}i_{\mathrm{d},i} + v_{\mathrm{q},i} \end{bmatrix}, \tag{5.9}$$

where $u_{\mathrm{d},i}$ and $u_{\mathrm{q},i}$ are control signals to be chosen. Applying (5.9) to (5.8) yields

$$L_{\mathrm{f},i}\dot{i}_{\mathrm{d},i} = -R_{\mathrm{f},i}i_{\mathrm{d},i} + u_{\mathrm{d},i} \qquad \text{and} \qquad L_{\mathrm{f},i}\dot{i}_{\mathrm{q},i} = -R_{\mathrm{f},i}i_{\mathrm{q},i} + u_{\mathrm{q},i}\,,$$

where $i_{\mathrm{d},i}$ and $i_{\mathrm{q},i}$ are independent. Now, by choosing

$$\hat{u}_{\mathrm{d},i} = \hat{K}_{\mathrm{c},i}(s)\left(\hat{i}_{\mathrm{d,ref},i} - \hat{i}_{\mathrm{d},i}\right) \qquad \text{and} \qquad \hat{u}_{\mathrm{q},i} = \hat{K}_{\mathrm{c},i}(s)\left(\hat{i}_{\mathrm{q,ref},i} - \hat{i}_{\mathrm{q},i}\right)$$

with

$$\hat{K}_{\mathrm{c},i}(s) = \frac{R_{\mathrm{f},i} + sL_{\mathrm{f},i}}{s\tau_{\mathrm{c}}}\,,$$

we can compensate for the converter output filter dynamics so as to make

$$\hat{i}_{\mathrm{d},i} = \frac{1}{\tau_{\mathrm{c}}s + 1}\hat{i}_{\mathrm{d,ref},i} \qquad \text{and} \qquad \hat{i}_{\mathrm{q},i} = \frac{1}{\tau_{\mathrm{c}}s + 1}\hat{i}_{\mathrm{q,ref},i} \tag{5.10}$$

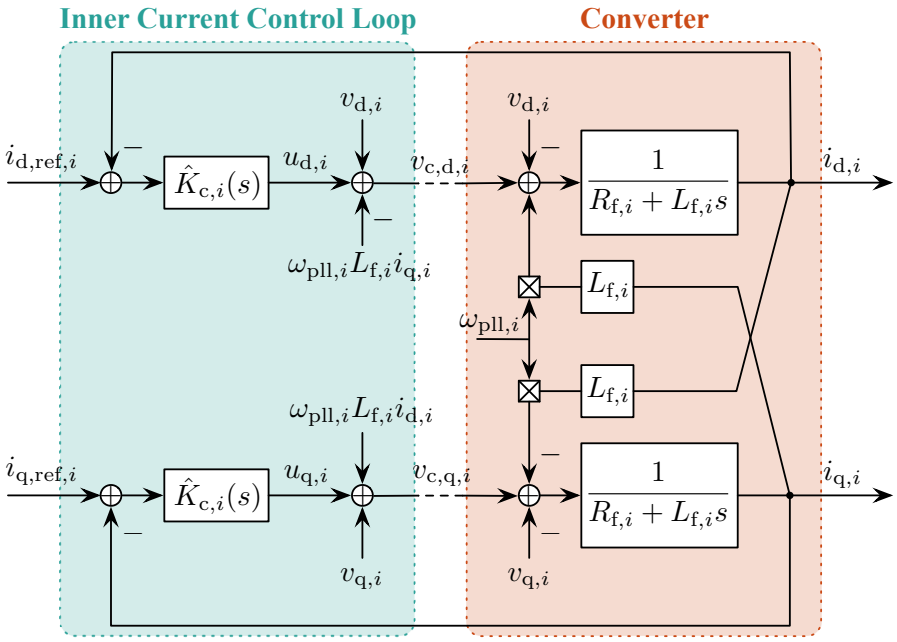

Figure 5.3: Block diagram of the converter and the inner current control loop in the dq-frame

with the desired inner current control time constant τ_{c} (in s) typically around milliseconds. In our simulations, we set $\tau_{\mathrm{c}} = 0.001\,\mathrm{s}$.

5.1.4 Effective Power-Frequency Response of Energy Storage

The power injection variation of the inverter-interfaced energy storage to the grid at the ith bus can be calculated by

$$p_{\mathrm{b},i} = \frac{3}{2}\left(v_{\mathrm{d},i} i_{\mathrm{d},i} + v_{\mathrm{q},i} i_{\mathrm{q},i}\right) \approx \frac{3}{2} v_{\mathrm{d},i} i_{\mathrm{d},i}\,,$$

where $i_{\mathrm{q},i} \approx 0$ is ensured by our setting that $i_{\mathrm{q,ref},i} = 0$. Therefore, after considering the converter and inner current control loop, we can characterize the effective power response of the energy storage to the estimated grid

frequency deviation as

$$\hat{p}_{\mathrm{b},i} \approx \frac{3v_{\mathrm{d},i}}{2}\hat{i}_{\mathrm{d},i} = \frac{3v_{\mathrm{d},i}}{2}\frac{1}{\tau_{\mathrm{c}}s+1}\hat{i}_{\mathrm{d,ref},i} = \frac{3v_{\mathrm{d},i}}{2}\frac{1}{\tau_{\mathrm{c}}s+1}\frac{2\hat{p}_{\mathrm{b,ref},i}}{3v_{\mathrm{d},i}} = \frac{\hat{c}_i(s)\hat{\omega}_{\mathrm{pll},i}}{\tau_{\mathrm{c}}s+1}\,, \quad (5.11)$$

where the first equality is due to (5.10), the second equality is due to (5.7), and the third equality is due to (5.6). Last but not least, although in our simulations we use the nonlinear PLL model described by (5.2)–(5.5), we can substitute its linearized counterpart [65, 66], i.e.,

$$\hat{\omega}_{\mathrm{pll},i} = \frac{k_{\mathrm{p}}s+k_{\mathrm{i}}}{s^2+k_{\mathrm{p}}s+k_{\mathrm{i}}}\hat{\omega}_i\,,$$

to (5.11) to get a concise transfer function from the true grid frequency deviation to the power injection variation of energy storage given by

$$\frac{\hat{p}_{\mathrm{b},i}}{\hat{\omega}_i} = \frac{k_{\mathrm{p}}s+k_{\mathrm{i}}}{s^2+k_{\mathrm{p}}s+k_{\mathrm{i}}}\frac{\hat{c}_i(s)}{\tau_{\mathrm{c}}s+1}\,. \quad (5.12)$$

For a device-level implementation, the control process abstracted by (5.12) is usually realized on a digital signal processor. The details of a device-level control realization are out of the scope of this thesis.

5.2 Case Study

We compare the performance of different frequency control laws by conducting simulations on the Western System Coordinating Council (WSCC) 9-bus 3-generator system given in Figure 5.4, using PST [60]. Attributed to PST, instead of the linear network model used in the analysis, the simulations are built upon a realistic setup including nonlinear power flows, line losses, and voltage dynamics.

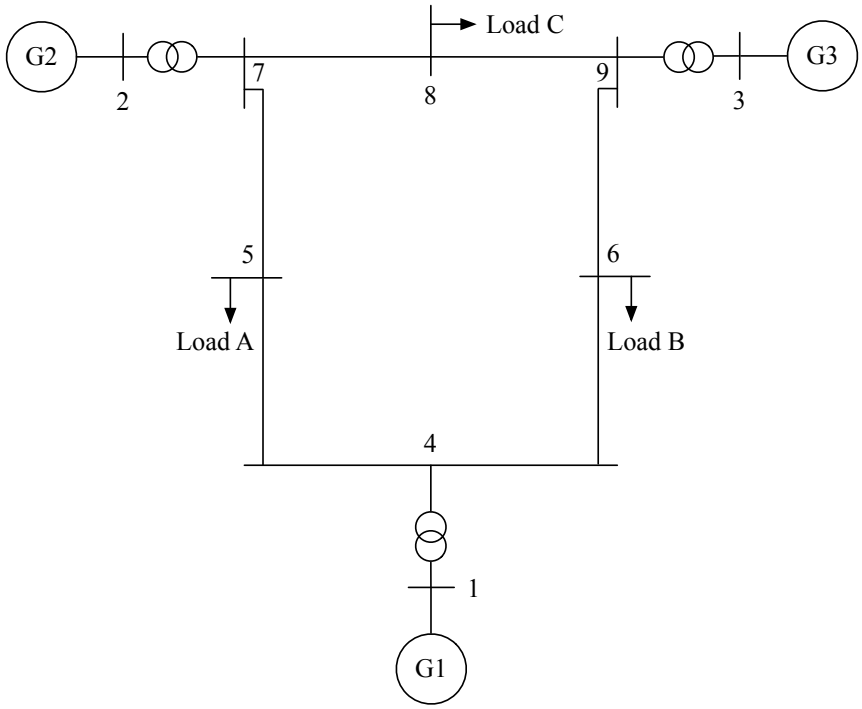

Figure 5.4: Single line diagram of the 9-bus 3-generator WSCC test case

5.2.1 System Description

The original test case contains 3 generator buses and 9 load buses. Each of the generator buses is distinctly indexed by some $i \in [3]$ and each of the load buses is distinctly indexed by some $i \in [9] \setminus [3]$. To mimic a low-inertia scenario, we modify parameter values of generator buses to emulate the Great Britain power system under the high renewable penetration scenario (see Examples 2.1 and 4.1). More precisely, the total system inertia is split slightly unevenly among three generator buses with $m_1 = 5.8\,\mathrm{s}$, $m_2 = 5.64\,\mathrm{s}$, and $m_3 = 1.7\,\mathrm{s}$, while the load-frequency sensitivity coefficients on three generator buses are equal, i.e., $\alpha_{1,1} = \alpha_{1,2} = \alpha_{1,3} = 1\,\mathrm{p.u.}$. Note that, although the simple

first- or second-order generator models are used in our analysis, the sub-transient generator models with multi-stage turbine-governors [67] equipped are adopted in our simulations, where the turbine dc gains (corresponding to the turbine inverse droop coefficients in the first-order turbine-governor model) are equal, i.e., $\alpha_{t,1} = \alpha_{t,2} = \alpha_{t,3} = 15\,\text{p.u.}$, but the turbine time constants are chosen to be somewhat heterogenous to make the test case more realistic. As before, we refer to this system without additional control from inverter-interfaced energy storage as SG. Clearly, the proportionality assumption (Assumption 3.1) required in our theoretical analysis is violated here.

We then place three inverter-interfaced energy storage units with explicit VSC models described in Section 5.1 at buses 4, 7, and 9, respectively, which are the load buses that are closest to the generator buses 1, 2, and 3, respectively. The active power controller $\hat{c}_i(s)$ in (5.6) imposed on each VSC can be either one of DC, VI, iDroop, and FS with $\hat{c}_1(s)$, $\hat{c}_2(s)$, and $\hat{c}_3(s)$ taking charge of the buses 4, 7, and 9, respectively.[1] Although our theoretical analysis does not contemplate jointly the effects of step disturbances and stochastic noise, we would like to explore here numerically the performance of different control laws in response to such combined input signals. To this end, for all simulations below, we add a step increase of active power load by 0.1689 p.u. to bus 5 at time $t = 1\,\text{s}$ as well as stochastic power fluctuations to all buses and frequency measurement noise to the estimated grid frequency deviation $\omega_{\text{pll},i}$ at buses 4, 7, and 9. Since in reality power fluctuations are usually larger than measurement noise, we focus on the case dominated by power fluctuations,

[1] One trick for implementing FS is to let the high frequency pole $s = -1/\tau_c$ introduced to (5.11) by the inner current control loop serve as the high frequency pole $s = -1/\tau_{h,i}$ needed in FS.

where $\kappa_{\mathrm{p}} = 10^{-4}$ and $\kappa_{\omega} = 10^{-5}$.

5.2.2 Controller Design

The design of control parameters in $\hat{c}_i(s)$ still relies on the knowledge of representative generator in some form even though the proportionality assumption is violated. We define the representative generator inertia constant as the mean of individual generator inertia constants, i.e.,

$$m_{\mathrm{o}} := \frac{1}{3}\sum_{i=1}^{3} m_i = \frac{5.8 + 5.64 + 1.7}{3}\,\mathrm{s} = 4.38\,\mathrm{s}\,. \tag{5.13}$$

Accordingly, the proportionality parameters are given by

$$r_i := \frac{m_i}{m_{\mathrm{o}}}\,, \qquad \forall i \in [3]\ . \tag{5.14}$$

Combining (5.13) and (5.14), we can get

$$\sum_{i=1}^{3} r_i = \frac{\sum_{i=1}^{3} m_i}{m_{\mathrm{o}}} = 3\,,$$

which is a result used frequently in the design of control parameters. Since the inertia constants are not defined for load buses in the original test case, we define

$$r_i := 0.01 \min_{j\in[3]} \left(r_j\right)\ , \qquad \forall i \in [9] \setminus [3]\ ,$$

for the purpose of scaling the noise according to the proportionally weighted noise assumption (Assumption 3.3). Then, we define the representative load-frequency sensitivity coefficient as

$$\alpha_{\mathrm{l,o}} := \frac{\sum_{i=1}^{3} \alpha_{\mathrm{l},i}}{\sum_{i=1}^{3} r_i}\,.$$

Since the complex multi-stage turbine-governors are involved in simulations, we can define the representative turbine-governor as suggested in Remark 4.6, i.e.,

$$\alpha_{\mathrm{t,o}}\hat{v}_{\mathrm{o}}(s) := \text{balred}\left(\frac{\sum_{i=1}^{3}\alpha_{\mathrm{t},i}\hat{v}_i(s)}{\sum_{i=1}^{3} r_i}, 2\right) \qquad \text{and} \qquad \hat{v}_{\mathrm{o}}(0) = 1\,, \tag{5.15}$$

where $\text{balred}(\hat{h}(s), n)$ computes a nth-order reduced model of $\hat{h}(s)$ using the balanced truncation procedure [68].

Now, we are ready to design control parameters. We start by examining the performance of SG as shown in Figure 5.5. Clearly, the Nadir is too close to the maximum allowed value for the Great Britain power system setting, which is 500 mHz. This is mainly a by-product of a large RoCoF, which should be clear soon. The synchronous frequency and RoCoF can be estimated algebraically by applying the results in Table 4.1 since SG can be considered as DC with $\alpha_{\mathrm{b,o}} = 0$. Thus, we get

$$\omega_{\text{syn,SG}} \approx \frac{\mu_{0,5}}{\sum_{i=1}^{3}(\alpha_{\mathrm{l},i} + \alpha_{\mathrm{t},i})} = \frac{-0.1689}{3 \times (1+15)}\,\text{p.u.} = -0.0035\,\text{p.u.}\,,$$

$$\|\dot{\bar{\omega}}_{\text{SG}}\|_{\mathcal{L}_\infty} \approx \frac{|\mu_{0,5}|}{\sum_{i=1}^{3} r_i}\frac{1}{m_{\mathrm{o}}} = \frac{|-0.1689|}{3} \times \frac{1}{4.38}\,\text{p.u.}\,\text{s}^{-1} = 0.0129\,\text{p.u.}\,\text{s}^{-1}\,.$$

We can also write the results above as

$$f_{\text{syn,SG}} \approx -175\,\text{mHz} \qquad \text{and} \qquad \|\dot{\bar{f}}_{\text{SG}}\|_{\mathcal{L}_\infty} \approx 0.645\,\text{Hz}\,\text{s}^{-1}$$

which match well with the simulation results in Figure 5.5. Recall from Section 2.3.2 that the maximum allowed quasi-steady-state frequency deviation is ± 200 mHz and the highest allowed RoCoF is $0.5\,\text{Hz}\,\text{s}^{-1}$. This means that

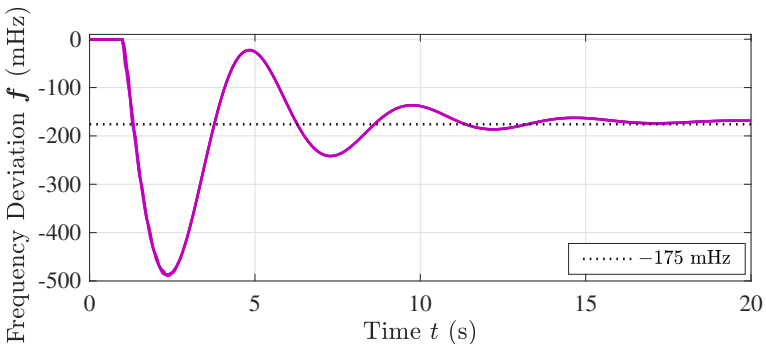

Figure 5.5: Performance of the modified WSCC test case when a step power imbalance and stochastic power fluctuations are introduced

the existing system SG suffices to provide satisfactory synchronous frequency but fails to meet the RoCoF requirement. Hence, there is no need to provide additional droop response via energy storage. Yet, it is desirable to reduce the RoCoF with the help of energy storage. In view of the above analysis, we directly rule DC out of our options since it contributes to frequency control solely by adding droop response which is not a necessity here. For the same reason, from now on, we only consider VI, iDroop, and FS with $\alpha_{\mathrm{b,o}} = 0$, which in fact helps to save energy by avoiding keeping power output from storage for nonzero frequency deviations.

Noticeably, FS seems tailor-made for the task of improving the frequency response performance of this system since, with the tuning proposed in (4.37), it is able to achieve both Nadir elimination and RoCoF reduction. A quick check of (4.37) shows that the only parameter remains to be designed is $m_{\mathrm{v,o}}$. This can be done easily by following Remark 4.5. When calculating $m_{\mathrm{v,o}}$, we set $\|\dot{\tilde{f}}\|_{\mathcal{L}_\infty,\mathrm{allowed}} = 0.4\,\mathrm{Hz\,s^{-1}} < 0.5\,\mathrm{Hz\,s^{-1}}$, i.e., $\|\dot{\tilde{\omega}}\|_{\mathcal{L}_\infty,\mathrm{allowed}} = 0.008\,\mathrm{p.u.\,s^{-1}}$, to

preserve some margin for frequency security. Thus, we have

$$m_{\mathrm{v,o}} = \max\left(\frac{|\mu_{0,5}|}{\|\dot{\tilde{\omega}}\|_{\mathcal{L}_\infty,\text{allowed}} \sum_{i=1}^{3} r_i} - m_{\mathrm{o}}, 0\right)$$

$$= \max\left[\left(\frac{|-0.1689|}{0.008 \times 3} - 4.38\right)\mathrm{s}, 0\right] = \max\left(2.6575\,\mathrm{s}, 0\right) = 2.6575\,\mathrm{s}\,.$$

Then, we set the ith active power controller under FS to be $\hat{c}_i(s) = r_i \hat{c}_{\mathrm{o}}(s)$ with $\hat{c}_{\mathrm{o}}(s)$ given by (4.37).

5.2.3 Performance Comparison

To provide a fair comparison of FS designed above with VI and iDroop, we do numerical experiments as illustrated in Figures 5.6 and 5.7.

Figures 5.6(a) and 5.7(a) compare the frequency deviations and net power output from energy storage, respectively, of the system under FS and VI for the case when VI is also tuned to provide a RoCoF of $0.4\,\mathrm{Hz\,s^{-1}}$ ($0.008\,\mathrm{p.u.\,s^{-1}}$). More precisely, we set $m_{\mathrm{v,o}} = 2.6575\,\mathrm{s}$ for the representative active power controller $\hat{c}_{\mathrm{o}}(s)$ under VI given by (4.4). Then, the ith active power controller under VI is $\hat{c}_i(s) = r_i \hat{c}_{\mathrm{o}}(s)$. A quick check can be done by applying the RoCoF expression of VI in Table 4.1 to verify that

$$\|\dot{\tilde{\omega}}_{\mathrm{VI}}\|_{\mathcal{L}_\infty} \approx \frac{|\mu_{0,5}|}{\sum_{i=1}^{3} r_i} \frac{1}{m_{\mathrm{o}} + m_{\mathrm{v,o}}}$$

$$= \frac{|-0.1689|}{3} \times \frac{1}{4.38 + 2.6575}\,\mathrm{p.u.\,s^{-1}} = 0.008\,\mathrm{p.u.\,s^{-1}}\,.$$

In this setting, the synchronous frequency and RoCoF are the same under FS and VI. Thus, considering that FS significantly picks up the frequency drop,

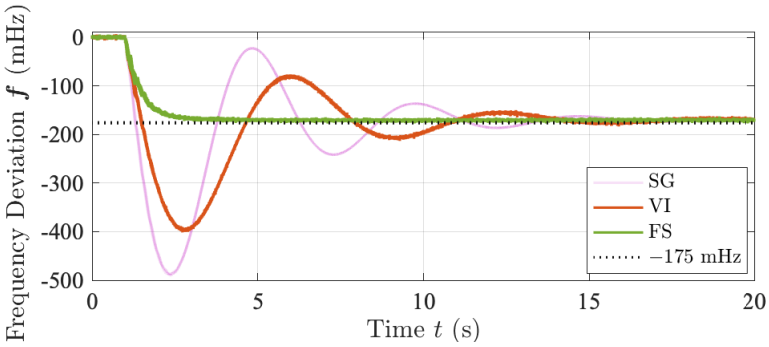

(a) When VI and FS are tuned to provide 0.4 Hz s^{-1} RoCoF

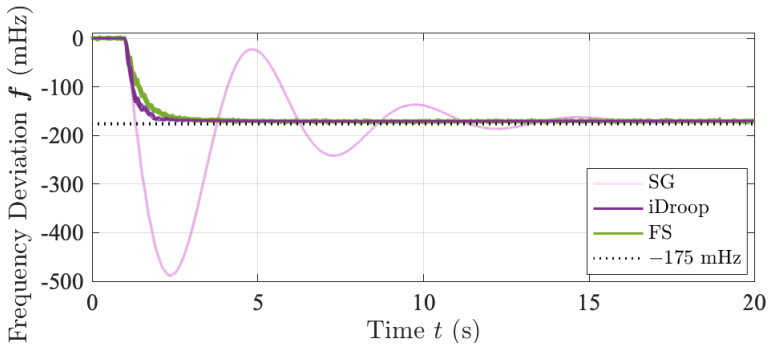

(b) When iDroop and FS are tuned to achieve Nadir elimination

Figure 5.6: Frequency deviations in the modified WSCC test case under different frequency control laws when a step power imbalance as well as stochastic power fluctuations and frequency measurement noise are introduced

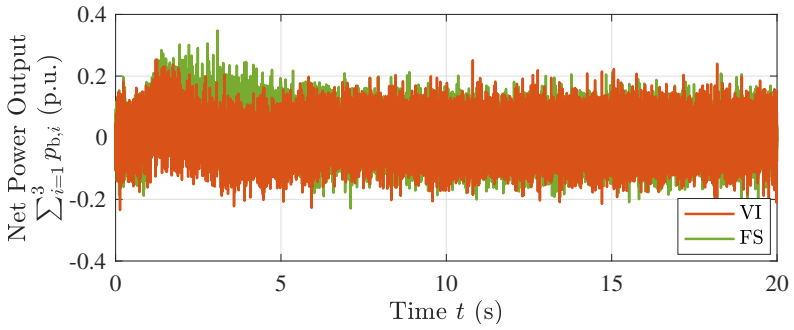

(a) When VI and FS are tuned to provide 0.4 Hz s^{-1} RoCoF

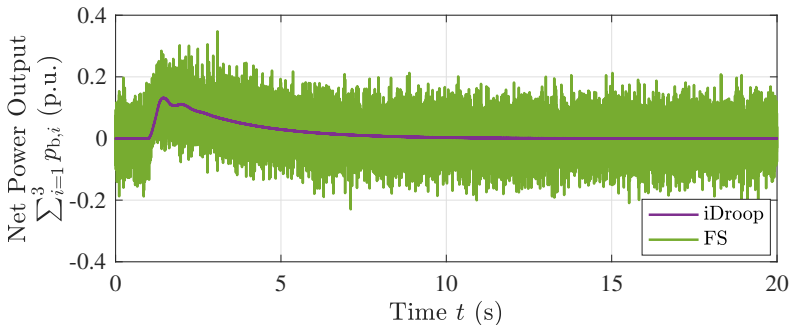

(b) When iDroop and FS are tuned to achieve Nadir elimination

Figure 5.7: Net power output from inverter-interfaced energy storage in the modified WSCC test case under different frequency control laws when a step power imbalance as well as stochastic power fluctuations and frequency measurement noise are introduced

there is no surprise that it requires a somewhat higher peak power compared with VI. However, FS is clearly smarter since it trades slightly increased peak power for complete Nadir elimination. Actually, the difference between the two power curves can be understood as an approximation of the energy used by the FS for Nadir elimination, whose amount is modest.

Remark 5.1 (Possible Instability Caused by VI). *One aspect we would like to highlight here is that it is not realistic to further increase $m_{\mathrm{v,o}}$ of VI until achieving Nadir elimination. An extremely large $m_{\mathrm{v,o}}$ is required to achieve Nadir elimination via VI for this system. However, simulations suggest that such a large $m_{\mathrm{v,o}}$ actually makes the system unstable rather than provides any benefit.*

Figures 5.6(b) and 5.7(b) compare the frequency deviations and net power output from energy storage, respectively, of the system under FS and iDroop for the case when iDroop is also tuned to achieve Nadir elimination. More precisely, we tune the representative active power controller $\hat{c}_{\mathrm{o}}(s)$ under iDroop as described in (4.38). Then, the ith active power controller under iDroop is $\hat{c}_i(s) = r_i \hat{c}_{\mathrm{o}}(s)$. In this setting, the frequency responses under FS and iDroop are both shaped well into first-order evolution. The only difference between the two frequency curves lies in the RoCoF. FS succeeds in reducing the RoCoF to $0.4\,\mathrm{Hz\,s^{-1}}$, while iDroop leaves it unchanged. Nevertheless, iDroop has much lower noise sensitivity compared with FS, which can be seen clearly from its smooth power curve. Last but not least, although the power curve of FS is quite noisy, its envelope suggests a similar amount of energy consumption by the grid as in iDroop.

Remark 5.2 (A Motivation for Grid-Forming Inverters). *Our simulations verify the high noise sensitivity of those active power controllers where there exist parameters playing the role of inertia. This is one of the drawbacks of the grid-following inverters which have to adjust their power output variations based on the grid frequency measurements. Recently, grid-forming inverters [24] have attracted a lot of attention from the research community. They set the grid frequency directly as a function of their power output variations, which makes them a potential solution to the problem of reducing noise sensitivity for two reasons. First, they help to avoid the noise introduced by the frequency measurements since there is no need to measure the grid frequency any more. Second, the inertial response can be realized through a proper transfer function in the grid-forming mode, which gets rid of the derivative terms that are sensitive to noise.*

Chapter 6

Conclusion

This thesis studies the impact of various frequency control laws imposed on inverter-interfaced energy storage to the power system performance. When it comes to the existing two common control laws, we show that DC cannot decouple the dynamic performance improvement from the steady-state performance and VI can introduce unbounded frequency variance in the presence of frequency measurement noise. Thus, we propose a new control law named iDroop, which is able to enhance the dynamic performance and preserve the steady-state performance at the same time. Specifically, we show that iDroop can be tuned to achieve Nadir elimination, zero synchronization cost, and low noise sensitivity. Yet, in view of the inability of iDroop to adjust RoCoF, we generalize it to FS which provides the extra freedom to tune RoCoF without loss of any property of iDroop. Although all analyses are conducted under a proportionality assumption, we illustrate numerically that the insights and advantages of the proposed control laws are still present even if the assumption is violated. All in all, this thesis confirms the superiority of principled control design over the naive imitation of synchronous generator behavior.

References

[1] D. S. Kirschen and G. Strbac. *Fundamentals of Power System Economics*. 2nd ed. Wiley, 2019.

[2] J. H. Eto, J. Undrill, P. Mackin, R. Daschmans, B. Williams, H. Illian, C. Martinez, M. O'Malley, K. Coughlin, and K. H. LaCommare. *Use of Frequency Response Metrics to Assess the Planning and Operating Requirements for Reliable Integration of Variable Renewable Generation*. Tech. rep. Lawrence Berkeley National Laboratory, 2010.

[3] "A world in transition". In: *Nature Energy* 1.15026 (2016).

[4] B. K. Bose. "Global energy scenario and impact of power electronics in 21st century". In: *IEEE Transactions on Industrial Electronics* 60.7 (2013), pp. 2638–2651.

[5] G. He, J. Lin, F. Sifuentes, X. Liu, N. Abhyankar, and A. Phadke. "Rapid cost decrease of renewables and storage accelerates the decarbonization of China's power system". In: *Nature Communications* 11.2486 (2020).

[6] *H.R.9—Climate Action Now Act*. Tech. rep. U.S. House Committee on Foreign Affairs, 2019.

[7] *Annual Energy Outlook 2021 with Projections to 2050*. Tech. rep. U.S. Energy Information Administration, 2021.

[8] B. Kroposki, B. Johnson, Y. Zhang, V. Gevorgian, P. Denholm, B. Hodge, and B. Hannegan. "Achieving a 100% renewable grid: Operating electric power systems with extremely high levels of variable renewable energy". In: *IEEE Power and Energy Magazine* 15.2 (2017), pp. 61–73.

[9] L. Bird, M. Milligan, and D. Lew. *Integrating Variable Renewable Energy: Challenges and Solutions*. Tech. rep. National Renewable Energy Laboratory, 2013.

[10] E. K. Hart, E. D. Stoutenburg, and M. Z. Jacobson. "The potential of intermittent renewables to meet electric power demand: Current methods and emerging analytical techniques". In: *Proceedings of the IEEE* 100.2 (2012), pp. 322–334.

[11] P. Denholm, T. Mai, R. W. Kenyon, B. Kroposki, and M. O'Malley. *Inertia and the Power Grid: A Guide Without the Spin*. Tech. rep. National Renewable Energy Laboratory, 2020.

[12] F. Milano, F. Dörfler, G. Hug, D. J. Hill, and G. Verbič. "Foundations and challenges of low-inertia systems (invited paper)". In: *Proc. of Power Systems Computation Conference*. 2018, pp. 1–25.

[13] F. P. DeMello, R. J. Mills, and W. F. B'Rells. "Automatic generation control part II—digital control techniques". In: *IEEE Transactions on Power Apparatus and Systems* PAS-92.2 (1973), pp. 716–724.

[14] T. Ackermann, T. Prevost, V. Vittal, A. J. Roscoe, J. Matevosyan, and N. Miller. "Paving the way: A future without inertia is closer than you think". In: *IEEE Power and Energy Magazine* 15.6 (2017), pp. 61–69.

[15] R. W. Erickson and D. Maksimović. *Fundamentals of Power Electronics*. 3rd ed. Springer, 2020.

[16] Y. Sun. "The impact of voltage-source-converters' control on the power system: The stability analysis of a power electronics dominant grid". PhD thesis. Eindhoven University of Technology, 2018.

[17] A. S. Ahmadyar, S. Riaz, G. Verbič, A. Chapman, and D. J. Hill. "A framework for assessing renewable integration limits with respect to frequency performance". In: *IEEE Transactions on Power Systems* 33.4 (2018), pp. 4444–4453.

[18] S. Kouro, B. Wu, H. Abu-Rub, and F. Blaabjerg. "Photovoltaic energy conversion systems". In: *Power Electronics for Renewable Energy Systems, Transportation and Industrial Applications*. Wiley, 2014. Chap. 7, pp. 160–198.

[19] B. P. Roberts and C. Sandberg. "The role of energy storage in development of smart grids". In: *Proceedings of the IEEE* 99.6 (2011), pp. 1139–1144.

[20] *Technical Report on the Events of 9 August 2019*. Tech. rep. National Grid Electricity System Operator, 2019.

[21] R. Ofir, U. Markovic, P. Aristidou, and G. Hug. "Droop vs. virtual inertia: Comparison from the perspective of converter operation mode". In: *Proc. of IEEE International Energy Conference*. 2018, pp. 1–6.

[22] L. Meng, J. Zafar, S. K. Khadem, A. Collinson, K. C. Murchie, F. Coffele, and G. M. Burt. "Fast frequency response from energy storage systems—a review of grid standards, projects and technical issues". In: *IEEE Transactions on Smart Grid* 11.2 (2020), pp. 1566–1581.

[23] M. A. Torres L., L. A. C. Lopes, L. A. Morán T., and J. R. Espinoza C. "Self-tuning virtual synchronous machine: A control strategy for energy storage systems to support dynamic frequency control". In: *IEEE Transactions on Energy Conversion* 29.4 (2014), pp. 833–840.

[24] B. K. Poolla, D. Gross, and F. Dörfler. "Placement and implementation of grid-forming and grid-following virtual inertia and fast frequency response". In: *IEEE Transactions on Power Systems* 34.4 (2019), pp. 3035–3046.

[25] S. S. Guggilam, C. Zhao, E. Dall'Anese, Y. C. Chen, and S. V. Dhople. "Optimizing DER participation in inertial and primary-frequency response". In: *IEEE Transactions on Power Systems* 33.5 (2018), pp. 5194–5205.

[26] U. Markovic, Z. Chu, P. Aristidou, and G. Hug. "LQR-based adaptive virtual synchronous machine for power systems with high inverter penetration". In: *IEEE Transactions on Sustainable Energy* 10.3 (2019), pp. 1501–1512.

[27] L. Guo, C. Zhao, and S. H. Low. "Graph laplacian spectrum and primary frequency regulation". In: *Proc. of IEEE Conference on Decision and Control*. 2018, pp. 158–165.

[28] F. Paganini and E. Mallada. "Global analysis of synchronization performance for power systems: Bridging the theory-practice gap". In: *IEEE Transactions on Automatic Control* 65.7 (2020), pp. 3007–3022.

[29] L. Pagnier and P. Jacquod. "Optimal placement of inertia and primary control: A matrix perturbation theory approach". In: *IEEE Access* 7 (2019), pp. 145889–145900.

[30] W. Liu, G. Geng, Q. Jiang, H. Fan, and J. Yu. "Model-free fast frequency control support with energy storage system". In: *IEEE Transactions on Power Systems* 35.4 (2020), pp. 3078–3086.

[31] E. Mallada. "iDroop: A dynamic droop controller to decouple power grid's steady-state and dynamic performance". In: *Proc. of IEEE Conference on Decision and Control*. 2016, pp. 4957–4964.

[32] Y. Jiang, R. Pates, and E. Mallada. "Performance tradeoffs of dynamically controlled grid-connected inverters in low inertia power systems". In: *Proc. of IEEE Conference on Decision and Control*. 2017, pp. 5098–5105.

[33] Y. Jiang, R. Pates, and E. Mallada. "Dynamic droop control in low-inertia power systems". In: *IEEE Transactions on Automatic Control* (in press).

[34] Y. Jiang, E. Cohn, P. Vorobev, and E. Mallada. "Storage-based frequency shaping control". In: *IEEE Transactions on Power Systems* (in press).

[35] Y. Jiang, A. Bernstein, P. Vorobev, and E. Mallada. "Grid-forming frequency shaping control for low-inertia power systems". In: *IEEE Control Systems Letters* 5.6 (2021), pp. 1988–1993.

[36] J. O'Sullivan, M. Power, M. Flynn, and M. O'Malley. "Modelling of frequency control in an island system". In: *Proc. of Power Engineering Society 1999 Winter Meeting*. 1999, pp. 574–579.

[37] G. Lalor, J. Ritchie, D. Flynn, and M. J. O'Malley. "The impact of combined-cycle gas turbine short-term dynamics on frequency control". In: *IEEE Transactions on Power Systems* 20.3 (2005), pp. 1456–1464.

[38] A. Ulbig, T. S Borsche, and G. Andersson. "Impact of low rotational inertia on power system stability and operation". In: *IFAC Proceedings Volumes* 47.3 (2014), pp. 7290–7297.

[39] P. Kundur. *Power System Stability and Control*. 1st ed. McGraw-Hill, 1994.

[40] J. D. Glover, T. J. Overbye, and M. S. Sarma. *Power System Analysis and Design*. 6th ed. Cengage Learning, 2017.

[41] P. Vorobev, D. M. Greenwood, J. H. Bell, J. W. Bialek, P. C. Taylor, and K. Turitsyn. "Deadbands, droop, and inertia impact on power system frequency distribution". In: *IEEE Transactions on Power Systems* 34.4 (2019), pp. 3098–3108.

[42] G. Kou, P. Markham, S. Hadley, T. King, and Y. Liu. "Impact of governor deadband on frequency response of the U.S. Eastern Interconnection". In: *IEEE Transactions on Smart Grid* 7.3 (2016), pp. 1368–1377.

[43] H. Min, F. Paganini, and E. Mallada. "Accurate reduced-order models for heterogeneous coherent generators". In: *IEEE Control Systems Letters* 5.5 (2021), pp. 1741–1746.

[44] *System Operability Framework 2016*. Tech. rep. National Grid Electricity System Operator, 2016.

[45] *National Electricity Transmission System Security and Quality of Supply Standard*. Tech. rep. National Grid Electricity System Operator, 2019.

[46] V. Knap, S. K. Chaudhary, D. Stroe, M. Swierczynski, B. Craciun, and R. Teodorescu. "Sizing of an energy storage system for grid inertial response and primary frequency reserve". In: *IEEE Transactions on Power Systems* 31.5 (2016), pp. 3447–3456.

[47] A. R. Bergen and V. Vittal. *Power Systems Analysis*. 2nd ed. Pearson, 2000.

[48] K. Purchala, L. Meeus, D. Van Dommelen, and R. Belmans. "Usefulness of DC power flow for active power flow analysis". In: *Proc. of IEEE Power Engineering Society General Meeting*. 2005, pp. 454–459.

[49] F. Bullo. *Lectures on Network Systems*. 1st ed. Kindle Direct Publishing, 2020.

[50] R. A. Horn and C. R. Johnson. *Matrix Analysis*. 2nd ed. Cambridge University Press, 2012.

[51] S. Skogestad and I. Postlethwaite. *Multivariable Feedback Control: Analysis and Design*. 2nd ed. Wiley, 2005.

[52] E. Tegling, B. Bamieh, and D. F. Gayme. "The price of synchrony: Evaluating the resistive losses in synchronizing power networks". In: *IEEE Transactions on Control of Network Systems* 2.3 (2015), pp. 254–266.

[53] *Continental Europe Operation Handbook: P1—Policy 1: Load-Frequency Control and Performance [C]*. Tech. rep. Union for the Coordination of Transmission of Electricity, 2009.

[54] *Fast Frequency Response Concepts and Bulk Power System Reliability Needs*. Tech. rep. North American Electric Reliability Corporation, 2020.

[55] F. Paganini and E. Mallada. "Global performance metrics for synchronization of heterogeneously rated power systems: The role of machine models and inertia". In: *Proc. of Annual Allerton Conference on Communication, Control, and Computing*. 2017, pp. 324–331.

[56] G. Kou, S. W. Hadley, P. Markham, and Y. Liu. *Developing Generic Dynamic Models for the 2030 Eastern Interconnection Grid*. Tech. rep. Oak Ridge National Laboratory, 2013.

[57] T. C. Weigandt, B. Kim, and P. R. Gray. "Analysis of timing jitter in CMOS ring oscillators". In: *Proc. of IEEE International Symposium on Circuits and Systems*. 1994, pp. 27–30.

[58] *Rate of Change of Frequency (ROCOF) Withstand Capability*. Tech. rep. European Network of Transmission System Operators for Electricity, 2018.

[59] M. Driels. *Linear Control Systems Engineering*. 1st ed. McGraw-Hill, 1996.

[60] J. H. Chow and K. W. Cheung. "A toolbox for power system dynamics and control engineering education and research". In: *IEEE transactions on Power Systems* 7.4 (1992), pp. 1559–1564.

[61] B. K. Poolla, D. Groß, and F. Dörfler. "Placement and implementation of grid-forming and grid-following virtual inertia and fast frequency response". In: *IEEE Transactions on Power Systems* 34.4 (2019), pp. 3035–3046.

[62] J. Rocabert, A. Luna, F. Blaabjerg, and P. Rodríguez. "Control of power converters in AC microgrids". In: *IEEE Transactions on Power Electronics* 27.11 (2012), pp. 4734–4749.

[63] A. Ortega and F. Milano. "Generalized model of VSC-based energy storage systems for transient stability analysis". In: *IEEE transactions on Power Systems* 31.5 (2016), pp. 3369–3380.

[64] A. Yazdani and R. Iravani. *Voltage-Sourced Converters in Power Systems: Modeling, Control, and Applications*. 1st ed. Wiley, 2010.

[65] S. Golestan, J. M. Guerrero, and J. C. Vasquez. "Three-phase PLLs: A review of recent advances". In: *IEEE Transactions on Power Electronics* 32.3 (2017), pp. 1894–1907.

[66] S. Golestan and J. M. Guerrero. "Conventional synchronous reference frame phase-locked loop is an adaptive complex filter". In: *IEEE Transactions on Industrial Electronics* 62.3 (2015), pp. 1679–1682.

[67] H. Chávez, R. Baldick, and S. Sharma. "Governor rate-constrained OPF for primary frequency control adequacy". In: *IEEE Transactions on Power Systems* 29.3 (2014), pp. 1473–1480.

[68] G. E. Dullerud and F. Paganini. *A Course in Robust Control Theory*. 1st ed. Springer, 2000.